Growth by HVPE and characterizations of III-As nanowires

Gabin Grégoire

UNIVERSITE CLERMONT AUVERGNE

ECOLE DOCTORALE DES SCIENCES FONDAMENTALES

THESIS

By

Gabin GREGOIRE

To obtain the grade of

Doctorate of University

Specialty: Dense Environments and Materials

Growth by HVPE and characterizations of III-As nanowires.

Public oral defense on October 15, 2021, with the following commission:

Maria Tchernycheva	Research Director, C2N, France	Reporting judge
Charles Cornet	Professor, Institut Foton, France	Reporting judge
Ray LaPierre	Professor, McMaster University, Canada	Examiner
Vladimir G. Dubrovskii	Professor, St. Petersburg State University, Russia	Examiner
Catherine Bougerol	Research Director, Institut Néel, France	Examiner
Yamina André	Associate Professor, HDR, Institut Pascal, France	Thesis director
Evelyne Gil	Professor, Institut Pascal, France	Thesis director

Table of contents

Abstract **i**

Acknowledgements **ii**

Dedications **iv**

General introduction **1**

I HVPE of III-As nanowires **6**

I.1 The nanowire geometry: what for? 6

I.2 Main ways to synthesize nanowires 8

I.2.1 Vapor-Liquid-Solid (VLS) growth 8

I.2.2 Catalyst-free growth 9

I.2.3 Selective area growth 10

I.3 (In,Ga)As nanowires: state of the art 10

I.3.1 (In,Ga)As material properties 10

I.3.2 InAs and GaAs nanowire growth 12

I.3.3 InGaAs nanowire growth 15

I.3.4 (In,Ga)As nanowires applications 17

I.3.4.1 Infrared photodetectors application 17

I.3.4.2 Laser application 19

I.3.4.3 Photovoltaic application 20

I.4 Institut Pascal: experimental setup 22

I.5 Thermodynamic study of (In,Ga)As condensation in HVPE environment 23
I.5.1 Vapor phase composition 23
I.5.1.1 Formation of III-Cl precursors 23
I.5.1.2 AsH_3 decomposition 24
I.5.1.3 Partial pressures in the growth zone 25
I.5.2 Thermodynamics of InGaAs reaction 27
I.5.3 Comparison with MOVPE and MBE 31
I.6 Kinetics aspect of HVPE process 33

II InAs and GaAs nanowires grown by HVPE 40
II.1 Introduction 40
II.2 Self-induced growth of InAs nanowires on Si(111) substrate 41
II.2.1 Experimental conditions 41
II.2.2 Effect of the growth parameters on nanowires morphology 41
II.2.2.1 Effect of additional HCl 42
II.2.2.2 Effect of the growth temperature 43
II.2.2.3 Effect of the III/V ratio 46
II.2.3 Structural characterizations 47
II.2.4 Kinetic modeling 48
II.3 Selective area growth of InAs nanowires 51
II.3.1 Growth on GaAs(111)B substrate 52
II.3.2 Growth on patterned Si(111) substrate 54
II.3.3 Control of surface treatment step prior to growth 58
II.3.4 Investigation of the optical properties 59
II.4 Selective area growth of GaAs NWs 62
II.4.1 Growth of GaAs NWs dense arrays on GaAs substrates 63
II.4.2 GaAs growth on silicon substrates 66
II.4.3 TASE-HVPE of GaAs on GaAs and Si substrates 74
II.5 Conclusion 77

III Growth of $In_xGa_{(1-x)}As$ nanowires 80

III.1 Introduction 80
III.2 InGaAs NWs growth: effect of the growth parameters 81
III.3 Thermodynamics and kinetics of InGaAs growth 89
III.3.1 Adsorption flux J_{+4} 90
III.3.2 Desorption flux J_{-4} 91
III.4 Conclusion 95

General conclusion **98**

Bibliography **102**
Bibliography 102

Résumé

Dans ce travail, nous avons pour la première fois démontré la croissance sans catalyseur de nanofils III-As par épitaxie en phase vapeur par la méthode aux hydrures (HVPE). Dans un premier temps, nous avons réalisé la croissance auto-organisée de nanofils InAs sur substrats silicium ainsi que l'étude de l'effet des paramètres expérimentaux sur la croissance. Un modèle théorique a été développé démontrant que la croissance a lieu par condensation directe des espèces InCl et As_4 sur la surface des substrats. Par la suite, nous avons étudié la croissance sélective d'InAs et de GaAs sur substrats GaAs et Si. Il est démontré que la HVPE permet de facilement contrôler la morphologie du matériau en modifiant les conditions de croissance aux échelles submicrométriques et nanométriques. Les mesures FTIR réalisées sur des réseaux de nanofils démontrent le potentiel des nanofils InAs pour la réalisation de détecteurs multi-spectraux dans le domaine de l'infrarouge. Des caractérisations par photoluminescence sont réalisées afin d'étudier les propriétés optoélectroniques des nanostructures GaAs et InAs. Finalement, nous avons démontré la croissance sélective (SAG) de nanofils InGaAs sur substrat GaAs et Si. Une étude préliminaire de l'effet des paramètres expérimentaux sur la composition et la morphologie des nanostructures est présentée. Nous avons montré que la composition de l'alliage ternaire (InGaAs) peut être contrôlée en variant les pressions partielles d'InCl et GaCl. Un modèle théorique permettant de relier la composition de la phase vapeur à la composition du solide est introduit.

Mots clés : nanofils III-As, croissance auto-organisée, croissance sélective, épitaxie, HVPE.

Abstract

In this work, we have performed for the first time the catalyst-free growth of III-As by hydride vapor phase epitaxy (HVPE). We first studied the self-assembled growth of InAs nanowires on Si(111) and the effect of the growth conditions on InAs nanowire growth. A kinetic model has been developed demonstrating that growth occurs through a direct condensation of gaseous InCl and As_4 species on the substrate. Then, we studied the selective growth of InAs and GaAs on GaAs and Si substrates. The capability of the HVPE process to easily control the morphology of the nanostructures by simply modifying the growth parameters is highlighted. FTIR measurements performed on nanowires arrays have demonstrated the potential of InAs nanowires arrays for multi-spectral phototedetection in the infrared range. Photoluminescence characterizations are performed to study the optoelectronic properties of GaAs and InAs nanostructures. We demonstrated the selective growth (SAG) of InGaAs nanowires on GaAs and Si substrates. A preliminary study of the experimental parameters effect on the composition and morphology of the nanostructures has been conducted. We have shown that the ternary alloy composition can be controlled by varying the partial pressures of InCl and GaCl. Finally, a theoretical model, which links the vapor phase composition to the solid composition, is introduced.

Key words : III-As nanowires, self-assembled growth, selective growth, epitaxy, HVPE.

Acknowledgements

First of all, I would like to thank my thesis supervisors Yamina André and Evelyne Gil for the trust they have given me during these three years of PhD. Your encouragement and advice during these three years have greatly helped me and given me confidence. Yamina, many thanks for your warm welcome in Hamilton, I spent very good moments with your family. Reminder for Evelyne, in this period of COVID, do not touch your friend's "chouquette".

A big thank you to Mohammed Zegouhane (Docteur le Bœuf) who was my unofficial supervisor and who helped me a lot in this work. I have no doubt about your professional and personal success. Thanks to Hadi Hijazi for our exchanges on modeling. Finally, thanks to both of you and Jihen for the good times spent in conference and during coffee breaks.

Thanks to Dominique Castelluci, our team engineer, for his availability and his skills which allowed me to realize this thesis in good conditions. Thanks also to Geoffrey Avit for having taken over during my third year, the team is in good hands with you.

I thank Catherine Bougerol from Institut Néel for the structural characterizations of nanowires by TEM, EDS, FIB and DRX. Thanks to Eric Tournié and Thierry Taliercio for the interresting collaboration.

Many thanks to Professor Ray LaPierre, for his welcome in his laboratory at McMaster University and his numerous scientific advices. I also thank Nebile Isik Goktas for the numerous experiments she performed for me.

I would like to thank Professor Vladimir Dubrovskii from ITMO St-Petersburg for the collaboration which allowed me to better understand the growth of nanowires.

Many thanks to Heinz Schmid, Kirsten E. Moselund, and Philipp Staudinger, from IBM Europe, for the collaboration which allow me to have nice results.

Thanks to Anne-Marie and Arnaud for these three years of SEM and also for the friendly discussions. A big thank you to the OSS team for the first PL measurements and their advice on photoluminescence. Special mention to Pierre Disseix, Martine Mihailovic and François Meydard for the numerous discussions during lunch time and coffee breaks. I also think of Françoise Bohaud for her precious help and the moments of laughter that we spent together.

I also think of my friends Léo, Léa, Charly and Loic with whom I spent memorable moments. You have seen me at my best during these three years. Léo, Charly and Loic, it is soon your turn!

These thanks would not be complete if I did not thank all my family who supported me during these three years but also during the 23 previous years.

Finally, all my gratitude goes to my love, Chlöé, for is unconditional support during these 3 years.

Dedications

To my grandfather Joseph

General introduction

Scientific community has been working on III-V semiconductor nanowires (NWs) and their potential for electronic and photonic device applications for more than 20 years. Indeed, variety of nanowire-based devices have been developed, including photo-detectors, solar cells, lasers and transistors.

Molecular beam epitaxy (MBE) and metal organic vapor phase epitaxy (MOVPE) are the most widely used growth techniques to synthesize NWs. During my PhD, I implemented HVPE: hydride vapor phase epitaxy. This process has been developed at Institut Pascal since the 1970s for the growth of III-V planar layers. In the last decade, Institut Pascal has demonstrated the successful growth of gold-catalysed GaAs NWs on GaAs [1] and Si substrates [2], and self-catalysed GaAs NWs on Si [3] as well. The group also demonstrated HVPE-growth of InGaN nanowires with perfect control of the alloy composition, In and Ga amounts [4].

HVPE takes advantage on high material input and high surface kinetics to grow gold-catalysed GaAs NWs of exceptional length with extremely high growth rate up to 170 µm/h, with a pure crystalline quality. The growth of such NWs has been first achieved on GaAs substrates and then developed on Si. Yet, gold is known to incorporate in the NWs and is not compatible with the silicon electronic platform. Furthermore, VLS (vapour liquid solid)-VPE growth of GaAs NWs is difficult to apply on silicon substrate. It was indeed demonstrated that Si atoms, coming from the substrate, enter the catalyst droplets and disturb the nucleation of NWs [2]. It results in the growth of large scales and parasitic crystals for gold-catalysed NWs, and extremely low density for self-catalysed NWs. Consequently, efforts should be pursued to develop catalyst-free growth of III-As NWs, which is the main topic of my PhD.

Part of my thesis work was performed within project ENNORA (2017-2022) (Epitaxie de Nanofils semiconducteurs pour l'ENergie. PrOpriétés StRucturales, Optiques et de TrAnsport Electrique) funded by the region AURA (Pack Ambition Recherche). The project objective, which brings together four French laboratories (Institut Pascal, CEA-INAC, Institut Néel and INSA-INL), is the growth and characterization of III-As and III-Nitride NWs for energy conversion applications. Within the project, Institut Pascal is in charge of the HVPE growth of InGaAs NWs. Another part of my thesis work was developed within project ENUF (Evaluation of Novel Ultra-Fast selective III-V Epitaxy) ERC Grant

(2019-2020) coordinated by IBM Europe. ENUF aims at promoting growth of high quality III-As material on silicon using template assisted selective epitaxy (TASE) and HVPE. Finally, I have been involved in a collaboration with Professor Ray LaPierre from McMaster University (Canada) where I stayed for 1 month. The objective was to develop growth of nanodevices based on III-As nanowire arrays. Thesis results are presented in this manuscript which contains three chapters.

The first chapter introduces the main characteristics of III-V nanowires. One-dimensional structures are discussed with respect to two-dimensional layers. The different growth modes of III-As NWs, self-organized growth mode, catalyzed (VLS) growth mode and selective area growth (SAG), are exposed. A state-of-the art of InGaAs NWs growth is presented. It highlights the main issues with the growth of InGaAs NWs for the different growth techniques. Variety of InGaAs NWs applications are given showing the potential of InGaAs NWs for optoelectronic devices. The HVPE facility which I used during my thesis is then described, followed by the calculation of the vapor phase composition as a function of the initial gas fluxes. Finally, the basic thermodynamic and kinetic principles necessary to understand the growth mechanisms involving gaseous chloride precursors are introduced.

Chapter II is devoted to the catalyst-free growth of GaAs and InAs nano and micro-structures on GaAs and Si substrates. We report the first HVPE growth of self-induced InAs NWs on bare Si(111) substrate with high growth rate up to 50 µm/h. An experimental study as a function of the vapor phase composition and growth temperature is conducted to understand the underlying nucleation and growth mechanisms of NWs. Then we present a theoretical model of condensation that explains the growth mechanisms. In the second section, we describe HVPE selective area growth (SAG) of InAs NWs on patterned substrates. We have demonstrated the growth of well ordered InAs NWs arrays on both GaAs and InAs substrates, as part of the collaboration with Pr. Ray LaPierre, with the aim to develop multi-spectral photo-detectors requiring a high flexibility in terms of NWs length and diameter. The effect of the growth conditions and pattern design on the crystal morphology is investigated. The optical properties of InAs NWs arrays are explored by photo-luminescence (PL) and FTIR measurements. In the third section, we report the selective growth of GaAs material on GaAs and Si substrates in the framework of the ERC ENUF project. The aim of ENUF is to develop and optimize the growth of III-As material on silicon using template assisted selective epitaxy (TASE) and HVPE. We have reached a high selectivity of GaAs growth over large patterned surfaces on GaAs substrate. Direct growth on Si substrate of GaAs NWs and platelets and their crystal quality is then studied. At the end of ENUF project, the growth of GaAs material on Si(111) using TASE-HVPE was successfully achieved.

In Chapter III, we report preliminary results on the growth of InGaAs material. Selective growth of In-rich InGaAs NWs on GaAs and Si substrates is achieved and the variation of the Ga concentration as a function of the vapor phase composition is investigated. The influence of the growth parameters on the crystal morphology is briefly discussed. A theoretical model which links the alloy composition to the vapor composition and growth temperature is developed. This model is based on kinetic principles of HVPE and follows a semi-empirical approach.

Chapter I

HVPE of III-As nanowires

I.1 The nanowire geometry: what for?

Since their discovery in the 60's by Wagner and Ellis, the interest in nanowires has grown increasingly. Nanowires are 1D objects with very peculiar properties in terms of strain relaxation, electrical transport, and light interaction. Controlling these properties is a key point for the development of efficient electronic and optoelectronic devices.

Main advantages of the 1D geometry:

The main issue with the epitaxial growth of semiconductors material on heterosubstrate is the difficulty to grow defect-free crystal. Growth of 2D layers on highly mismatched substrates can generate strains at the interface between the grown material and the substrate. It results in a poor quality interface with a high density of misfit dislocations which strongly reduce the optical and electrical properties of the grown material. In fact, structural defects in III-V semiconductors are known to act as non-radiative recombination centers. The NW geometry, with its small lateral size allows an efficient elastic stress relaxation through the free lateral surfaces (figure I.1) [5, 6, 7]. It enables the growth of dislocation-free III-V materials even in high lattice-mismatched systems [5, 6].

Many studies have been conducted on the strain relaxation in nitride NWs. Same considerations can be applied to III-As nanowires. Growth of dislocation-free III-As/P nanowire heterostructures has already been demonstrated. F. Glas et al. [8] showed that for a given misfit percentage, there is a critical diameter below which NWs are dislocation-free. In this study, the critical nanowire length above which dislocations become energetically favorable, is calculated as a function of the NW initial radii and for different lattice mismatch values [8]. The results are presented in figure I.2-(a). We can see that for a lattice mismatch of 2% the nanowire are dislocation free if the initial radius is below 100 nm, while for a radius of 200 nm dislocation will appear for NW length above 6 nm.

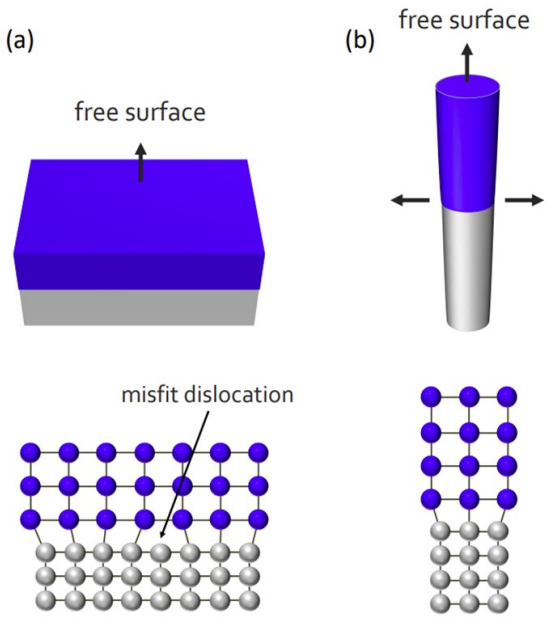

Figure I.1: Schematic of a) planar growth and b) nanowire growth on heterosubstrate. Strain relaxation results in misfit dislocation for the 2D layer, while strain is relaxed through the free-lateral facets of the NW. From [7].

Nanowires offer a suitable solution to design active III-V devices on mismatched substrates. This 1D geometry also makes it possible to consider core/shell heterostructures [9, 10]. In this type of structure, the inner material is called the core and the surrounding material is the shell. From a geometrical point of view, radial heterostructures of high aspect ratio provide a larger active area for the same amount of substrate surface. This permits to use the large interface of the core/shell active surface, and increases the emission efficiency per unit area of the substrate surface. The radial growth can also be used to passivate the core [11], or to generate a p-i-n junction for photovoltaic applications [12]. However it is still a complex task to achieve dislocation free radial growth due to the large surface of a NW. Theoretical calculation realized by S. Raychaudhuri [6] predicts the critical radius for different material systems. An example is shown on figure I.2-(b) for InAs core / $In_{1-x}Ga_xAs$ shell NWs for different shell thicknesses and indium compositions. Below each line, the growth is dislocation free. For example, for NWs with a radius of 60 nm and an indium composition of 0.1, a 20 nm shell can be grown without dislocation. Thus, to avoid the formation of dislocation, the diameter of the NWs should be sufficiently small.

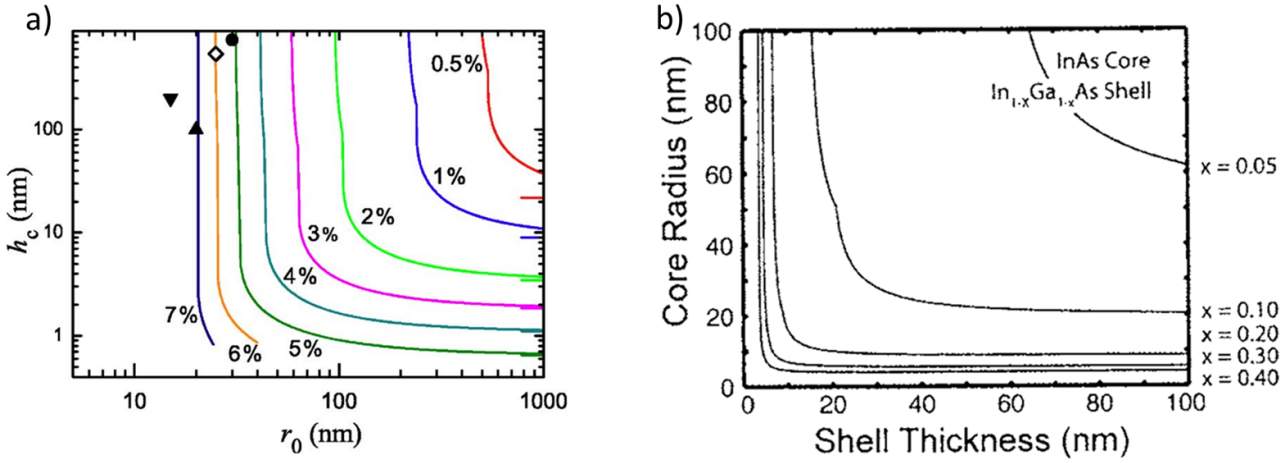

Figure I.2: (a) Change in critical thickness before the formation of dislocations depending on the radius of the NW for different lattice mismatch values. From [8]. (b) Determination of the maximum thickness of an InGaAs shell without dislocation around an InAs core for different indium compositions. Adapted from [6].

I.2 Main ways to synthesize nanowires

Molecular Beam Epitaxy (MBE), Metal Organic Vapor Phase Epitaxy (MOVPE) and more recently Hydride Vapor Phase Epitaxy (HVPE), are the most popular techniques to synthesize nanowires. For all this techniques, different approaches can be considered to grow NWs such as catalysed-growth, catalyst-free growth and selective area growth (SAG).

I.2.1 Vapor-Liquid-Solid (VLS) growth

The VLS growth of nanowire was first investigated in 1964 by Wagner and Ellis [13] with the growth of silicon NWs. The growth was achieved on silicon substrate by the means of gold particles using H_2 and $SiCl_4$ precursors. The gold droplets are obtained by depositing a thin solid Au layer which is annealed before the growth. A representation of the growth mechanism is shown on figure I.3. Under high temperature, gold droplets are formed on the substrate. The droplets act as catalyst by increasing the pyrolysis reaction $SiCl_4+2H_2 \rightleftharpoons Si+4HCl$ and the collect of the $SiCl_4$ precursor. Moreover, the droplets lower the nucleation barrier at the liquid/solid interface enabling solidification of Si material when supersaturation over equilibrium is reached. Solidification occurs through the nucleation and lateral extension of a 2D island. The initial size of the droplet defines the NW diameter. It can be tuned by changing the Au layer thickness and the annealing conditions as well.

Later, the same process was applied to GaAs nanowires growth paving the way to the integration of high quality III-As material on various substrates. Then, efforts were made to understand the

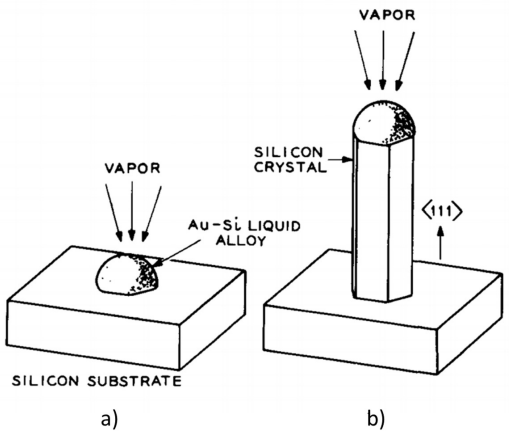

Figure I.3: Illustration showing the growth of a silicon whisker by VLS: a) Au-Si droplet on the Si substrate at the initial stages of growth; b) growth of pure Si crystal under the droplet. From [13]

NW morphology variation depending on the growth parameters. Taking the example of MBE grown GaAs NWs, it was shown that together with the droplets size distribution, the variations of the growth temperature and precursor fluxes influence the NWs radius, length, density and shape [14]. Today, gold-catalysed growth is the most documented and the most used approach. With regard to purity, even if the phase diagrams do not show solid alloys of Au with Si or III-V semiconductors, Au can still incorporate in the NW by diffusing on the sidewalls. Yet, gold particles are known to act as an impurity by introducing deep level recombination centers, which significantly degrade the electrical and optical properties of the system [15, 16].

In 2008, Colombo et al. [17] and Jabeen et al. [18] demonstrated the growth of GaAs NWs using Ga as the droplet catalyst. Their works introduced the concept of self-catalysed III-V NWs growth, for whom growth is promoted by the group III metal (Ga for GaAs and In for InAs). This approach circumvents the incorporation of impurities and enables the growth of high purity NWs compatible with the Si-CMOS technology. The group III element can be deposited before growth, or it can be formed directly on the substrate during the NW growth. The key parameters governing the III-assisted growth of III-As nanowires by MBE are: the oxide layer which provides the sites for nucleation, and offers the wetting characteristics which favor the formation of droplets [19, 20]; the arsenic flux controlled by the As_4 pressure [14], which limits the axial growth rate; the III adatoms flux at the droplets which increases the growth rate [21].

I.2.2 Catalyst-free growth

The growth occurs without the use of any seed particles, and the precursors condensate directly on the substrate or incorporate after diffusion along the lateral facets. The use of specific growth conditions is required to enable an anisotropic growth with a very high axial growth rate. Such growth anisotropies are governed by the specific surface energies of the respective facets, which are

very sensitive to the chemical potential μ, and therefore are strongly governed by growth conditions. These facet-dependent growth anisotropies describe the underlying mechanism of catalyst-free VS-type growth of NWs, independent of whether they are grown either directly on a foreign substrate such as Si (heteroepitaxy) or on any given substrate (including homoepitaxy) as in the case of selective area growth (SAG) as discussed below. Epitaxial NWs only nucleate on oxide free surface, however, on completely oxide-free substrate, large islands nucleate due to the high mobility of the III adatoms [22]. Such islands have a drastically reduced axial growth rate, hindering the nanowire growth. The NWs morphology and density are tuned by a precise control of pin-holes formation in the oxide layer. This is achieved by the pre-deposition of an oxide layer followed by an etching of this latter [23, 22, 24]. However, even if the density of NWs can be controlled, the NWs are still randomly distributed on the substrate.

I.2.3 Selective area growth

Selective area growth (SAG) consists of the growth of NWs on pre-defined location. This technique requires the pre-deposition of a dielectric mask (SiOx, SiNx) on the substrate. Then holes with well defined pitch and diameter are open using lithography technique. Today, openings with few tens nanometers can be achieved by Electron Beam Lithography (EBL). This method enables the control of the NWs size and density which are key parameters for applications where light absorption depends on the pitch and NWs morphology. Concerning the growth, it can proceed either by the VS or VLS mode. In both cases, it is assumed that the step-edge of the opening favors the nucleation of the crystal or the formation of the III-droplet (Ga / In). A thin layer of In or Ga can also be pre-deposited on the substrate. During annealing, the metal atoms diffuse into the openings to form the catalyst droplet. In MBE and MOVPE, the control of the morphology is achieved by tuning different growth parameters [25, 26] (temperature, growth time and III/V ratio) and by tuning the pattern design and dimension [27, 28, 29]. Selectivity is more restricted in MBE compared to MOVPE due to a lower desorption of group-III atoms from the dielectric mask. Thus, MBE SAG growth is only achieved when sufficient atom diffusivity is reached [29].

I.3 (In,Ga)As nanowires: state of the art

I.3.1 (In,Ga)As material properties

Arsenide based nanowires can crystallised into two phases, zinc blende (ZB) and wurzite (WZ) (figure I.4). The ZB phase is a face centered cubic (fcc) structure containing two sub-lattices at (0,0,0) and (1/4,1/4,1/4) a_{ZB}, filled with (In,Ga) and As atoms, respectively. A III-As material growing along the [111] direction can be terminated either with (In, Ga) atoms corresponding to III-As(111)A, or with As atoms for III-As(111)B. The ZB crystal is a repetition of three bilayers represented as "ABCABC" sequences (see figure 1.4-(c)). The wurtzite structure is formed by the penetration of two

hexagonal compact (hcp) lattices with "ABAB" stacking sequence, one lattice of III atoms (In,Ga) and one of As atoms. Both lattices have the same axes and are shifted by $3/8c_{wz}$ as illustrated in figure 1.4-(a) and (b). The atomic arrangement of the wurtzite structure along the a_{wz} axis ([0001] direction) is identical to ZB structure along the [111] direction. A representation of GaAs ZB and WZ structures is shown figure I.4. The yellow atom can be either In and/or Ga atom.

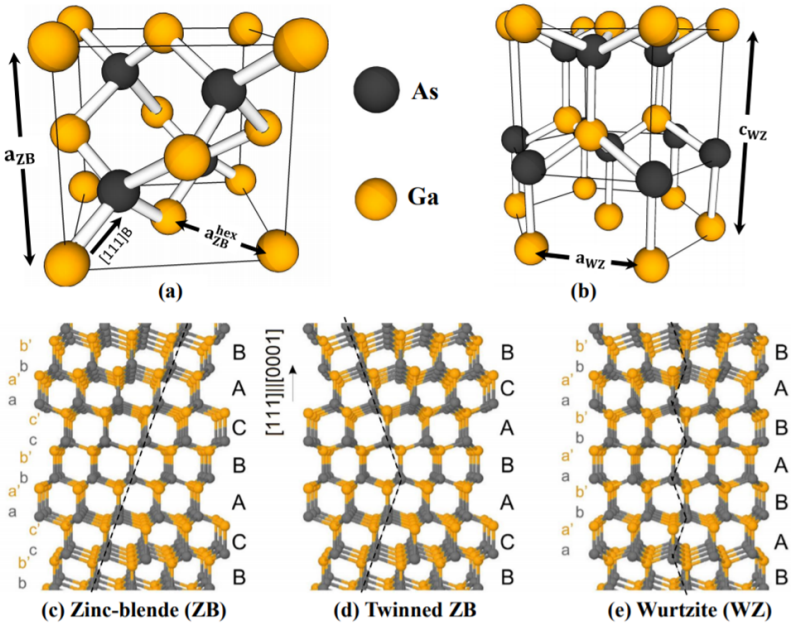

Figure I.4: a) GaAs zinc-blende (ZB) lattice and b) Wurtzite (WZ) lattice of GaAs crystal. c) ZB, d) Twinned ZB and e) WZ crystal structure along the $< 111 >$ direction. Viewing direction is $< 1120 >$. From [30].

III-As materials mainly crystallize in the Zinc-Blende structure in planar or massive layers. In NWs, both phases can be obtained. The surface to volume ratio in these structures is very high compared to bulk materials, thus the surface energy plays a more important role. In one hand, the WZ phase has a lower number of dangling bonds on the NW side facets, which manifests as a lower surface energy for this phase. On the other hand, the ZB phase possesses a cohesive energy, between an atomic pair, about 24 meV lower than in WZ [31]. Given that, it can be easily imagined that the growth of NWs is a competition between the two phases.

Because the ZB phase is the principal phase observed in this work, we will focus on the properties of this one. Cubic (In,Ga)-As based semiconductors are direct band-gap semiconductors. The minimum of the conduction band and maximum of the valence band are located at the center of the Brillouin zone at k = 0 (see figure I.5-(a)). The valence band structure near the Γ-symmetry point consists of a heavy hole band, a light hole band, and a split-off band. The heavy hole and light hole bands are degenerate at the Γ-point. Measuring energy from the top of the valence band at the Γ-point, the split-off energy in GaAs is E_{so} = -0.34 eV and E_{so} = -0.41 eV in InAs. Due to the direct gap, the probabilities of generation and radiative recombination of carriers are very important. Thus III-V

semiconductors are very efficient at converting electronic energy into light energy and reciprocally. This constitutes a big advantage compared to silicon whose indirect gap limits optical absorption. The band-gap energies (Eg) vary from 0.36 eV for InAs to 1.425 for GaAs at 300K. The interest in InGaAs alloy arises mainly from its band gap and wavelength tuning covering wavelength between 880 and 3500 nm. The bandgap energy can be tuned by controlling the indium concentration. Band-gap energy (E_g) as a function of the indium concentration is given by the following equation:

$$E_g(x) = E_g(GaAs) - 1.501x + 0.436x^2$$

Where $E_g(GaAs)$ is the band gap energy of ZB GaAs and x is the In concentration.

E_g at 300K as a function of the In fraction is plotted on figure I.5-(b).

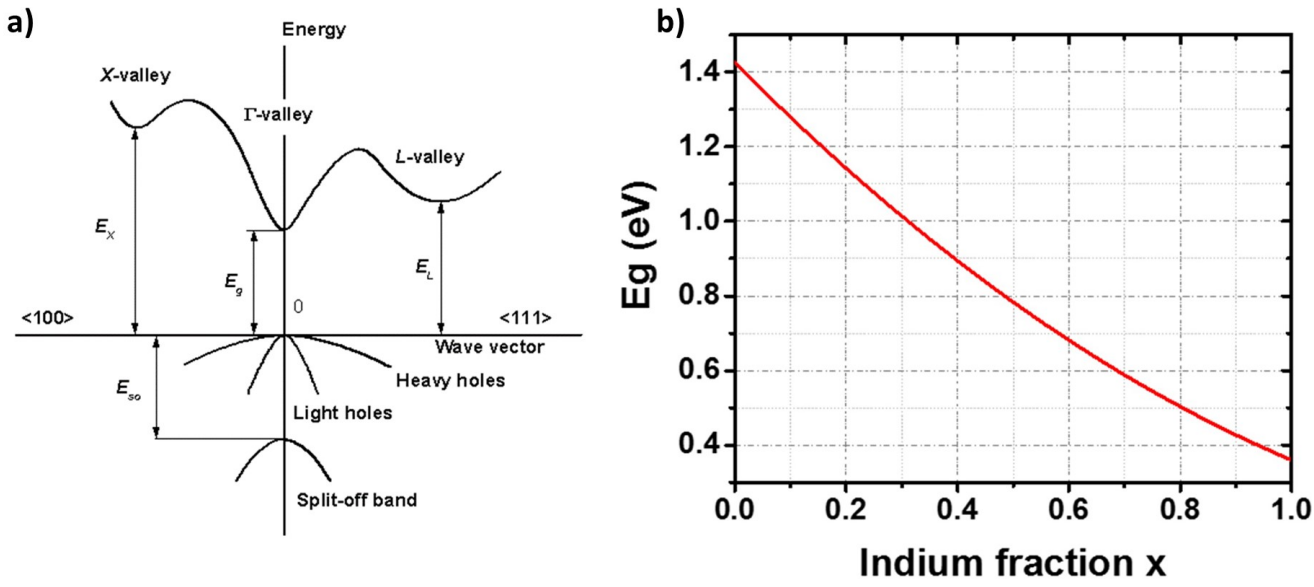

Figure I.5: a) Band structure of cubic III-arsenide material near k=0, b) InGaAs band-gap energy as a function of the indium concentration. The curve is given by the Vegard law.

I.3.2 InAs and GaAs nanowire growth

The growth of III-As NWs has been widely studied by MBE, MOVPE and HVPE. One of the most documented method to grow III-As NWs is the Au-catalyzed growth since it was the first method which succeeded to produce NWs. Now the relationship between the size of the Au droplet, selected growth parameters and the growth kinetics have been formulated for all these growth techniques [32, 33]. In MBE and MOVPE, it appears that the nanowires growth is very sensitive to the diffusion of the element III. In ref. [34], the dependence of GaAs NWs lengths on the size of gold catalyst particles has been studied. It was shown that the growth of NWs exhibiting diameters lower than 100 nm was mainly the diffusion-induced growth. In other terms, the diffusion of ad-atoms from the

substrate to the top of NWs considerably increases the length of NWs, especially for low diameters (<100 nm). Moreover, J.C Harmand et al. [35] have studied the effect of the Ga diffusion length on the NWs morphology. At low temperature, the diffusion length of Ga is small, enabling nucleation on the sidewalls before the adatoms reach the top of the wires. Thus the NWs have a conical shape (see fig I.6-(a). When the temperature is raised, the diffusion length is increased so that the adatoms can reach the gold particle and the NW become more cylindrical (figure I.6-(b)).

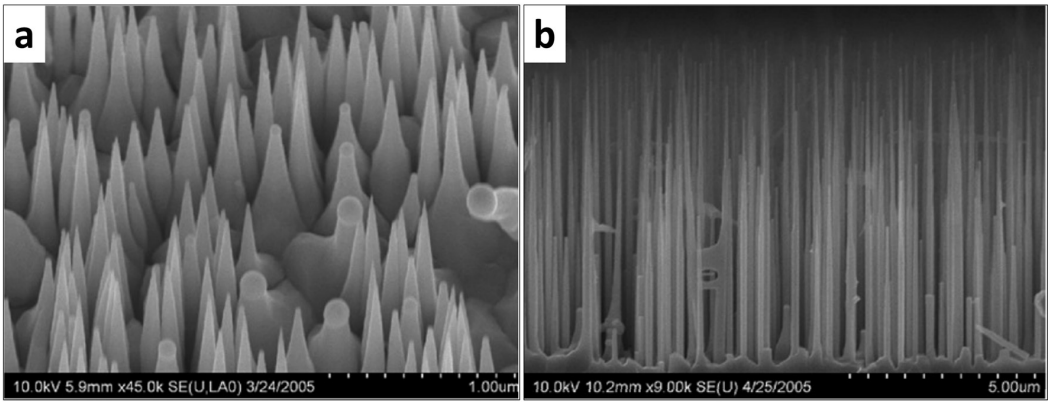

Figure I.6: SEM images of gold catalysed GaAs nanowires grown by MBE at a) 420 °C and b) 580 °C. Adapted from [35].

The same behavior can also be observed for gold-catalysed InAs NWs grown by MOVPE when diffusion of ad-atoms dominates the growth rate, and chemical reaction is negligible [36]. With the HVPE technique, gold-catalyzed GaAs NWs with exceptional lengths and pure ZB crystal structure can be obtained [1]. Growth rate up to 170 µm/h can be reached for a growth temperature of 715 °C and a III/V ratio of 5 which is way above MOVPE and MBE growth rates, which do not exceed some µm/h. The reasons standing behind that are the high material input (3×10^{-4} and 3×10^{-3} atm for $GaCl_g$ and As_{4g}, respectively) and the high dechlorination rate of the element III precursor (GaCl) in HVPE. Finally, gold-catalyzed growth is an easy way to achieve the growth of defect-free nanowires. In the case of Au-assisted InAs nanowires, only MBE have succeeded in growing pure wurtzite NWs [37, 38]. The good crystalline quality is attributed to the very small diameter (20 nm) of the NWs [37]. However, as already said, Au is known to acts as impurity which creates deep-level recombination centers, degrading the properties of the material. Consequently, effort has been devoted to grow gold-free III-As NWs by implementing self-catalyzed growth.

While self-catalysed growth of GaAs NWs was performed successfully by MBE, MOVPE [15] and HVPE [3] have shown limited progress, despite the serious attempts reported in the last few years. Indeed, Breuer et al [15]. have studied the self-catalyzed growth of GaAs NWs by MOVPE on Si(111) substrates and have shown that the nucleation can occur at 600 °C using low III/V ratio (<1). However the density and the randomness of the structures are still far from being controlled. The same observations were found by Dong et al. [3] using HVPE. For VPE processes, the main challenge is related to the temperature required for cracking chemical precursors (such as organometallic precursors), combined with arsenic rich atmosphere in the reactor. Such conditions do not favor both

the initial nucleation and the further stability of the liquid gallium droplets [39, 40]. Given these limitations, it is extremely difficult to find appropriate conditions for Ga-catalyzed VLS growth and GaAs nanowires obtained so far are limited in length (typically less than 1μm). On the other hand, self-catalysed InAs NWs growth has been successfully demonstrated for both MBE [21, 41, 42] and MOVPE [43, 44]. However, it is not straightforward to determine whether a droplet is present during the growth or not. In fact, indium droplets are rarely observed on the tip of the NWs at the end of the growth, especially in MOVPE system. An example of self-catalysed InAs NWs grown by MBE is shown on figure I.7.

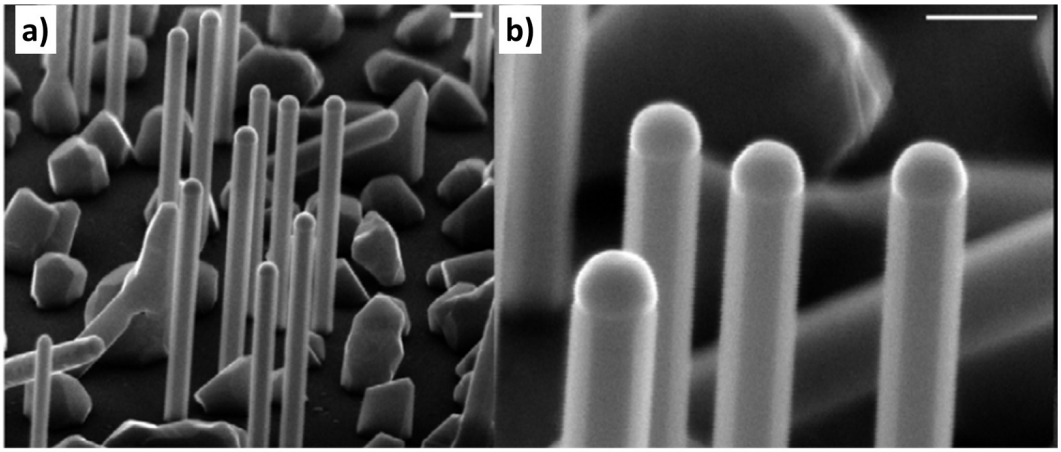

Figure I.7: SEM images showing self-catalysed InAs NWs grown by MBE. An In droplet is visible on the top of the NW. The contact angle is approximately 90°. The scale bars are 200 nm. Adapted from [21].

At the same time, many studies focused on the catalyst-free growth of III-As NWs. As for catalysed growth, the morphology of the NWs is controled by changing the growth parameters [45, 46]. For both self-catalyzed and catalyst-free NWs, many authors showed the importance of the surface preparation before growth. As mentionned earlier, the optimization of the oxide layer is necessary to observe the nucleation of NWs. Moreover, in ref. [9, 47], it is reported that the arsenic (As) pretreatment of the Si(111) surface to form the (111)B like surface, is mandatory to ensure the vertical growth of GaAs and InAs NWs.

An alternative technique based on selective area growth (SAG) was developed to produce periodic NW arrays on patterned substrates, where growth occurs on pre-determined sites. This approach allows the integration of NWs into large-scale arrays with homogenous properties [11, 48]. SAG of GaAs and InAs NWs on various substrates has been demonstrated by (MBE) and (MOVPE) [9, 25, 28, 49, 50, 51]. Several studies have shown a strong relationship between the pattern hole size and the final shape of the GaAs and InAs crystal grown on GaAs (111)B and Si(111) substrates [52, 53]. H. Yoshida et al. have reported that the morphology of the GaAs crystal evolved from an hexagonal NW to a truncated tetrahedra shape when the aperture diameter is higher than $\sim$ 100 nm [53]. These findings were also confirmed experimentally and supported by a theoretical model based on the Gibbs free energy variation by K. Ikejeri et al. [50]. Wang et al. [54] observed a different

behavior when increasing the holes size (figure I.8). They have demonstrated that by increasing the hole diameter, the number of NWs per hole increased. In smaller opening, once a nanowire nucleates, it acts like sink for adsorbed species and suppresses the formation of other nucleus. Above a certain diameter, the number of adsorbed species is high enough to enable multiple NWs nucleation.

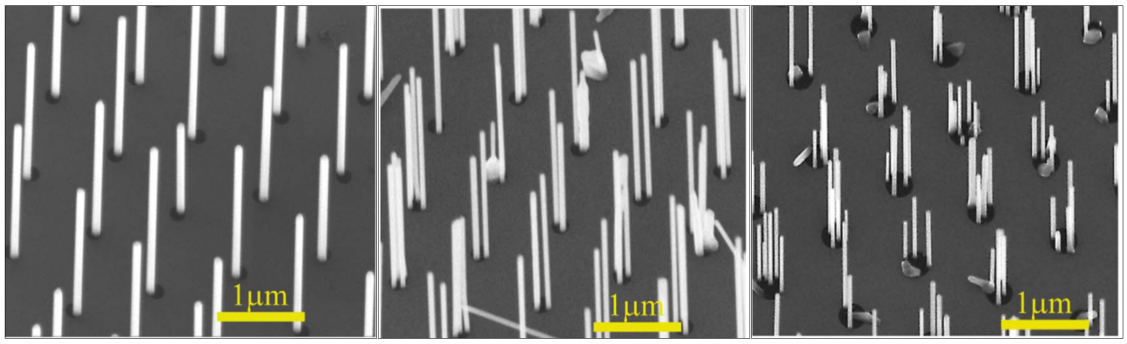

Figure I.8: SEM images of InAs NW arrays on Si(111) grown by MOVPE. The sizes of nanoholes are (a) 160 nm, (b) 200 nm, (c) 300 nm. Adapted from [54].

Selective area epitaxy can also be combined with self-catalysed growth [55]. M T. Robson et al. [56] developed a model to determine the growth conditions resulting in a high yield of self-catalysed SAG InAs NWs. They showed that precise group V and III fluxes are needed to nucleate a small droplet and then one NW per hole. They also showed that excessive group III flux lead to large droplets and irregular crystallites. Excessive group V fluxes resulted in a VS growth of crystallites. Moreover, in ref. [57], it is demonstrated that the diameter/height aspect ratio of openings impacts the yield of vertical NWs. Finally, no matter what the growth mechanism is (VS or VLS), the 1-D geometry during SAG depends not only on the growth conditions (temperature and vapor phase composition), but also on the pattern dimensions.

I.3.3 InGaAs nanowire growth

As we discussed previously, the growth of Au-catalyzed InAs and GaAs NWs is now well established. However, when it comes to Au-assisted InGaAs NWs, controlling the morphology and the composition is not straightforward, since In and Ga atoms exhibit different properties in terms of surface diffusion, kinetics of incorporation and solubility [58]. Concerning the morphology, strong NW tapering were observed by Regolin et al., using MOVPE growth [59] .In ref. [58, 60], the variation in density and shape is explained by the large differences in surface diffusion of the respective In and Ga adatoms on the surface. The In diffusion length is much longer than that of Ga atom. Then, the non-uniform geometry of the NWs is associated to a large In/Ga compositional variation along the NW, with a three times higher In concentration near the base as compared to the top region of the NWs.

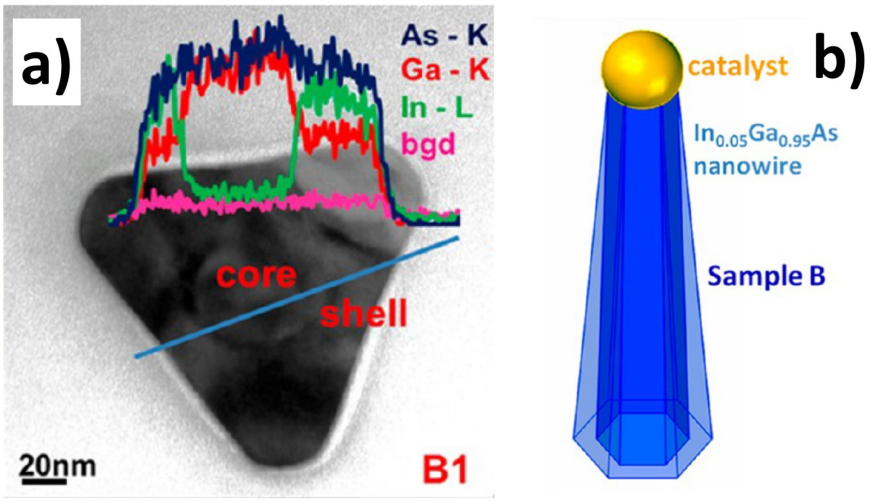

Figure I.9: Gold-catalysed InGaAs nanowires grown by MOVPE. a) TEM images of InGaAs nanowire cross sections. b) Schematic illustration of a 3D structural model of as-grown $In_{0.05}Ga_{0.95}As$ nanowires, showing a Ga-rich InGaAs core and an In-enriched InGaAs shell. Adapted from [61].

These findings were further supported by Guo et al [61] who showed that the grown InGaAs NWs had an unintentional core-shell structuration (figure I.9). The core is composed of Ga rich InGaAs and and the shell is In rich InGaAs. In atoms have a higher affinity with Au than Ga atoms, thus Ga atoms diffuse more easily to the growth front compared to In atoms. The core growth is mediated by the gold droplet while the shell growth occurs through the VS mode. More recently, it has been demonstrated that non-tapered InGaAs NWs can be grown by reducing the temperature and the V/III ratio. The NWs exhibit length of several microns and a higher compositional uniformity [62].

Au free InGaAs NWs growth is more desired with regards to gold contamination, as we mentioned earlier for GaAs and InAs NWs. Heiss et al. [63], reported the growth of self-catalysed InGaAs NWs by MBE where the growth occurs via a Ga rich droplet. However, they observed a delay for the In atoms to precipitate in the solid resulting in a limited indium incorporation ($x_{In} < 5\%$). Moreover, a core-shell structure with In rich shell was obtained when the growth temperature was decreased. This behavior is similar to gold-catalyzed InGaAs NWs (Figure I.9). Thus, due to the non uniformity of morphology and composition for NWs grown by VLS, efforts were made to develop catalyst-free growth of InGaAs NWs. Shin et al. [64] demonstrated the growth of non-tapered and high aspect ratio self-assembled InGaAs NWs, using MOVPE. The nanowires were grown on Si subtrate and their In concentration ranging from 0.2 to 1. Compared to VLS grown NWs, the overall composition was much more homogeneous. Nevertheless, despite the good composition homogeneity of a single InGaAs NW, large composition variations could be observed from one NW to an other. This observation was correlated with the random NWs nucleation on the substrate and thus the NWs density. In fact, due to the different diffusion lengths of Ga and In atoms, incorporation ratio of Ga and In atoms is very sensitive to the NWs inter-distance. The latter may vary along the substrate due to the random distribution of the nucleation sites. Kobmuller and Hertengberger [65], studied the variations of the NWs composition and morphology as a function of the growth parameters. In their work, they high-

light the benefits of using patterned substrate to optimize composition homogeneity. As can be seen on the XRD spectra (figure I.10), the peak full-width-at-half-maximum (FWHM) is smaller in the case of InGaAs NWs grown by SAG. It shows that the composition of the NWs across the substrate is much more homogeneous compared to self-assembled NWs.

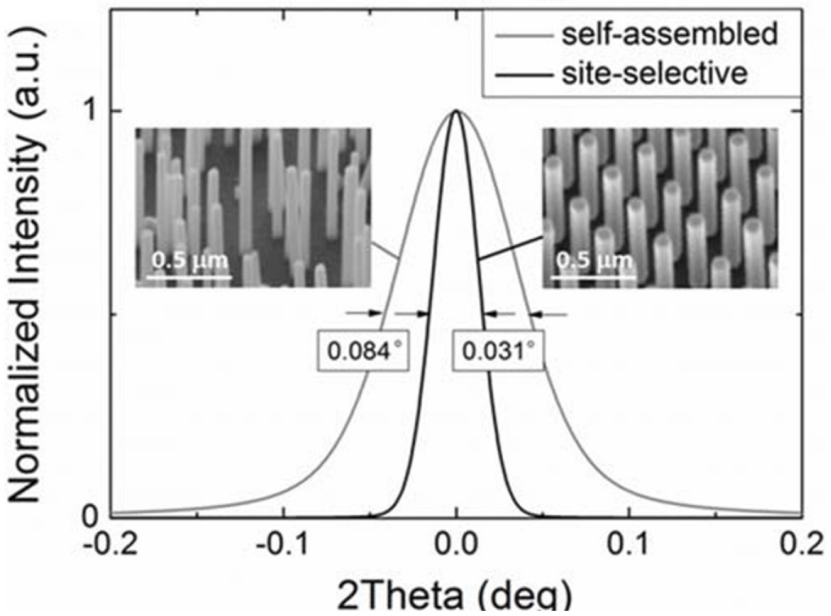

Figure I.10: Normalized intensity of the 2θ-InGaAs peak position (fixed at 2θ=0) comparing similarly grown site-selective $In_{1-x}Ga_xAs$ NWs [x(Ga)=0.07, black] and self-assembled $In_{1-x}Ga_xAs$ NWs [x(Ga)=0.08, grey]. Insets illustrate representative SEM images of the two different types of NWs. From [65].

I.3.4 (In,Ga)As nanowires applications

As introduced in section I.1, the NW geometry presents specific properties, offering a wide range of applications. In fact, the cost of devices can be drastically reduced by using lattice-mismatched but cheap substrates (Si) while keeping a high efficiency. InGaAs NWs are very promising for IR photodetection applications due to their high electron mobility, high adsorption coefficient, and their bandgap tunability in a wide range of wavelength in the near infrared range 870-3500 nm. In this part, we will focus mainly on light emitting devices, photo-detectors and photovoltaic applications which are the main domains targeted for the III-As NWs which are developed at Institut Pascal.

I.3.4.1 Infrared photodetectors application

One of the simplest forms of photodetectors are photoconductors. They produce current under an optical excitation when an external bias is applied. The current increases with the light illumination, corresponding to the photo-response of the detector. Mainly two types of photo-detectors are reported

in the litterature, single NW-based devices and ensemble NWs photodetectors. Single NW photodetectors are in turn divided into two categories, horizontal [66, 67], and vertical [68, 69] devices. An example of single InAs NW photodetector [66] is presented on figure I.11. The device is composed of a single InAs NW laying on a Si/SiO_2 substrate. The two ends of the NW are covered with a metal layer to form the drain and source electrode of a FET. We can see that by changing the excitation energy, different photo-responses are obtained. A cut-off wavelength of 1470 nm is observed which is the maximum cut-off wavelength for single InAs NW photodetectors.

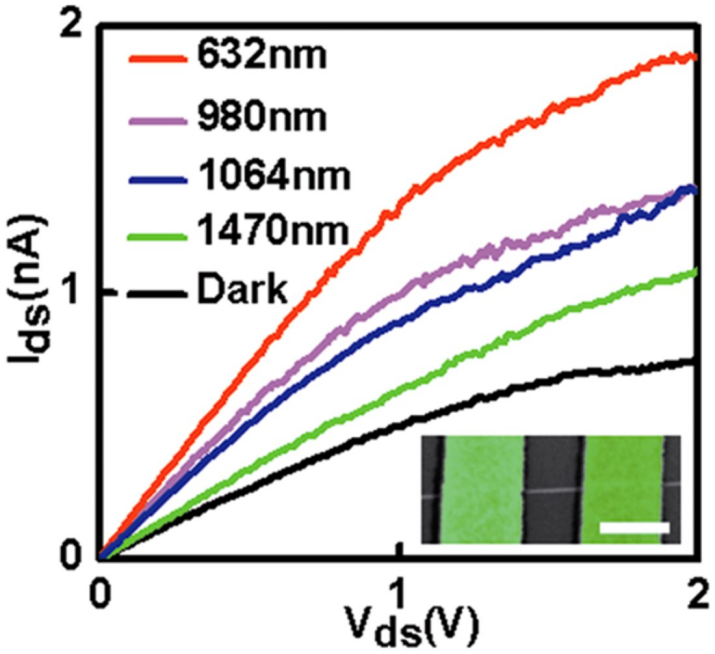

Figure I.11: I–V curves of a single InAs nanowire detector in dark and under illuminations of different frequencies. Response cut-off frequency of the single InAs nanowire detector is 1470 nm. From [66]

A way to increase the cut-off wavelength is the use of vertical NWs arrays. Using ensemble of InAs NWs, responsivity up to 3 µm has been observed [70]. The light adsorption of this type of devices can be optimized by adjusting the NWs diameter (D), length (L) and spacing (P). R.R LaPierre et al. [71] developed a model demonstrating the possibility to achieve multispectral detection by tuning NWs size and spacing. The absorptance in vertical NWs arrays is a result of three optical phenomena: radial mode resonances, near-field evanescent wave coupling, and Fabry–Perot (F–P) modes. In their work, they have detailed the effect of the different parameters D, L and P on each modes which in turn modified the absorptance wavelength. In ref. [72], the same authors reported the multispectral adsorption of InSb NWs arrays. The multispectral adsorption of such NWs arrays is shown on figure I.12-(a). We can see that experimental results are in accordance with the theoretical simulation (figure I.12-(b)). By increasing the NWs diameter, a red shift of the absorption peak is observed due to changes in the radial boundary conditions. This type of devices is of great interest, that is why multispectral absorption of InAs NWs arrays grown by HVPE will be investigated in chapter II.

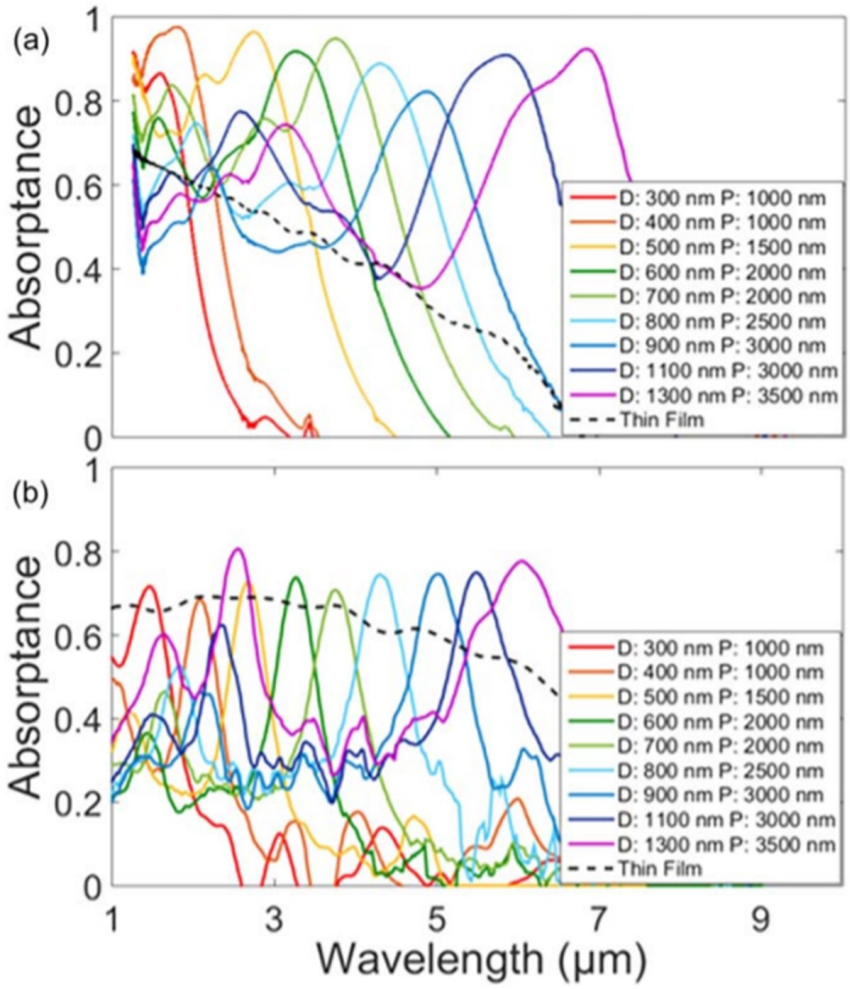

Figure I.12: (a) FTIR absorptance spectra of InSb NW arrays with the indicated diameter (D) and pitch (P). (b) Simulated absorptance spectra. From [72].

I.3.4.2 Laser application

Lasers find wide areas of applications in metrology, information transfer or even in medicine. The use of structures based on nanowires enables to consider a low threshold and a better laser emission efficiency. Because of the high surface recombination in the GaAs material, it has been difficult to observe laser emission for structures based on GaAs nanowires. However, in 2013 Saxena et al. [73] were able to show a laser effect in GaAs / AlGaAs / GaAs structures at room temperature for an excitation power of 240 μJ/cm^2. More recently, InGaAs NWs based laser, working at room temperature, has been demonstrated [11]. The NWs are grown on SOI platform to form a photonic cavity which drastically increases the optical properties of the laser (see figure I.13). The InGaAs NWs are also capped with an InGaP shell to passivate the surface, enabling a laser threshold of 15 μJ/cm^2 at room temperature.

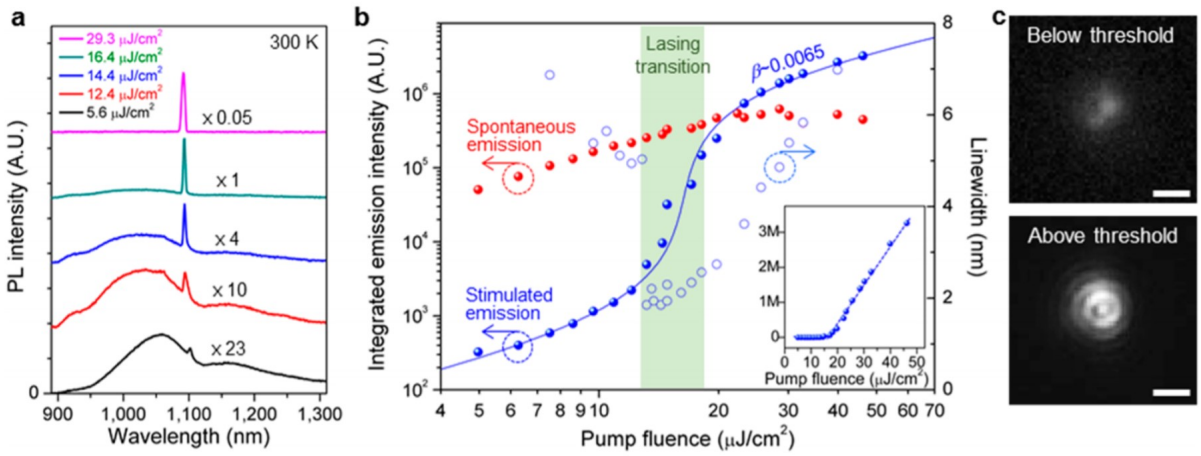

Figure I.13: a), Photoluminescence spectra of an InGaAs Nw array laser with increasing pump power, showing the transition from spontaneous emission to lasing. b), Integrated emission intensities of the stimulated emission (filled blue circle) and spontaneous emission (filled red circle), and cavity peak linewidth (open circle). S-shaped response of the stimulated output. Inset shows light-light curve of the lasing peak shown in a linear scale. c), Emission patterns measured by a commercial 2D focal plane array detector. Interference patterns are observed above the lasing threshold. Scale bars are 5 μm. From [11]

I.3.4.3 Photovoltaic application

The production of photovoltaic cells based on III-As semiconductors is a promising field of application for III-V NWs. It has been shown that by tuning the morphology of the NWs and their organization on the surface of the substrate, it is possible to obtain very large optical absorption. With arrays of NWs, it was theoretically demonstrated that by tuning the NWs diameter and pitch, it is possible to obtain light absorption equivalent to 2D material, using 10% of the total material [74]. In ref. [75], GaAs NW solar cell with p-i-n junction is demonstrated. The solar cell is composed of vertical NWs arrays as shown on figure I.14 (a). The authors have shown that large diameter and shallow p-i-n junctions are essential for a high extraction efficiency. On figure I.14 (b), we clearly see that by increasing the diameter of the NWs, the efficiency is increased. This latter increased from 0.68% for D=100 nm to 3.03% for D=250 nm.

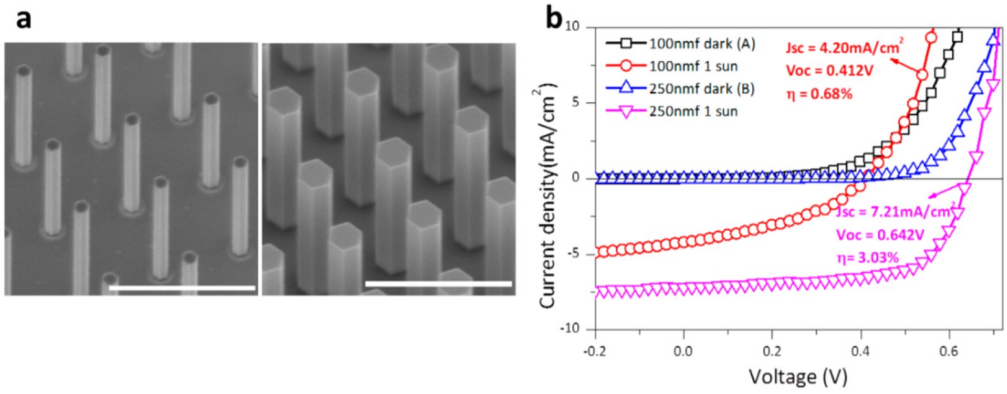

Figure I.14: Comparison between performance of NWs with 100 nm diameter and 250 nm diameter. (a) 30° tilted SEM images of NWs with diameter of 100 nm (sample A) and 250 nm (sample B). (b) I-V curves of typical devices made from 100 and 250 nm thick NWs in dark and under AM 1.5 solar spectrum. From [75].

P. Krogstrup et al. [12] have demonstrated solar cells based on vertical GaAs NW with radial p-i-n junction with an outstanding efficiency of 40%. Such efficiency is beyond the Shockley-Queisser and is explained by the far larger light absorption area than the projected crosssectional. Later, Ning Hang [76] have demonstrated single GaAs NW based solar cells for flexible photovoltaic. I(V) characteristic of such devices is shown on figure I.15. Black curve corresponds to the NWs arrays in the dark and the red curve corresponds to I(V) under illumination. The advantage of the device relied on a Schottky structure formed by an asymmetric Au-Al contact. Without any p-n doping or growth of axial heterostructures, this single NW solar cell shows a high energy conversion efficiency of 16%. Finally, the different devices presented here, clearly indicates the potential of GaAs NWs for photovoltaic application.

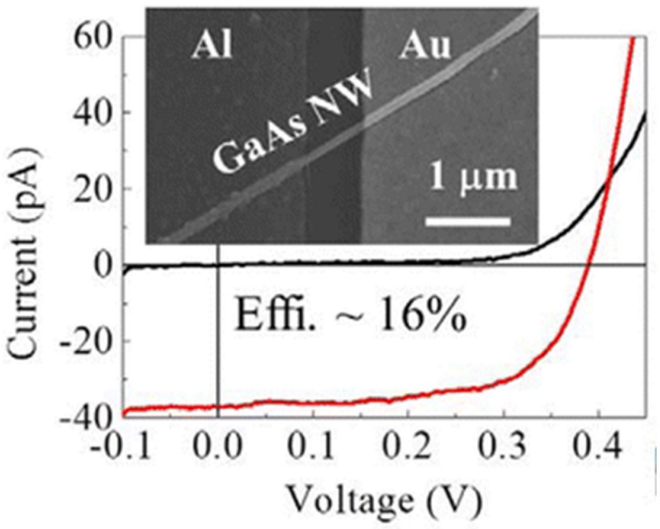

Figure I.15: SEM image of the single GaAs NW Schottky barrier solar cell using Au-Al electrodes. I-V curves of the solar cell. From [76].

Finally, the majority of devices presented in this section require specific NWs morphology with precise diameter and length. The tuning of the morphology can be achieved by a good control of the growth conditions which in turn depend on the reactor geometry. In the next section, I present the HVPE reactor used in this work and its peculiar features.

I.4 Institut Pascal: experimental setup

The reactor used in our laboratory is a home-made hot wall reactor working at atmospheric pressure. The whole reactor is made of quartz which ensures a good thermal stability even at very high temperature (up to 1000 °C). The reactor is divided into three zones, heated by a six-zone furnace. Schematic of the HVPE reactor is shown on figure I.16.

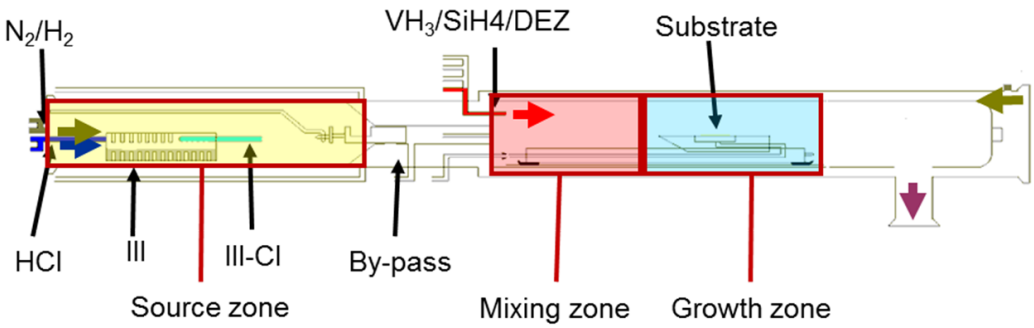

Figure I.16: Schematic of the HVPE reactor of Institut Pascal for the growth of III-V semiconductors at atmospheric pressure.

The total flow and the geometry of the reactor are adjusted to ensure a homogeneous mixture in the vapor phase and a laminar flow over the substrate. In the source zone, H_2 carrier gas is introduced and III-chloride (InCl and GaCl) gaseous species are produced by reacting HCl gas with liquid indium and gallium at 700 °C. Additionnal HCl can also be introduced in this zone to control the supersaturation of the vapor phase during the growth. The supersaturation is a very important parameter in HVPE and will be detailed in the next section. Arsine gas (AsH_3) is introduced in the downstream mixing zone of the reactor heated at higher temperature, to ensure a homogeneous mixing of the gas phase and reduce parasitic nucleation upstream of the substrate, since the reactions involving chloride molecules are exothermic. Doping during growth is also possible by introducing SiH_4 and diethyle zinc (DEZ) in this zone. The source and the mixing zones are connected through a drawer-valve which is manually controlled. It enables the preparation of the different species without

any unwanted deposition upstream of the substrate. The third zone is the deposition zone which is maintained at the lowest temperature so that the reaction is favored on the substrate.

Finally, knowing the temperature profile and the gas transport in the reactor, we are able to determine growth conditions leading to the growth of InAs, GaAs and InGaAs materials. This is the topic of the following section.

I.5 Thermodynamic study of (In,Ga)As condensation in HVPE environment

HVPE is a near-equilibrium process which involves GaCl and InCl precursors of elements III and AsH_3/As_2/As_4 as precursors of elements V. Thermodynamic calculations enable to determine which gaseous species interact with the substrate surface, especially for arsine (AsH_3) that decomposes into As_2/As_4 when entering the hot wall reactor. Thermodynamics of the global deposition reaction enables to know if either growth or etching of the solid will occur.

I.5.1 Vapor phase composition

Partial pressures of the different gaseous species in the growth zone are calculated as a function of the flows of the gas introduced in the reactor. The partial pressures obtained are used to predict the optimal conditions for a better control of the growth of the ternary InGaAs.

I.5.1.1 Formation of III-Cl precursors

In the source zone, III-chloride (GaCl and InCl) gaseous species are produced by reacting HCl gas with liquid indium and liquid gallium heated at 730 °C. The corresponding reaction is written:

$$In_l + HCl_g \rightleftharpoons InCl_g + \frac{1}{2}H_{2g} \qquad (R1)$$

V. S. Ban showed that the reactions of gaseous HCl with liquid indium or gallium produce only the mono-chloride species for temperature above 725 °C. Thus we consider that only InCl is present in the vapor phase. We can notice that H_2 is a product of the reaction. It is also essential to know the yield of the reaction to calculate the number of HCl molecules that do not react with the liquid. It mainly depends on the gas speed and the source temperature. In our case, the gas speed is equal to 0.1 cm/s which is sufficiently low to consider that any material input (HCl_g on In_l) pushes the reaction towards equilibrium. Thus we can introduce the equilibrium constant of the reaction (R1) as following:

$$K_{InCl} = \frac{[InCl]_1 \times [H_2]_1^{1/2}}{[HCl]_1} \tag{I.1}$$

$[InCl]_1$ is the InCl partial pressure at the exit of the liquid indium cell (labelled 1).

Knowing the input flow rates of HCl and H_2 (d^{in}_{HCl} and $d^{in}_{H_2}$) we are able to calculate the partial pressures at the source output using the principle of conservation of the different species H and Cl.

For the H atoms:

$$d^{in}_{HCl} + 2d^{in}_{H_2} = d_1(2[H_2]_1 + [HCl]_1) \tag{I.2}$$

For the Cl atoms:

$$d^{in}_{HCl} = d_1([HCl]_1 + [InCl]_1) \tag{I.3}$$

With d_1, the total flow rate at the source output.

The total pressure is equal to atmospheric pressure and is also equal to the sum of the partial pressures at the outlet of the In source. Thus we can write:

$$[HCl]_1 + [InCl]_1 + [H_2]_1 = 1 \tag{I.4}$$

The system constituted by the equations (1), (2), (3) and (4) can be solved using the iterative method of Newton. It enables the calculation of the partial pressures of the different species $[InCl]_1$, $[HCl]_1$ and $[H_2]_1$ and the flow rate d_1 at the outlet of the source.

The same method is applied to the Ga source to calculate $[GaCl]_2$, $[HCl]_2$ and $[H_2]_2$ and d_2 respectively the partial pressures of $GaCl$, HCl and H_2 and the flow rate at the outlet of the Ga source.

I.5.1.2 AsH_3 decomposition

The cracking of AsH_3 occurs in the hot tube that carries the V species in the central zone of the reactor. The reaction of decomposition is given by:

$$AsH_{3g} \rightleftharpoons \frac{1}{2}As_{2g} + \frac{3}{2}H_{2g} \tag{I.5}$$

As_{2g} species are in equilibrium with As_{4g} following the equation:

$$\frac{1}{2}As_{2g} \rightleftharpoons \frac{1}{4}As_{4g} \tag{I.6}$$

In order to calculate the partial pressures resulting from the AsH_3 cracking, we introduce the cracking yield r_{As}. It is given by:

$$r_{As} = 1 - \frac{N_{AsH_{3g}}}{N^{in}_{AsH_{3g}}} \tag{I.7}$$

Where N_{AsH_3} is the number of undecomposed AsH_3 at the output of the tube and $N^{in}_{AsH_3}$ is the number of AsH_3 molecules introduced in the reactor. For temperatures above 600 ° C, the thermodynamic study predicts an almost complete decomposition or "cracking" of arsine following reaction I.5. We can write:

$$N_{AsH_{3g}} = (1 - r_{As}) N^{in}_{AsH_{3g}} \tag{I.8}$$

$$N_{As_{2g}} = \frac{1}{2} r_{As} N^{in}_{AsH_{3g}} \tag{I.9}$$

$$N_{H_{2g}} = \frac{3}{2} r_{As} N^{in}_{AsH_{3g}} + N^{in}_{H_{2g}} \tag{I.10}$$

Using the principle of conservation of arsenic species, we deduce the flow rate (d_3) at the tube outlet:

$$d_3 = (1 + r_{As}) d^{in}_{AsH_3} + d^{in}_{H_2} \tag{I.11}$$

d^{in}_j is the flow rate of the introduced species j.

Thus we can calculate the partial pressures of AsH_{3g}, As_{2g} and H_{2g} at the tube outlet as a function of d_3:

$$[AsH_3]_3 = (1 - rAs) d^{in}_{AsH_3} / d_3 \tag{I.12}$$

$$[As_2]_3 = \frac{1}{2} r_{As} d^{in}_{AsH_3} / d_3 \tag{I.13}$$

$$[H_2]_3 = (\frac{3}{2} r_{As} d^{in}_{AsH_3} + d^{in}_{H_2}) / d_3 \tag{I.14}$$

I.5.1.3 Partial pressures in the growth zone

Knowing the partial pressures and the flow rates of species arriving from the source zone and the arsenic tube, we are able to calculate the partial pressures and the total flow rate (d_T) in the growth zone by solving the following system of equations:

$$d_1 [InCl]_1 = d_T [InCl] \tag{I.15}$$

$$d_2[GaCl]_2 = d_T[GaCl] \tag{I.16}$$

$$d_1[HCl]_1 + d_2[HCl]_2 + d_{HCl_{add}} = d_T[HCl] \tag{I.17}$$

$$d_3([AsH_3]_3 + 2[As_2]_3 + 4[As_4]_3) = d_T([AsH_3] + 2[As_2] + 4[As_4]) \tag{I.18}$$

$$d_3[AsH_3]_3 = d_T[AsH_3] \tag{I.19}$$

$$K_{As}(T_d) = \frac{[As_4]^{\frac{1}{4}}}{[As_2]^{\frac{1}{2}}} \tag{I.20}$$

$$2d_1[H_2]_1 + 2d_2[H_2]_2 + d_3(2[H_2]_3 + 3[AsH_3]_3) + 2d_{H_{2vecteur}} = d_T(2[H_2] + 3[AsH_3]) \tag{I.21}$$

$$[InCl] + [GaCl] + [AsH_3] + [As_2] + [As_4] + [HCl] + [H_2] = 1 \tag{I.22}$$

This system is solved using the iteration method of Newton. Variations of the partial pressures involved in InGaAs growth are given as a function of temperature in figure I.17.

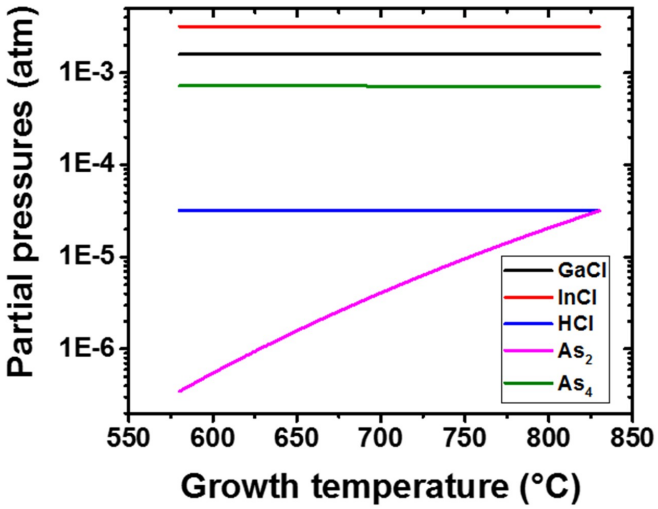

Figure I.17: Variations of the different partial pressures in the growth zone as a function of growth temperature.

We can see that the InCl, GaCl, HCl and As_4 partial pressures are constant over the temperature range. The partial pressure of As_2 species, which is in equilibrium with As_4, increases with the temperature. However, its value is very low compared to As_4. Then only As_4 species will be consider for the growth of InAs, GaAs and InGaAs in this work. Once the partial pressures are determined, we can calculate the III/V ratio which is defined as following:

$$III/V = \frac{P_{III-Cl}}{P_{As_4}}$$

In this manuscript, we will discuss results as a function of this III/V ratio, calculated as the ratio between the partial pressures of gaseous InCl and GaCl over the partial pressure of gaseous As4 interacting with the substrate surface in the growth zone.

I.5.2 Thermodynamics of InGaAs reaction

Knowing the composition of the vapor phase at equilibrium, we now focus on the reaction of condensation from this vapor phase. We study the thermodynamic of the reactions leading to the growth of InGaAs by considering that ternary InGaAs is a solid crystal solution of binaries InAs and GaAs. The development of the chemical potential will enables the introduction of the interaction parameter between InAs and GaAs in the solid.

The condensation of InAs and GaAs can be described by the following reactions:

$$InCl_g + \frac{1}{4}As_{4_g} + \frac{1}{2}H_{2_g} \rightleftharpoons InAs_s + HCl_g \tag{I.23}$$

$$GaCl_g + \frac{1}{4}As_{4_g} + \frac{1}{2}H_{2_g} \rightleftharpoons GaAs_s + HCl_g \tag{I.24}$$

The reactions are considered at thermodynamic equilibrium. Thus we can write the equality of the chemical potentials of each reaction to calculate their respective equilibrium constants. We will focus on InAs deposition as an example, given that the same treatment could be applied to GaAs deposition.

Using the equality of the chemical potentials we can write:

$$\mu_{InAs} + \mu^0_{HCl_g} - \mu^0_{InCl_g} - \frac{1}{4}\mu^0_{As_{4g}} - \frac{1}{2}\mu^0_{H_{2g}} = +k_B T_D ln\left(\frac{[As_4]^{1/4}_{eq}[H_2]^{1/2}_{eq}[InCl]_{eq}}{[HCl]_{eq}}\right) \tag{I.25}$$

$\mu^0_{i_g}$ is the standard chemical potential of species i at equilibrium.

Then the equilibrium constant for InAs deposition is defined as:

$$K^{eq}_{InAs}(T_D) = \left(\frac{[As_4]^{1/4}_{eq}[H_2]^{1/2}_{eq}[InCl]_{eq}}{[HCl]_{eq}}\right) \tag{I.26}$$

T_D is the temperature in the growth zone.

In the ternary alloy InGaAs, Ga and In atoms are distributed in the sub-lattices of the elements III. The alloy is considered as a pseudo-binary A_xB_{1-x} where A and B are InAs and GaAs, respectively. The interaction energy between atoms of the AB alloy is calculated using the mean-field approximation of Bragg-Williams:

$$E = \frac{N_A}{2} j\phi_{AA} + \frac{N_B}{2} j\phi_{BB} + \nu_{AB}\phi$$

N_A and N_B are the numbers of atoms A and B, respectively. j is the number of first neighbours atoms, and ν_{AB} is the number of A-B bonds in the structure. ϕ_{lm} is the potential energy of interaction between one atom l and one atom m:

$$\phi = \phi_{AB} - \frac{\phi_{AA} + \phi_{BB}}{2} \tag{I.27}$$

We can also write E as following:

$$E = E_0 + \nu_{AB}\phi \tag{I.28}$$

where E_0 is independent of the atomic distribution.

The number of A-B bonds in the alloy A_xB_{1-x} is given by:

$$\nu_{AB} = xNj(1-x) = N_A j\left(1 - \frac{N_A}{N_A + N_B}\right) \tag{I.29}$$

with N the total number of atoms.

The chemical potential of the atom A is defined using the variation of the free energy F of the system:

$$\mu_A = \left(\frac{\partial F}{\partial N_A}\right)_{N_B} \tag{I.30}$$

where $F = -k_B T ln(Z)$ and Z is the partition function of the system at equilibrium, given by:

$$Z = \frac{N!}{N_A!(N - N_A!)} exp\left(-\frac{E}{k_B T_D}\right) \tag{I.31}$$

Then:

$$\mu_A = \frac{j}{2}\phi_{AA} + j.\phi(1-x)^2 + k_B T_D ln(x) \tag{I.32}$$

with x, the A content in the alloy.

The chemical potential is described by the sum of a standard potential of material A without any interaction (μ_A^*) and an interaction term within the ternary alloy. We defined the interaction parameter the activity coefficient α_A of A in the alloy A_xB_{1-x} by:

$$\alpha_A = exp\left(\frac{(1-x)^2 j\phi}{k_B T_D}\right) = exp\left(\frac{(1-x)^2 \Omega}{k_B T_D}\right) \tag{I.33}$$

with $\Omega = j\phi$, the energy interaction parameter.

Then: $\mu_A = \mu_A^* + k_B T ln(x\alpha_A)$

The same approach is used for the binary B. Its chemical potential in the alloy A_xB_{1-x} is given by:

$$\mu_B = \mu_B^* + k_B T_D ln((1-x)\alpha_B) \tag{I.34}$$

with

$$\alpha_B = exp\left(\frac{x^2 \Omega}{k_B T_D}\right) \tag{I.35}$$

With these considerations, we can write the variation of the chemical potential of the binaries InAs and GaAs in the alloy $In_xGa_{1-x}As$:

$$\Delta\mu_{InAs} = \mu^*_{InAs_s} + \mu^0_{HCl_g} - \mu^0_{InCl_g} - \frac{1}{4}\mu^0_{As_{4g}} - \frac{1}{2}\mu^0_{H_{2g}} - k_B T_D ln(Q_{InAs}(x, T_D)) \tag{I.36}$$

$$\Delta\mu_{GaAs} = \mu^*_{GaAs_s} + \mu^0_{HCl_g} - \mu^0_{GaCl_g} - \frac{1}{4}\mu^0_{As_{4g}} - \frac{1}{2}\mu^0_{H_{2g}} - k_B T_D ln(Q_{GaAs}(x, T_D)) \tag{I.37}$$

where:

$$Q_{InAs}(x, T_D) = \frac{[InCl][As_4]^{1/4}[H_2]^{1/2}}{[HCl]x\alpha_{InAs}} \tag{I.38}$$

and

$$Q_{GaAs}(x, T_D) = \frac{[GaCl][As_4]^{1/4}[H_2]^{1/2}}{[HCl](1-x)\alpha_{GaAs}} \tag{I.39}$$

with $[i]$, the partial pressure of species i interacting with the substrate during growth.

Condensation (growth) or sublimation is determined considering the variation of the free enthalpy $\Delta\mu$, defined by the extent of the reaction of deposition with respect to its equilibrium:

$$\Delta\mu = \mu^0_{products} - \mu^0_{reactants} - k_B T_D ln\left(\frac{a_{reactants}}{a_{products}}\right) \tag{I.40}$$

$a_{reactants}$ and $a_{products}$ are the reactants' activity and the products' activity of the reaction.

At equilibrium, $\Delta\mu = 0$ thus:

$$\Delta\mu^0 = k_B T_D ln\left(\frac{a_{reactants}}{a_{products}}\right)_{equilibrium} \tag{I.41}$$

The extent of reaction reads:

$$\Delta\mu = k_B T_D ln\left(\frac{(a_{reactants}/a_{products})_{equilibrium}}{(a_{reactants}/a_{products})}\right) \tag{I.42}$$

As written, negative $\Delta\mu$ means that growth occurs.

The supersaturation of the vapor phase γ is related to the thermodynamic force to restore equilibrium, that is the excess of chemical potential with respect to equilibrium of the reaction at temperature T_D:

$$\Delta\mu = -k_B T_D ln(1+\gamma) \tag{I.43}$$

Then:

$$\Delta\mu < 0 \quad \Rightarrow \quad \gamma > 0 \tag{I.44}$$

Thus, γ is the parameter used to measure the deviation of the reaction from its equilibrium. Depending on its sign, we can predict if the growth is favored or not:

$\gamma = 0$ refers to equilibrium between the vapor phase and the solid.

$\gamma > 0$ corresponds to the formation of the solid.

$\gamma < 0$ corresponds to the etching of the solid.

The relative supersaturations of the vapor phase related to InAs and GaAs are given by:

$$\gamma_{InAs}(x, T_D) = \frac{[InCl][As_4]^{1/4}[H_2]^{1/2}}{[HCl]x\alpha_{InAs}} \frac{1}{K^{eq}_{InAs}(T_D)} - 1 \tag{I.45}$$

$$\gamma_{GaAs}(x, T_D) = \frac{[GaCl][As_4]^{1/4}[H_2]^{1/2}}{[HCl](1-x)\alpha_{GaAs}} \frac{1}{K^{eq}_{GaAs}(T_D)} - 1 \tag{I.46}$$

The supersaturations at T_D=715 °C as a function of the HCl flux on the indium source are shown figure I.18. The full lines correspond to the supersaturations of the binaries binary. The dashed lines correspond to the supersaturations considering a ternary alloy InGaAs with an indium composition of 0.85. This specific composition is an experimental point which will be discussed in chapter 3.

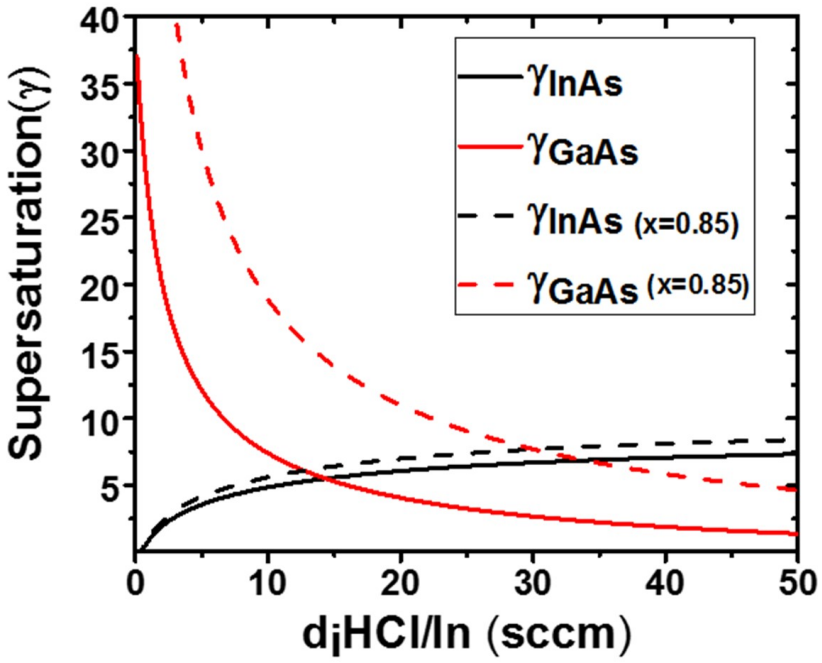

Figure I.18: Variations of InAs and GaAs supersaturations as a function of the HCl flow above the indium source.

First we clearly see a drastic variation of γ_{GaAs} when we increase the HCl flux on the indium source. An increase of the HCl flux on the indium source results in an increase of the residual HCl in the growth zone which leads to reduce γ_{GaAs}. The residual HCl also enables to explain the slow increase of γ_{InAs}. In fact the InCl increase is counterbalanced by HCl increase. In the ternary alloy $In_{0.85}Ga_{0.15}As$ we observe the same behaviour, however the values of γ_{GaAs} and γ_{InAs} are higher than in the binaries InAs and GaAs. Indeed, the activities of InAs and GaAs have lower values when considering the interaction parameter Ω in the ternary material.

I.5.3 Comparison with MOVPE and MBE

Earlier, we briefly introduced the HVPE process as a near-equilibrium process, here we will further detailed this property and explained why it can be an advantage to grow InGaAs crystal. The equilibrium constant for the reaction of condensation can be written as a function of the Gibbs free energy difference between reactants and products:

$$K^{eq}_{III-As} = exp\left(-\frac{\Delta G(T)}{k_B T}\right)$$

$\Delta G(T)$ is calculated from the thermodynamic data of the heat capacities of the species involved in the reaction at temperature T. Within this framework, we can now discuss the notion of near-equilibrium process. Considering GaAs growth and according to Stringfellow's work [77], MOVPE and MBE exhibit $\Delta G(T)$ that is approximately eight times higher than for HVPE at 1000 K. As shown in figure I.19, comparing with the extremely non-equilibrium techniques MOVPE and MBE, the thermodynamic driving force for growth by HVPE is relatively small.

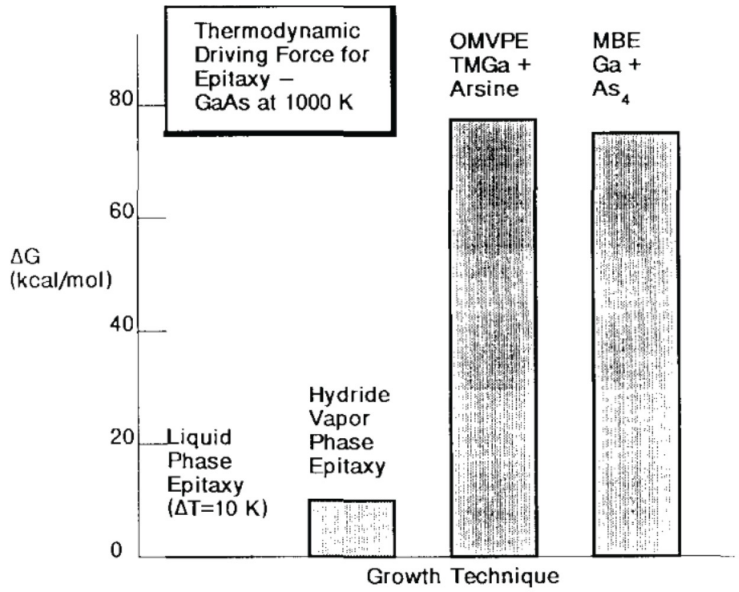

Figure I.19: Estimated thermodynamic driving force, Gibbs free energy difference between reactants and products, for several epitaxial growth processes. All calculations are for the growth of GaAs at 1000 K. From [77].

One point of view is to say that when the thermodynamic driving force for growth is small, then the process operates at near-equilibrium conditions: thermodynamics governs or limits growth. According to Stringfellow [77], MOVPE can be controlled by thermodynamic factors despite high supersaturation of the input vapor phase: near-equilibrium conditions may prevail near the solid–vapor interface because of mass transport limitation to the substrate surface. In that case, the growth is considered to proceed at near-equilibrium because there is a small supersaturation interacting with the surface.

In the HVPE system, surface kinetics and mass transport are fast enough to establish equilibrium at all times. On increasing the supersaturation, dechlorination frequency is high enough to avoid kinetic limitation; the return to equilibrium, which produces the solid, takes place quickly [78]. On decreasing the supersaturation, a reversible process occurs at the interface due to the volatility of the chlorides. This feature characterizes a near-equilibrium process, which gives the interesting possibility of modulating the growth rate by varying the mass input rate of the reactants. Then in the case of InGaAs, for which the composition is a function of the growth rate of the InAs and GaAs binaries in the ternary, its composition can be tuned by simply changing the InCl and GaCl partial pressures. Finally, it should be possible to grow InGaAs material using HVPE, while covering the full range of

composition.

Thermodynamics provides access to the experimental conditions (temperature and composition of the vapor phase) that promote growth. It must be completed by a kinetic study and modelling in order to assess the actual growth rate of the deposition reaction.

I.6 Kinetics aspect of HVPE process

R. Cadoret, A. Pimpinelli and E. Gil [79] have developed a kinetic model describing the homoepitaxial growth of GaAs on GaAs(100) substrate. In this model, the global growth reaction is decomposed into three steps: (1) adsorption of group III and V atoms on the surface, (2) dechlorination step where several mechanisms are proposed as a function of the vapor phase composition and temperature and (3) the diffusion of the ad-atoms to the nucleation sites in the semi-crystal. The reaction starts with the adsorption of arsenic atoms on the vacant sites of the surface (figure I.20). Then GaCl molecules are adsorbed on the surface, resulting in the formation of a stable chemisorbed As-GaCl complex. The final step is the chlorine desorption from the As-GaCl complex. This step determines the kinetics of the whole process since it is the slowest step. Two different mechanisms are proposed to describe the dechlorination. The first one is the desorption of the Cl atom as HCl_g with the help of H_{2_g}. The second one consists in the adsorption of a second layer of GaCl, follow by the desorption of $GaCl_3$. This second mechanism takes place when the adsorption of GaCl molecules is very high. In this work the growth conditions used to grow GaAs and InAs correspond to growth governed by the first H_2 mechanism represented in figure I.20-(a).

The different steps described in figure I.20-(c) can be written as follows:

$$4V + As_{4g} \rightleftharpoons 4As \tag{I.47}$$

$$As + GaCl_g \rightleftharpoons AsGaCl \tag{I.48}$$

$$AsGaCl + H_{2g} \rightleftharpoons AsGa_c + HCl_g + \frac{1}{2}H_{2g} \tag{I.49}$$

Where V represents a vacant site, the index g and c indicate gaseous species and incorporated crystal respectively.

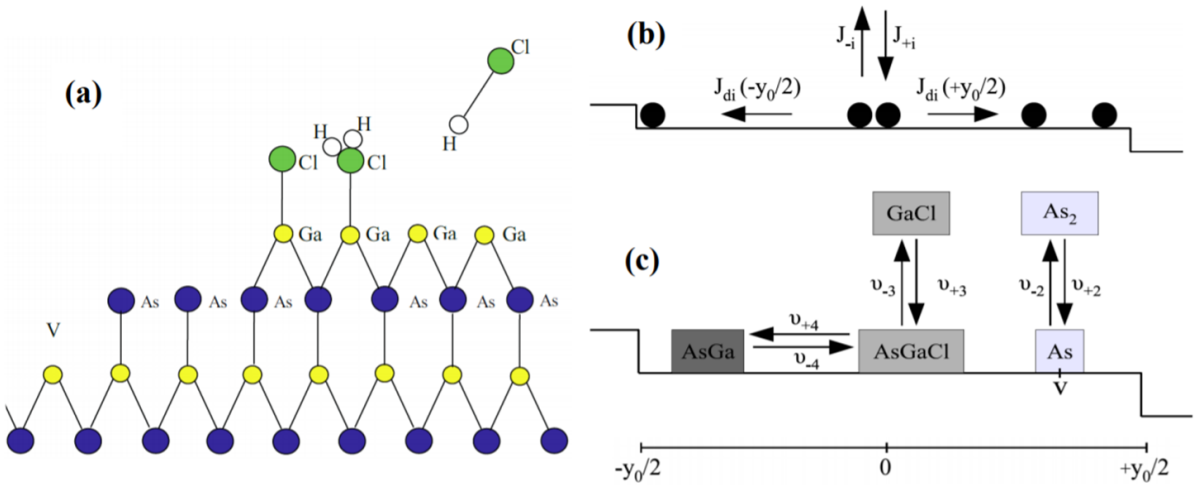

Figure I.20: a) Scheme of H_2-AsGaCl ad-species dechlorination mechanism, V is a vacant site. b) Scheme of the surface processes for the step-flow growth modeling on a vicinal substrate presenting terraces of width equal to y_0. c) Schematic steps of GaAs growth from $GaCl_g$ and As_{4g}. Adsorption and desorption frequencies of As and GaCl are represented as ν_{+2}, ν_{-2}, ν_{+3} and ν_{-3} (from reactions 1.47 and 1.48), and ν_{+4} as dechorination frequency, ν_{-4} as chlorination frequency (reaction I.49).

The kinetic model is based on the near-field approximation of Eyring's theory that allows the calculation of adsorption flux J_{+i} and desorption flux J_{-i} of molecules i. The fluxes are function of the activation energies and the partial pressures of the different gaseous species. The model also takes into account the diffusion flux J_{di} towards the incorporation sites at the steps on the surface, (see figure I.20-(b)).

The adsorption flux of species i is written as $J_{+i} = k_{+i} F_i \theta vacant$

where

F_i is the mass input considered as element i's partial pressure, $\theta vacant$ is the surface coverage ratio in vacant sites and k_{+i} is a kinetic constant defined as:

$k_{+i} = C_{+i}(T) exp\left(-\frac{E_{+i}}{k_B T}\right)$ with $C_{+i} = \frac{1}{\sqrt{2\pi m_i k_B T}}$, the classical Hernst-Knudsen term.

The desorption flux of species i is given by: $J_{-i} = k_{-i} \theta i$

with

θi: the surface coverage of occupied sites with i-type ad-species, and $k_{-i} = C_{-i}(T) exp\left(-\frac{E_{-i}}{k_B T}\right)$ with $C_{-i}(T) \propto \Pi z$ written with the partition functions z of the species involved in the desorption process.

Thus, the net adsorption flux of species i can be written as a function of the difference between its respective adsorption and desorption fluxes:

$J_i = J_{+i} - J_{-i}$

Concerning the diffusion of ad-atoms, we consider that the surface is composed of steps and terraces (see figure I.20-(b)). The height of the steps corresponds to a monolayer. The width of the terraces is denoted y_0. We assume that the diffusion of the ad-species is faster than the steps progression which are supposed to be stationary (quasi-static hypothesis). Then we can use the equation of conservation of matter for element i to link its surface diffusion flux and the surface-vapor dynamics:

$$div(J_{di}) = J_i - J_{i+1} \tag{I.50}$$

J_{di} represents the diffusion flux of the ad-species i towards the edge of the step. J_{i+1} corresponds to the consumption of the species i during the reaction $i+1$, where $i+1$ adsorbs on species i according to the net adsorption flux J_{i+1}.

It gives:

$$div(J_{d_{As}}) = J_{As} - J_{As+1} = (J_{+As} - J_{-As}) - (J_{+AsGaCl} - J_{-AsGaCl}) \tag{I.51}$$

which reads:

(As adsorbing on vacant site of the surface) - (As disappearing because covered by GaCl)

$$div(J_{d_{AsGaCl}}) = J_{AsGaCl} - J_{AsGaCl+1} = (J_{+AsGaCl} - J_{-AsGaCl}) - (J_{+GaAs} - J_{-GaAs}) \tag{I.52}$$

which reads:

(GaCl adsorbing on As) - (AsGaCl disappearing because of Cl desorption)

Finally, for GaAs there is only one term:

$$div(J_{d_{GaAs}}) = J_{GaAs} = J_{+GaAs} - J_{-GaAs} \tag{I.53}$$

J_{d_i} is expressed by Fick's law considering the surface concentration C_i of ad-species i:

$$J_{di} = -D_i \frac{\partial C_i}{\partial y} \tag{I.54}$$

Where $C_i = N_S \theta_i$. with N_S is the number of sites per surface unit, and D_i is the diffusion coefficient of ad-species i.

We now introduce the adsorption and desorption frequencies ν_{+i} and ν_{-i} respectively. These frequencies are illustrated in figure I.20-(c). They are written as follows:

$$\nu_{\pm i} = \frac{J_{\pm i}}{C_i} \tag{I.55}$$

This enables to write the following system of coupled equations:

$$\nu_{+3}C_{As} - \nu_{-3}C_{AsGaCl} - (\nu_{+4}C_{AsGaCl} - \nu_{-4}C_{GaAs}) = -D_{AsGaCl}\frac{\partial^2 C_{AsGaCl}}{\partial^2 y} \tag{I.56}$$

$$\nu_{+4}C_{AsGaCl} - \nu_{-4}C_{GaAs} = -D_{GaAs}\frac{\partial^2 C_{GaAs}}{\partial^2 y} \tag{I.57}$$

Then by considering the time needed to cover the terraces, we are able to determine the growth rate V:

$$V = \frac{h}{t} = h\frac{\dot{y}}{y_0} = \frac{\Omega}{y_0}\left[D_{GaAs}\left|\frac{\partial C_{GaAs}}{\partial y}\right|_{-\frac{y_0}{2}} - D_{GaAs}\left|\frac{\partial C_{GaAs}}{\partial y}\right|_{+\frac{y_0}{2}}\right] \tag{I.58}$$

with h the step height, $t = \frac{y_0}{\dot{y}}$ the time for covering one terrace and Ω the molecular volume of GaAs.

The solution of the system I.56 and I.57 enables the calculation of the concentration of solid C_{GaAs}. This value is then introduced in equation I.58 in order to calculate the growth rate. The variation of the growth rate as a function of the growth temperature is shown figure I.21.

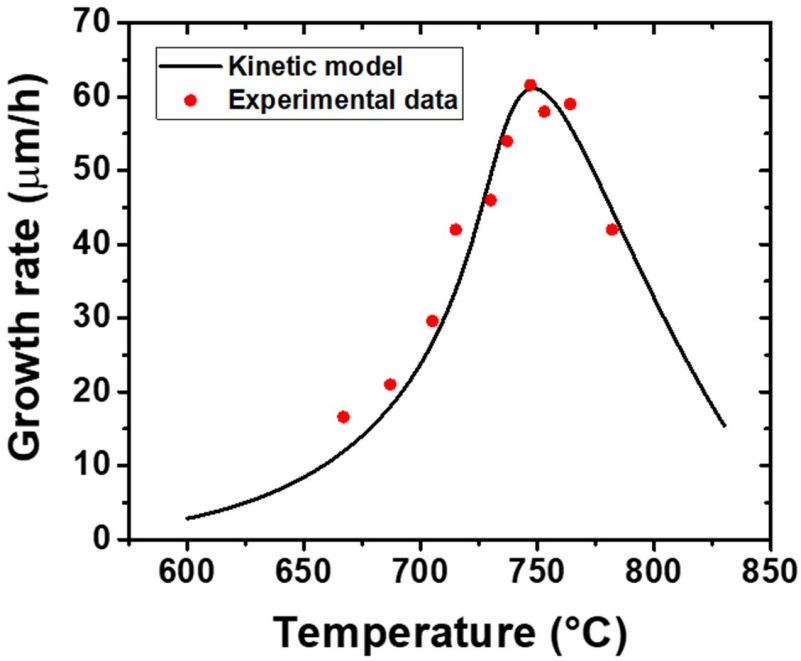

Figure I.21: (001) GaAs growth rate R in µm/h as a function of the growth temperature T for standard experimental conditions (III/V=4.5, γ=4). The dots are the experimental points; the full line is the computed theoretical curve according to the kinetic model.

At low temperature, growth is limited by dechlorination of GaCl ad-molecules, desorption and surface diffusion of ad-species, which are inhibited. The surface is then blocked with undecomposed

AsGaCl species. This low temperature domain was defined by Shaw [80] as the kinetically limited regime. When the temperature increases, the dechlorination frequency of GaCl ad-molecules increases. Then the surface is no further saturated and the number of adsorption sites increases. Thus, growth rate increases up to a maximum that takes place at 750 °C, which is predicted by the thermodynamic study. At high growth temperatures, HVPE exhibits the thermodynamically controlled growth regime and the growth rate is determined by the material input rate of the precursors [80]. On the high temperature side of the curve, desorption of GaCl becomes predominant and the growth rate decreases.

In the next chapter, we focus on the HVPE input to the growth of InAs nanowires. Synthesis of InAs nanowires was the first objective of this thesis work. I could rely on the complete study of GaAs NWs HVPE-growth on GaAs substrate performed at Institut Pascal, to investigate growth of InAs and further InGaAs NWs (chapter III). In chapter II, modelling of InAs NWs growth will be described according to the thermodynamic and kinetic approaches that have been presented here. Second objective was to develop and consolidate growth of GaAs and InAs NWs on silicon substrate, that will be find in chapter II.

Chapter II

InAs and GaAs nanowires grown by HVPE

II.1 Introduction

Devices based on III-As nanowires arrays exhibiting homogeneous electrical and optical properties require a good control of the nanowires morphology over a large substrate's surface. This can be achieved by a high control of the vapor phase and a good understanding of the mechanisms involved during growth. In this chapter, a complete study of InAs and GaAs NWs grown on different substrates is conducted. First, I demonstrate the growth of InAs nanowires on bare Si(111) substrates. An experimental study as a function of growth parameters is carried out to reveal the steps and the mechanisms involved in the growth of the NWs. The observed experimental trends are supported by kinetic and thermodynamic considerations. I also discuss about the surface treatment of Si(111), which appears to be critical for NWs nucleation. A surface treatment under AsH_3 was developed and applied for the selective area growth (SAG) of InAs and GaAs crystals. The study of InAs and GaAs SAG highlights the effect of the growth parameters and mask's openings on the crystal morphology. The crystalline quality of InAs and GaAs materials were checked by HRTEM analysis and PL measurements. Suitability of InAs NWs arrays for infra-red multispectral photodetection is also demonstrated through FTIR measurement. It is shown that wavelength of maximum absortpance is shifted by varying the NWs diameter and the pitch of the arrays.

II.2 Self-induced growth of InAs nanowires on Si(111) substrate

As shown in chapter I, the growth of InAs NWs has been widely studied by MBE and MOVPE, however the presence of defects in the crystal is still an issue. With the peculiar properties of the HVPE process (high growth temperature, high mass input), it was interesting to determine if defects-free InAs NWs could be grown using HVPE. The study of InAs NWs growth was also initiated by our collaboration with Prof. Dubvroskii who has previously developed theoretical models of the growth of GaAs NWs and nitride NWs using HVPE.

The growth of InAs material has already been studied at Institut Pascal in the 90's in form of 2D planar layers. For more than 20 years, the research were then focused on GaAs. The first task was to install the metallic indium source in the reactor. As growth of gold-catalysed GaAs NWs by HVPE is now well understood, the first idea was to grow gold catalysed InAs NWs. However, after few experiments, I observed growth of InAs structures on Si(111) substrates. Thus, I decided to focus my work on the optimization of InAs growth on Si(111) without the use of gold catalyst.

II.2.1 Experimental conditions

In this part, I use non-intentionally doped Si(111) substrates covered with a 10 nm oxide layer which was thermally grown (using dry oxidation method). Before growth, the samples are etched with 1% diluted hydrofluoric (HF) acid for 10 minutes to remove the oxide layer, then they are rinsed in deionised water and finally blow dried with N_2. These cleaned substrates are introduced in the HVPE reactor. As_4 and InCl are used as gaz precursors of element V and III, respectively. H_2 is used as carrier gas during growth. The source zone is kept at a temperature of 700 °C to ensure a constant yield of InCl formation. The growth temperature is ranged between 580 °C and 715 °C. The temperature of the central zone is adjusted to a hot point for each temperature profile, to ensure the stability of the vapor phase composition in the growth zone and avoid parasitic nucleation upstream the substrate.

II.2.2 Effect of the growth parameters on nanowires morphology

In crystal growth, Wulff construction is usually used to explain the final morphology of the crystal. It links the growth rate of the different facets to the surface energy anisotropy. During growth, each facet has its own kinetics of diffusion, adsorption and desorption, driven by the growth conditions. Therefore, I decided to study the effect of the growth parameters on the NWs morphology. First, I had to find the growth conditions giving satisfying results in terms of NWs nucleation density and morphology. Starting from this point, I varied the growth parameters, i.e additional HCl, growth temperatures and III/V ratio.

II.2.2.1 Effect of additional HCl

In figure II.1, InAs structures with a high aspect ratio are shown. The growth conditions used for this growth correspond to standard conditions generally used to grow GaAs material, ($P_{InAs} = 6.4 \times 10^{-3}$ atm, $P_{As_4} = 3.6 \times 10^{-4}$ atm). The growth temperature is 640 °C corresponding to the one previously established by the laboratory [81] to grow InAs 2D layers. P_{HCl} was 7×10^{-4} atm for figure II.1-(a) and 3.6×10^{-5} atm for figure II.1-(b). Additional HCl in HVPE is a powerful tool to increase or decrease the supersaturation γ (equation I.45, chapter I) which is the key parameter to control the growth rate. Moreover, adding additional HCl allows to neglect the effect of the residual HCl coming from the indium source. In fact, this residual HCl partial pressure is 20 times lower than $P_{HCl_{add}}$.

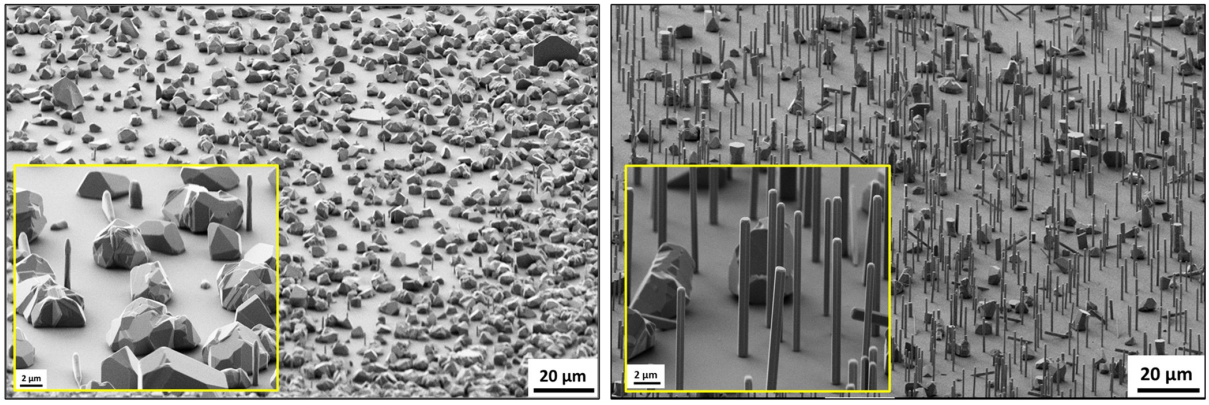

Figure II.1: Tilted-view SEM images of InAs crystals grown on Si(111) at 640 °C, with additional HCl_{add} flow (a), and without HCl_{add} flow (b) introduced in the reactor.

For the growth with additional HCl (figure II.1-(a)), few NWs grow together with InAs crystallites. The NWs have a length of 6 μm and a diameter of 600 nm. They grow along the (111)B direction. III-As NWs growing along the (111)B direction are generally delimited by six equivalent $\{110\}$ lateral facets. Here, in figure II.1-(a), we can see the $\{1-10\}$ facets but we can also see $\{11-2\}$ facets that randomly appear on the sidewalls. This can be due to HCl_{add} which is known to have an important effect on the growth rate of the different facets. Moreover, additional HCl drastically reduces the supersaturation and then the nucleation density of NWs. $\gamma = 0.15$ for figure II.1-(a) and $\gamma = 20$ for figure II.1-(b). NWs grown without additional HCl clearly have a uniform diameter with a hexagonal shape delimited by six equivalent $\{110\}$ side facets and (111)B facet on the top. We also observe that the density of the NWs drastically increases and the morphology of the NWs is improved due to the lower HCl partial pressure. Then, for the rest of the study, additional HCl is not introduce in the reactor during growth to ensure InAs NWs nucleation.

II.2.2.2 Effect of the growth temperature

As presented in Chapter I, temperature has a large influence on the growth rate of (100) GaAs surface. As a matter of fact, varying temperature enables to assess the mechanisms involved during NW growth in the HVPE system, since the HVPE growth regime implemented by our laboratory is mainly governed by kinetics and thermodynamics. Figure II.2 displays the effect of the growth temperature on InAs NWs growth. The partial pressures of As_4 (P_{As_4}) and InCl (P_{InCl}) were fixed to 3.6×10^{-4} atm and 6.4×10^{-3} atm, respectively, giving a III/V ratio of 18. Regardless of the growth temperature, the NWs clearly exhibit a uniform diameter with a hexagonal shape. Similar findings on InAs morphology were observed in ref [26], where NWs were grown by a vapor-solid (VS) mechanism.

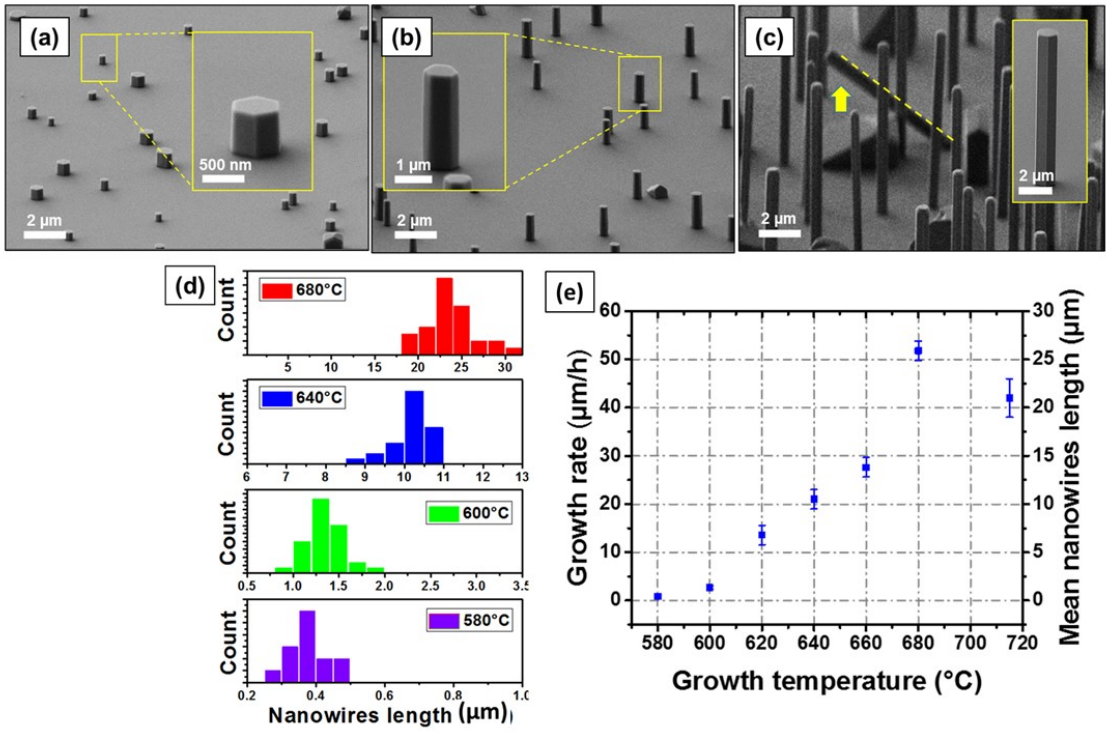

Figure II.2: Tilted-view SEM images of InAs NWs grown on Si(111) substrate at different growth temperatures: (a) 580 °C, (b) 600 °C and (c) 640 °C. Insets show magnified views of single NWs. (d) Length distributions of InAs NWs for different growth temperatures. (e) Average NW growth rate as a function of the growth temperature.

We consider that formation of liquid In particles which would initiate a VLS growth mode, is thermodynamically not favorable. It is difficult to form droplets of In from InCl gaseous precursors on the substrate surface. In fact, during my PhD, I have observed the formation of an oxide layer on the surface of the indium source due to a technical problem of the N_2 generator. We assumed that the presence of the oxide reduced the yield of the source, but we were not able to determine its value. However, by considering a yield of 99% which is still a very high yield, I have calculated the supersaturation corresponding to the formation of liquid indium from InCl molecules. The variation of ${\gamma_{In}}^{liq}$ as a function of the temperature is shown on figure II.3.

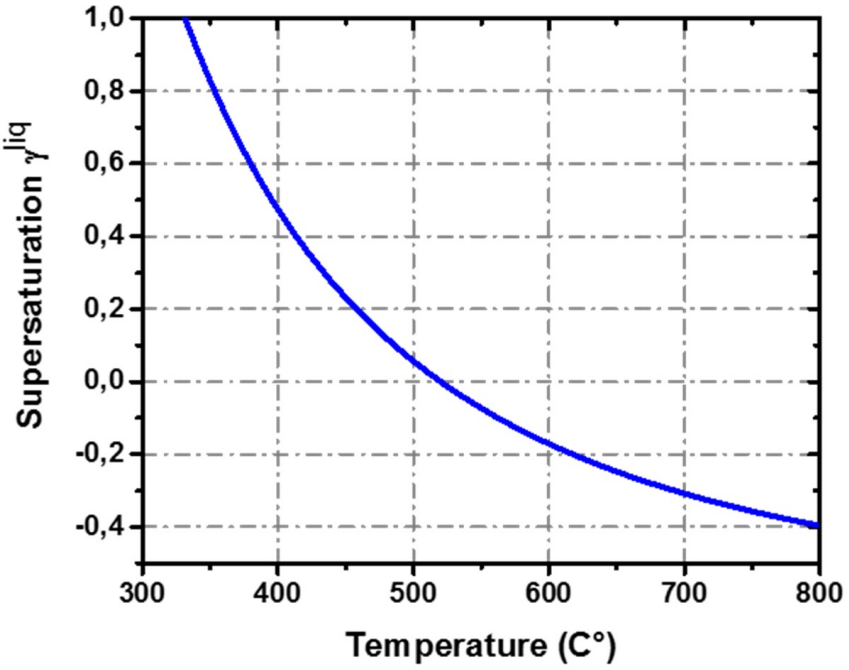

Figure II.3: Variation of the liquid indium supersaturation as a function of the growth temperature.

One can observe that the supersaturation becomes negative at a temperature of 520 °C. This means that for growth temperature above 520 °C, the formation of an indium droplet is not favourable. The supersaturation was calculated here with the partial pressures that are the most favourable for the formation of indium droplets (III/V=18 in this study). Here, we assume that growth is likely initiated with the formation of self-assembled InAs islands by the Volmer-Weber mode on the oxide-free surface. The different growth steps are represented in figure II.4. The one-dimensional form of NWs at growth temperatures above 600 °C is ensured by the growth conditions, which promote anisotropic growth where the axial growth rate is maintained higher than the lateral one. HVPE was proven to be a very powerful growth technique for shaping 3D structures by taking advantage of the large intrinsic anisotropic growth of III-V materials [82, 78].

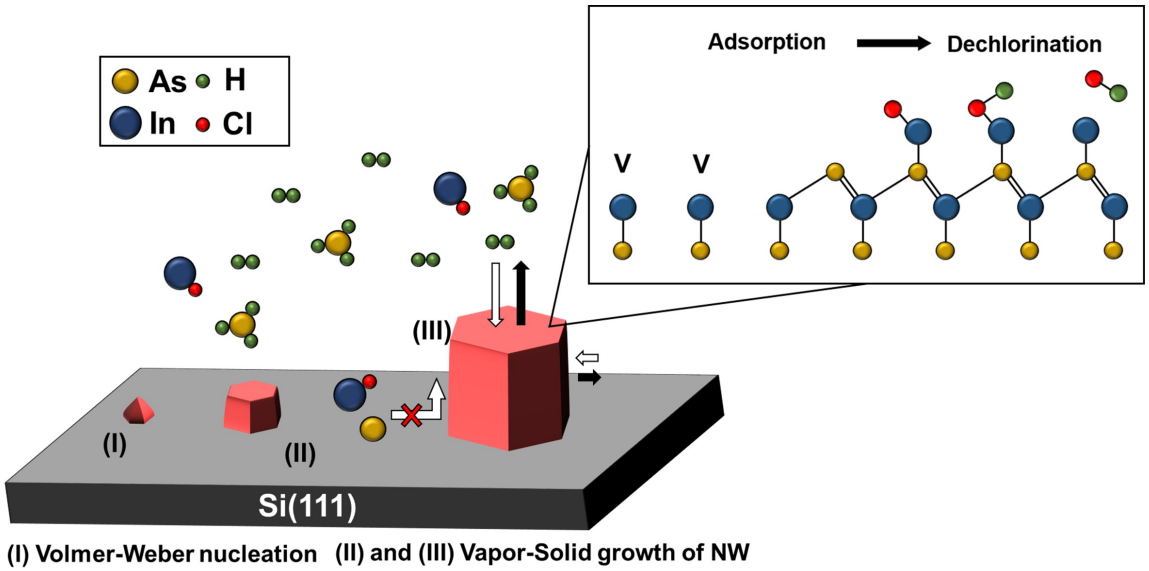

Figure II.4: Schematic of InAs nanowire growth. Step I - Volmer-Weber nucleation of a 3D island. Step II - As adsorption on vacant In (reaction (2), p.48), on which InCl molecules adsorb (reaction (3), p.48), and chlorine desorption into HCl by H_2 (reaction (4), p.48). Step III – Axial growth rate prevails. There is no diffusion of the precursors on the substrate surface, growth precursors do not incorporate on the NW sidewalls.

The nucleation stage determines the island size and NW diameter. Nucleation strongly depends on the silicon surface, with a random surface re-oxidation occurring after HF etching prior to the introduction of the substrate into the reactor. This likely explains the large dispersion in the NW diameter on the same sample. No dependence has been observed between length and diameter. The variation of the axial growth rate of InAs NWs as a function of the growth temperature is presented in Figure II.2-(e). The growth rate was determined from statistical analysis as shown in Figure II.2-(d) and calculated by dividing the average length of the NWs by the growth time. It can be observed that the axial growth rate increased from 0.8 µm/h to 51.8 µm/h with increasing growth temperature from 580 °C to 680 °C. The axial growth rate decreased to 42 µm/h at a higher temperature of 715 °C. Similar dependence of the axial growth rate of InAs NWs with the growth temperature was observed by MBE and MOVPE [83, 84] where growth was governed by the thermally-activated adatom diffusion on the surface of the substrate and NW sidewalls [45, 84]. HVPE growth is mainly driven by the balance between adsorption and desorption of precursor materials, and the kinetics of the dechlorination step. Surface diffusion of ad-species is not limiting in the HVPE process [79, 82, 85]. A first simple analysis indicates that at low temperature, growth is limited by decomposition of adsorbed precursors, e.g., dechlorination. As the temperature increases, the growth rate increases due to thermal activation of the dechlorination step until desorption prevails for the highest temperature, resulting in a maximum growth rate with temperature (Figure II.2-(e)).

II.2.2.3 Effect of the III/V ratio

I have also studied the effect of the III/V ratio on the axial growth rate. The growth temperature was fixed at 680 °C where the growth rate was the greatest. The evolution of the average axial growth rate of NWs as a function of the partial pressures of both III and V elements is reported in Figure II.5-(a). Either the InCl partial pressure was fixed at 6.4×10^{-3} atm and As_4 partial pressure was varied from 3.6×10^{-4} to 1.0×10^{-3} atm (blue curve), or As_4 was fixed at 3.6×10^{-4} atm and InCl partial pressure was varied from 1.0×10^{-3} to 6.4×10^{-3} atm (red curve). This resulted in a III/V variation from 3 to 18. An increase of the InCl partial pressure induced an increase of the axial growth rate from 36.8 µm/h to 52 µm/h. The growth rate saturated at higher III/V (as seen from the red curve in Figure II.5-(a)). To explain this observation, we introduce thermodynamic and kinetic considerations as described earlier. At the growth temperature of 680 °C, the growth rate is assumed to be mainly dependent on the supersaturation since the growth temperature is high enough to ensure a fast dechlorination of InCl ad-species with respect to the incoming flux of material on the surface. As shown in Figure II.5-(b), the supersaturation in the vapor phase, which promotes InAs deposition, increases with the input partial pressure of InCl. Consequently, the growth rate increases. When the III/V ratio is greater than 12, one observes a slight decrease of the growth rate, as the surface becomes blocked with a large amount of adsorbed InCl ad-species. The growth rate is then limited by the kinetics of dechlorination and remains nearly constant. This trend has already been studied theoretically and experimentally for the growth of GaAs by HVPE where the authors illustrated the surface blocking with the III-element as a function of the growth temperature and the partial pressure of GaCl precursor [86].

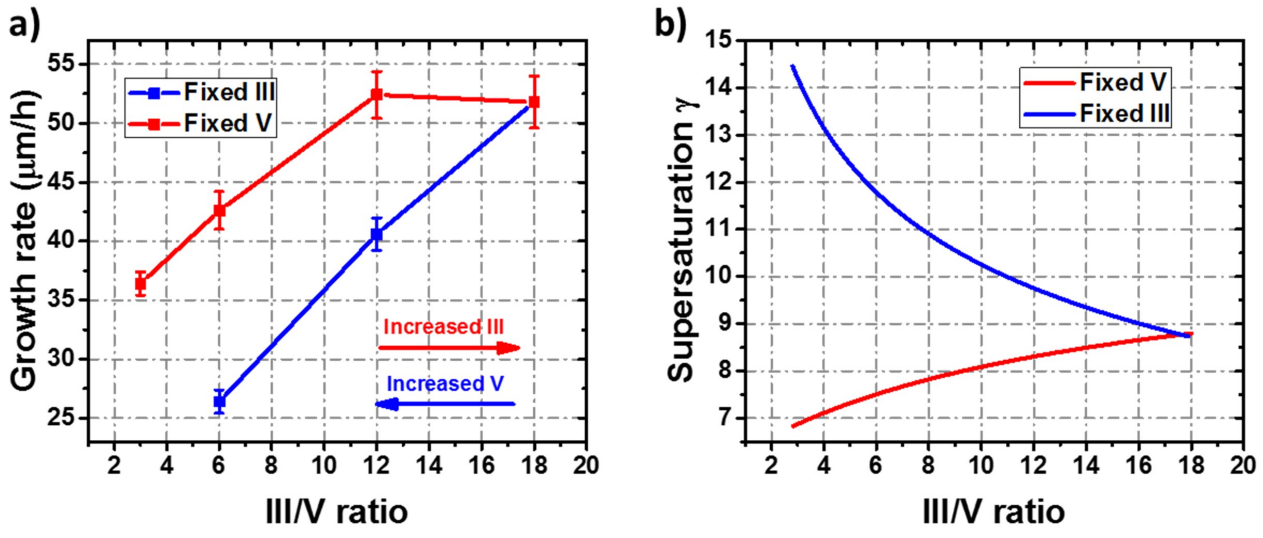

Figure II.5: (a) Variation of the growth rate as a function of the III/V ratio in the vapor phase. (b) Variation of the supersaturation as a function of the III/V ratio.

The blue curve in Figure II.5-(a) shows the variation of the axial growth rate as a function of the III/V ratio, by varying the partial pressure of As_4 at a fixed partial pressure of InCl. The growth rate increases from 26 µm/h to 52 µm/h when the III/V ratio increases from 6 to 18. Ref. [87]

showed that the (111)B surface structure of III-As is sensitive to the growth temperature and the As flux in the vapor phase (AsH_3, As_4, As_2), leading to different surface reconstructions such as (1×1), (2×2) and $(\sqrt{19} \times \sqrt{19})$. Several studies claim that the (2×2) surface reconstruction originates from the formation of an As-trimer layer with very stable bonds under an As rich environment, which is obviously the case with the high material input of HVPE. As a result, free dangling bonds for the incorporation of the III-element are missing and therefore the growth rate is reduced. [88] On this basis, we assume that such a decrease in the growth rate with As_4 is related to the (2×2) surface reconstruction which corresponds to surface saturation with the As-trimer bonds.

II.2.3 Structural characterizations

Structural characterization by HR-(S)TEM was carried out to examine the crystalline quality of the NWs. Figure II.6-(a), (b) and (c) show HAADF-STEM images of an InAs NW grown at 680 °C with a III/V ratio of 3.

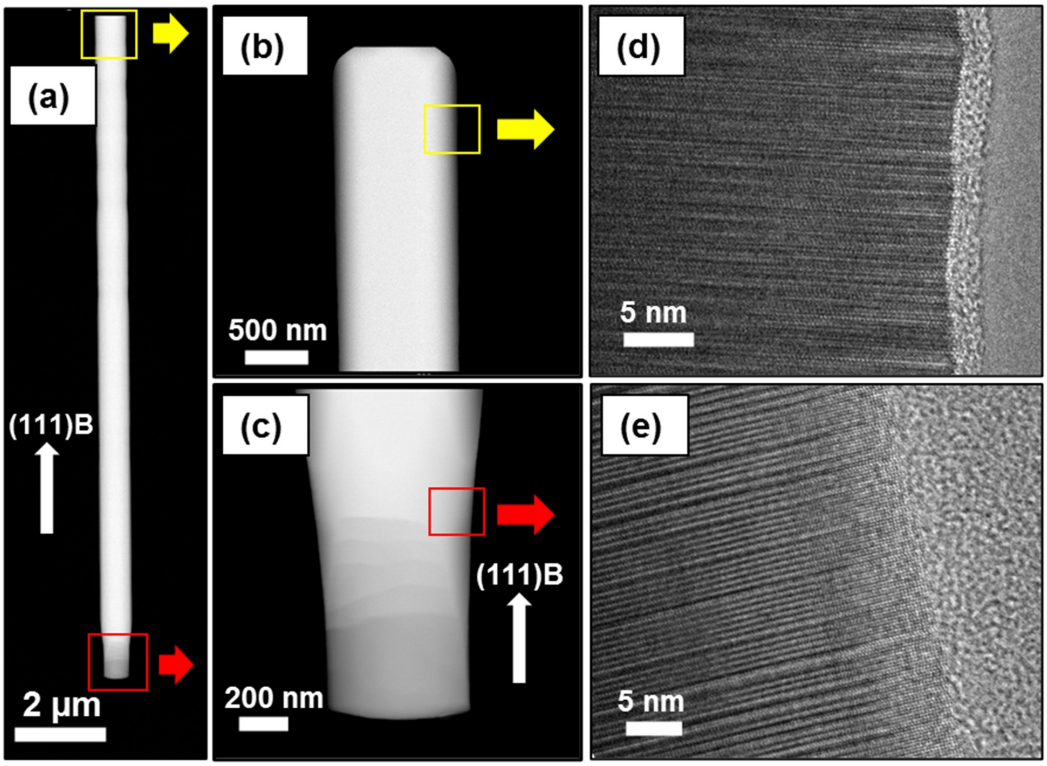

Figure II.6: (a) HAADF of InAs NW, (b) NW top and (c) NW base. (d) and (e) Corresponding HRTEM images of (b) and (c), respectively.

The uniform diameter and the well faceted top of the NW indicate that the growth occurs through a direct condensation from the vapor phase. The reverse tapered base of the NWs is attributed to the transient regime during which the partial pressures of the gaseous precursors stabilize. HRTEM images taken from the top (Figure II.6 -(d)) and the base (Figure II.6-(e)) of the NW indicate that the NWs exhibit alternating zinc-blende (ZB) and wurtzite (WZ) segments. These observations have been

confirmed on dozens of wires grown at different growth conditions of temperature and III/V ratio. Z. Liu et al. [87] have reported that the crystal phase of InAs is determined by the growth temperature and the As_4 composition in the vapor phase. The authors assumed that the formation of structural defects during InAs growth is linked to the (2×2) surface reconstruction of the (111)B top facet of the NW. This was supported by a theoretical model based on the nucleation probability of both wurtzite and cubic phases. Based on that model, the presence of both phases in HVPE-grown InAs NWs over the broad range of growth conditions used in our work can be related to the high partial pressure of As_4 used in the HVPE process (some $10^{-4}/10^{-3}$ atm) compared to other growth techniques.

II.2.4 Kinetic modeling

To model the axial growth rate of the NWs, we consider that there is a direct condensation from the vapor phase onto the (111)B top surface of the InAs NWs. The growth of InAs NWs proceeds through the following reactions, depicted in Figure II.4, for axial growth perpendicular to the (111)B face:

$$2As_{2g} \rightleftharpoons As_{4g} \qquad (1)$$

$$4V + As_{4g} \rightleftharpoons 4As \qquad (2)$$

$$As + InCl_g \rightleftharpoons AsInCl \qquad (3)$$

$$AsInCl + H_{2g} \rightleftharpoons AsIn_c + HCl_g + \frac{1}{2}H_{2g} \qquad (4)$$

where V is an In vacant site on the substrate surface; index g is assigned to gaseous molecules; index-free species are adsorbed molecules or atoms; and index c is for crystalline species. InAs deposition can be summarized by the global reaction:

$$InCl_g + \frac{1}{4}As_4 + \frac{1}{2}H_2 \rightleftharpoons InAs_s + HCl_g$$

γ_{InAs} is plotted as a function of the growth temperature in Figure II.7-(a) (p.51, blue curve). It remains positive over the temperature range: the vapor is supersaturated with respect to equilibrium, and growth occurs. The supersaturation parameter decreases with increasing temperature, meaning that the growth rate would continuously decrease, which is not observed. We should consider the kinetics of dechlorination, which is thermally activated. Thus, it is important to determine the dechlorination frequency (kinetics of reaction (4)), which is responsible for the low growth rate that is observed at low temperature, despite favorable thermodynamic conditions.

It is shown that for reversible processes where the complex species (AsInCl) acts as source for the crystal unit (InAs), the growth rate of InAs can be reduced to the growth rate expression for direct condensation in a one-particle system, when the desorption frequency of AsInCl molecules (that occurs here through the desorption of InCl according to reverse reaction (3)), is much higher

than the dechlorination frequency (reaction (4)). As a matter of fact, in (As, InCl) systems, the adsorption/desorption flux ratio for As is greater than one for temperature up to 800 °C, but it is not the case for the volatile InCl molecules. Desorption of InCl starts to be an issue for temperature around 600 °C, that is why III/V ratio greater than one are used in HVPE to compensate the strong desorption of element III precursors. The physics of desorption prevails over reaction (4), so that the surface density of AsInCl is uniform all over the surface, and diffusion fluxes vanish.

The classical expression for direct condensation rate R_{DC} in one-particle systems is:

$$R_{DC} = \Omega_{InAs}\gamma_{InAs}\nu_{-4}c_{InAs}$$

where Ω_{InAs} is the molecular volume of InAs, ν_{-4} is the chlorination frequency of InAs according to reverse reaction (4), c_{InAs} is the surface concentration of InAs. c_{InAs} depends on the detailed description of the intermediate steps (reactions (1) to (3)) involved in the growth of the InAs crystal unit (reaction (4)), as described in the following. Introducing the chlorination flux (reverse reaction (4)) J_{-4}:

$$\nu_{-4}c_{InAs} = J_{-4}$$

$$R_{DC} = \Omega_{InAs}\gamma_{InAs}J_{-4}$$

The net adsorption fluxes of ad-species i per unit time and surface $J_i = J_{+i} - J_{-i}$, where J_{+i} is the adsorption flux and J_{-i} the desorption flux of species i, are written for chemical reactions (2), (3) and (4) as:

$$J_{As} = J_2 = J_{+2} - J_{-2} = 4k_{+2}\theta_v[As4_{(g)}] - k_{-2}\frac{\theta_{As}^4}{\theta_v} \tag{II.1}$$

$$J_{AsInCl} = J_3 = J_{+3} - J_{-3} = k_{+3}\theta_{As}[InCl_{(g)}] - k_{-3}\theta_{AsInCl} \tag{II.2}$$

$$J_{InAs} = J_4 = J_{+4} - J_{-4} = k_{+4}\theta_{AsInCl}[H_{2_{(g)}}]^{1/2} - k_{-4}\theta_{InAs}[HCl_g] \tag{II.3}$$

where $k_{\pm i}$ are temperature-dependent pre-factors involving activation energies ε_i, $[i_{(g)}]$ is the partial pressure of gaseous species i and θ_i is the surface coverage of ad-species i. The calculation of the pre-factors $k_{\pm i}$ is thoroughly described in reference [82]. Namely, k_{+i} are the kinetic constants corresponding to the adsorption of As (reaction (2)), InCl (reaction (3)) and H_2 onto AsInCl ad-species that leads to dechlorination (reaction (4)). k_+i are written with the Ernst-Knudsen flux expression. k_{-i} are the kinetic constants corresponding to the reverse desorption processes of reactions (2), (3) and (4); they are written as products of the partition functions of the species involved.

The surface coverage of vacant surface sites is defined as:

$$\theta_v = 1 - \theta_{As} - \theta_{AsInCl} - \theta_{InAs} \tag{II.4}$$

or

$$\frac{1}{\theta_v} = 1 + \frac{\theta_{As}}{\theta_v} + \frac{\theta_{AsInCl}}{\theta_v} + \frac{\theta_{InAs}}{\theta_v} \tag{II.5}$$

with

$$\frac{\theta_{As}}{\theta_v} = \sqrt{2}\left(\frac{k_{+2}^{1/4}}{k_{-2}^{1/4}}\right)[As4_{(g)}]^{1/4} = A(T,\varepsilon_2)[As4_{(g)}]^{1/4} \tag{II.6}$$

$$\frac{\theta_{AsInCl}}{\theta_v} = \left(\frac{k_{+3}}{k_{-3}}\right)[InCl_{(g)}] \times A(T,\varepsilon_2)[As4_{(g)}]^{1/4} = B(T,\varepsilon_2,\varepsilon_3)[InCl_{(g)}][As4_{(g)}]^{1/4} \tag{II.7}$$

$$\frac{\theta_{InAs}}{\theta_v} = \left(\frac{k_{+4}}{k_{-4}}\right)[H2_{(g)}]^{1/2}/[HCl_{(g)}] \times B(T,\varepsilon_2,\varepsilon_3)[InCl_{(g)}][As4_{(g)}]^{1/4} \tag{II.8}$$

$$\frac{\theta_{InAs}}{\theta_v} = C(T,\varepsilon_2,\varepsilon_3,\varepsilon_4)[InCl_{(g)}][As4_{(g)}]^{1/4}[H2_{(g)}]^{1/2}/[HCl_{(g)}] \tag{II.9}$$

The activation energies ε_i are determined after fitting the experimental data. The system composed of equation II.6, II.7 and II.8 is solved using the Jacobi iterative method. It enables the calculation of θ_{As}, θ_{AsInCl}, θ_{InAs}, and then θ_v. θ_v is plotted and the growth rate R_{DC} can be finally plotted as a function of θ_v:

$$R_{DC} = \kappa \times \gamma_{InAs} \times \theta_v \tag{II.10}$$

with $\kappa = \Omega_{InAs} k_{-4} C(T,\varepsilon_2,\varepsilon_3,\varepsilon_4)[InCl_{(g)}][As4_{(g)}]^{1/4}[H2_{(g)}]^{1/2}$

The red curve in Figure II.7-(a) shows the variation of the surface coverage of vacant sites (V) as a function of the growth temperature. Figure II.7-(b) shows the variation of the growth rate as a function of the temperature. At low temperature, growth is limited by dechlorination of InCl ad-molecules and desorption of species. The surface is then blocked with undecomposed AsInCl species. This explains the low surface coverage of vacant sites and the low growth rate even at high supersaturation. When the temperature increases, the dechlorination frequency increases. Consequently, θ_V starts to increase and the axial growth rate significantly increases with the temperature up to a maximum of 680 °C (as seen in Figure II.7-(b)). At high temperature of 715 °C, desorption of InCl becomes predominant and the growth rate decreases. Finally, we obtain the typical bell-curve which is generally observed in HVPE.

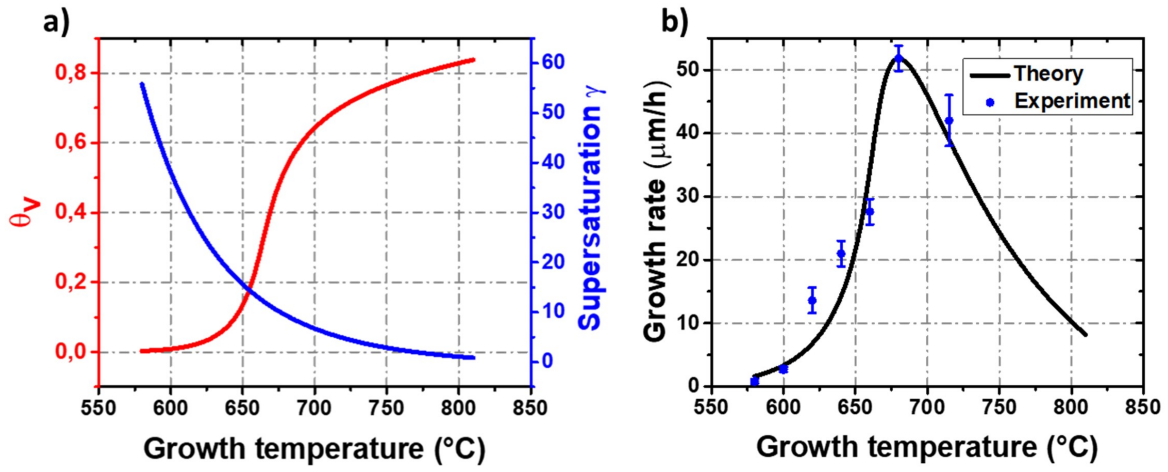

Figure II.7: (a) Variations of the coverage of vacant surface sites and of the supersaturation as a function of the growth temperature. (b) Variation of the axial growth rate as a function of the growth temperature at a III/V ratio of 18.

II.3 Selective area growth of InAs nanowires

Controlling the length and diameter of NWs is essential to have homogenous optical and electrical properties across the substrate. Selective area growth (SAG), which uses a patterned dielectric mask, is a powerful solution to control the nanostructures morphology. The SAG of InAs NWs has already been demonstrated by MBE and MOVPE on various substrates, such as patterned InAs(111)B [25], GaAs(111)B [28] and Si(111) [26, 29]. The control of the morphology is achieved by tuning different growth parameters (growth temperature, growth time and III/V ratio). HVPE is well known for the selective growth of micro- and nano-structures for both III-nitride and III-arsenide materials [78, 89, 90, 91, 92]. Due to the use of chloride III-elements, HVPE enables a perfect selectivity at a low temperature of about 600 °C on usual masks like SiOx or SiNx. In ref. [78, 89], it is shown that the morphology of the microstructures can be easily tuned by changing the surface kinetics of the different facets. Here we show that the control of SAG InAs NWs is achievable by a tight control of the growth parameters such as temperature and III/V ratio.

This work is part of a collaboration with Professor Ray LaPierre from McMaster University (Canada). The aim of the project is to develop multi-spectral photo-detectors using InAs NWs arrays. With this type of device, it is possible to vary the absorption wavelength by tuning the length and diameter of the NWs. The control of the NWs morphology requires a good understanding of the growth parameters effect on the NWs growth. Therefore, this study was performed through two steps. First, I have calibrated the growth on patterned GaAs(111)B substrates as condensation readily occurs on GaAs. Then, growth was performed on Si to demonstrate the feasibility of InAs-based devices on Si. The SiOx mask was deposited on GaAs(111)B by plasma-enhanced chemical vapor deposition (PECVD) and the pattern was defined by electron beam lithography (EBL) with hole diameters of 60 nm. For Si(111), larger diameters were used, 350 nm, 500 nm and 1 μm, to favor nucleation. The

SiNx mask was deposited on Si(111) by plasma-enhanced chemical vapor deposition (PECVD) and then patterned by optical lithography. Before growth, Si(111) substrates were etched with 5% HF for 10 s to remove the native oxide formed in the openings.

II.3.1 Growth on GaAs(111)B substrate

The GaAs(111)B patterned substrates were supplied by IBM Europe within the framework of a collaboration with Institut Pascal. The patterns consist of a 4×4 μm^2 nano-holes arrays with diameter varied from 60 nm to 1000 nm and pitch between 200 nm and 4 µm. The large panel in dimensions allowed us to determine the ideal pattern enabling the growth of InAs NWs.

Figure II.8 shows SEM images of InAs micro- and nano-structures grown on GaAs(111)B substrates with SiOx mask at different opening diameters (D) of a) D = 200 nm, b) D =100 nm and c) D = 60 nm. 2D growth is observed for diameters above 100 nm (figure 8-(a)), while NWs are obtained for diameters below 100 nm (figure 8-(c)). Radial growth was favoured for large apertures, whereas axial growth was favoured for small apertures. The presence of both 2D growth and NWs in figure 8-(b) may be explained by residual SiOx in the openings resulting in a reduced hole diameter. This small effective oxide free surface is favorable for NW growth.

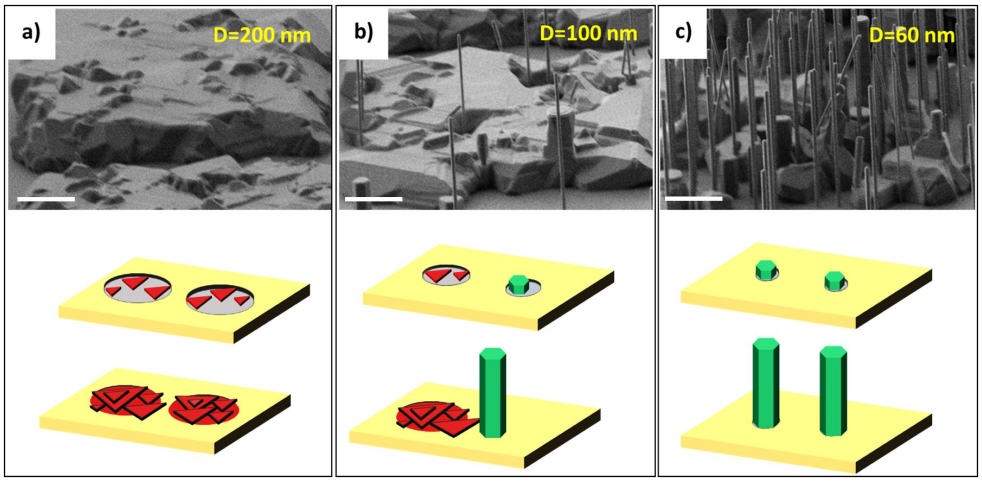

Figure II.8: Tilted-view SEM images of InAs material grown on patterned GaAs(111)B with SiOx mask. The corresponding schematic of the nucleation step is shown below each SEM image. The diameters of the holes were (a) 200 nm, (b) 100 nm, and (c) 60 nm. Different nuclei merge into coalesced triangular-shaped islands (red) or NWs (green). The pitch is 2 µm and scale bars are 5 µm.

The nucleation density during SAG depends not only on the growth temperature and vapor phase composition but also on the aperture size [9, 27]. For large apertures, more atoms are collected enabling the nucleation of many triangular-islands. The coalescence of islands during growth leads to the formation of lateral facets with a very high growth rate (see scheme in Figure II.8-(a)). Then due to the lateral overgrowth, crystals from different apertures coalesced forming a layer with visible triangular 3D islands. In HVPE, it is well known that there is no parasitic nucleation on the dielectric

mask due to the use of III-chloride precursors and the high growth temperature. For small apertures (<100 nm), only one island nucleates promoting the growth of a NW with low radial growth rate (see scheme in Figure II.8-(c)).

With the aim to develop multi-spectral photo-detectors with McMaster University, we have decided to study the effect of the growth conditions on the NWs morphology. Multi-spectral photo-detector requires a precise control of the NWs length, diameter and density. The theory behind multi-spectral photo-detectors will be further detailed in the optical characterization part. By tuning the growth temperature we expect to tune the NWs length and the diameter. The size of the array is increased to 1×1 mm^2 to evaluate the absorptance of the NWs arrays. The hole diameter is 60 nm and the picth is 4 µm. The effect of the growth temperature on InAs NWs growth is shown on figure II.9. The NWs are grown for 30 minutes. The temperature is varied between 580 °C and 715 °C. InCl and As_4 partial pressures were fixed at 4.5×10^{-3} atm and 3.6×10^{-4} atm respectively.

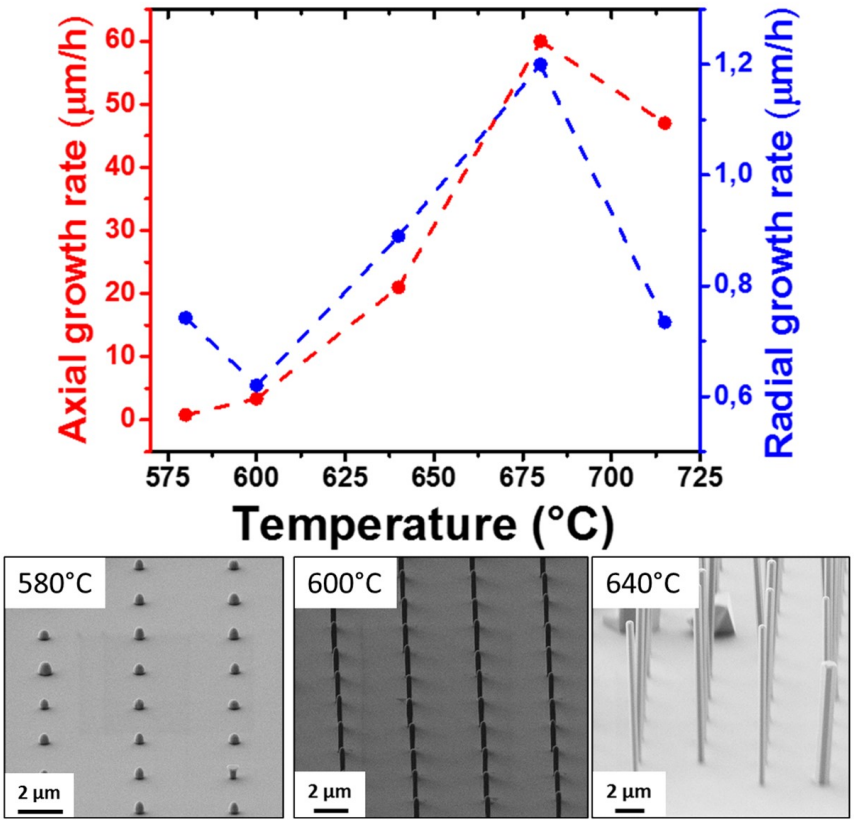

Figure II.9: a) Average axial and radial growth rates of InAs NWs grown on patterned GaAs(111)B as a function of the growth temperature. (b), (c) and (d) show tilted-view SEM images of InAs grown at 500 °C, 600 °C and 640 °C, respectively. The hole diameter is 60 nm and the picth is 4 µm.

We can observe that the axial growth rate follows the same trend as the axial growth rate of InAs NWs grown on bare Si(111) substrates. Between 580 °C and 680 °C the growth rate increases due to an increase of ad-molecules decomposition, especially the dechlorination of InCl molecules. By further increasing the temperature, the adsorption/desorption ratio of molecules drastically decreases, leading to the drop of the axial growth rate. The same behaviour is observed for the radial growth

rate which indicates that similar kinetic mechanisms are involved during growth. As shown in the section II.2.2.3, the As_4 partial pressure has a high impact on the InAs NWs length, meaning that this parameter can be varied to tune the NW morphology. Due to the limited number of good patterned substrates, I have not carried out a systematic study of the As_4 partial pressure effect. However, figure II.10 shows InAs NWs grown at 640 °C at two different III/V ratios. InCl partial pressure is fixed at 4.5×10^{-3} atm and the III/V ratios are 6 and 12 for figure (a) and (b), respectively. NWs diameters and lengths are D=680 nm / L=2 µm for (a) and D=500 / L=10 µm for (b), resulting in aspect ratios of 3 and 20 respectively.

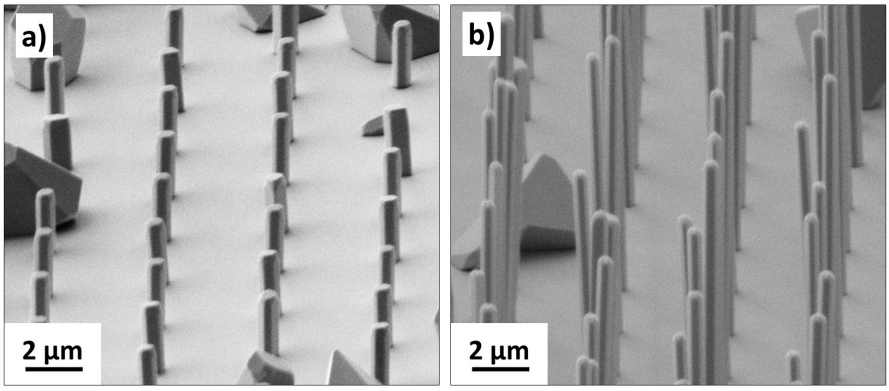

Figure II.10: Tilted-view SEM images of InAs NWs grown on GaAs(111)B substrate at III/V ratio of (a) 12 and (b) 6. The hole diameter is 60 nm and the picth is 4 µm.

The very low axial growth rate observed in figure (a) compared to figure (b) is consistent with the results of II.2.2.3 for InAs NWs grown at 680 °C under various As_4 partial pressures. It confirms that the axial growth rate is limited by the formation of As-trimers on the (2×2) reconstructed surface. The formation of such complexes is even more important at 640 °C because the adsorption of arsenic molecules is increased at lower temperature. The larger diameter is simply explained by the larger adsorption of arsenic molecules on the lateral facets. This latter, is known to be the main mechanism governing the radial growth rate as shown in Ref. [49]. The tuning of the NWs length and diameter by varying the growth parameters is very promising for multi-spectral photo-detectors. By precisely choosing the growth temperature, III/V ratio and growth time, it would be possible to grow InAs NWs with well defined diameter and length. Finally, those samples are the one used for FTIR measurement and the results are presented in the optical characterization part. The selective growth of InAs NWs on GaAs(111)B was an important step for HVPE, yet, the final goal is to grow NWs arrays on Si(111) substrates, aimed at integrating III-V based devices on silicon plateform.

II.3.2 Growth on patterned Si(111) substrate

Selective growth on GaAs substrate under various growth conditions has been successfully demonstrated in the previous part and growth on non-patterned Si(111) has been shown in section II.2. I present here the study of InAs NWs growth on patterned Si(111) substrate. The willingness

to grow InAs NWs on silicon raises from the fact that Si substrates are cheaper than GaAs substrates and are easier to process.

Figures II.11-(a), (b) and (c) show SEM images of InAs NWs grown on SiNx patterned Si(111) substrate with opening diameter of D = 1 µm (a), D = 500 nm (b) and D = 350 nm (c). For D = 1 µm many triangular islands nucleate in each hole resulting in a layer with visible triangle after coalescence. For D = 500 nm, either 3D crystals or NWs nucleated. However, for 350 nm openings, NW growth was promoted and only one NW nucleated per hole. This behaviour is similar to that observed on GaAs(111)B. However, the transition between 3D growth and NW growth on Si(111) was not clearly defined and NWs grew even on very large apertures.

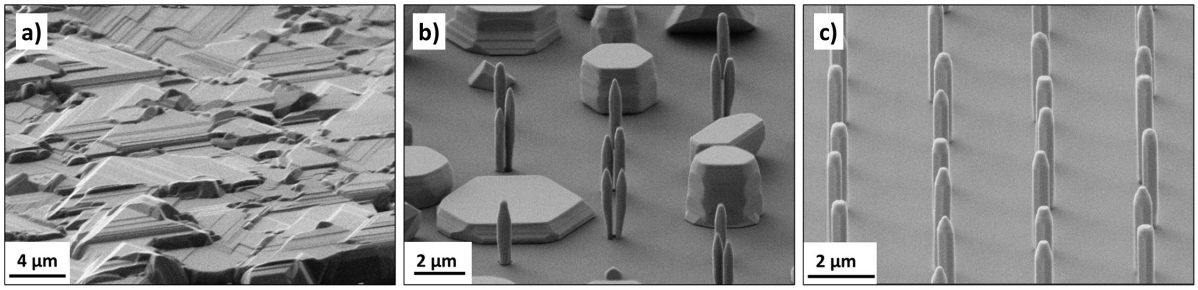

Figure II.11: Tilted-view SEM images of InAs material grown on patterned Si(111) with SiNx mask. The diameter of the hole is (a) 1 µm, (b) 500 nm and c) 350 nm. The pitch is 2.5 µm.

For growth on Si(111), we consider that for figure II.11-(a) and for holes with 3D crystals in figure II.11-(b), the same growth as Figure II.10-(a) occurs, which corresponds to the coalescence of triangular 2D islands. For holes with NWs, we speculate that the reoxidation of the surface creates pinholes inside the apertures which form nucleation sites for NWs but inhibit the formation of large crystals. This oxidation occurs during the introduction of the sample in the reactor after the HF cleaning. Due to this reoxidation, there is a reduction of the atoms' collection area. Thus, for D = 350 nm, the oxide-free surface enables the nucleation of only one NW. Moreover, once a NW nucleates in the apertures, it acts as a sink and collects a large amount of the arriving atoms. Subsequently, the probability for additional NWs to nucleate in each hole is drastically reduced [27]. This study highlights the lower nucleation density on Si(111) as compared to GaAs(111)B. A maximum diameter of 60 nm was required to nucleate only one NW on GaAs(111)B, while holes with a diameter of 350 nm on Si(111) still resulted in only a single NW. This is explained by the As-terminated surface of the GaAs(111)B substrate, which promotes the nucleation of InAs material.

Figure II.12-(a) shows the variation of the axial and radial growth rates of InAs NWs grown on patterned Si(111) substrate with the growth temperature. The diameter of 350 nm was fixed to ensure the nucleation of only one NW in the apertures. The growth temperature ranged from 600 °C to 680 °C and the III/V ratio was fixed at 2.

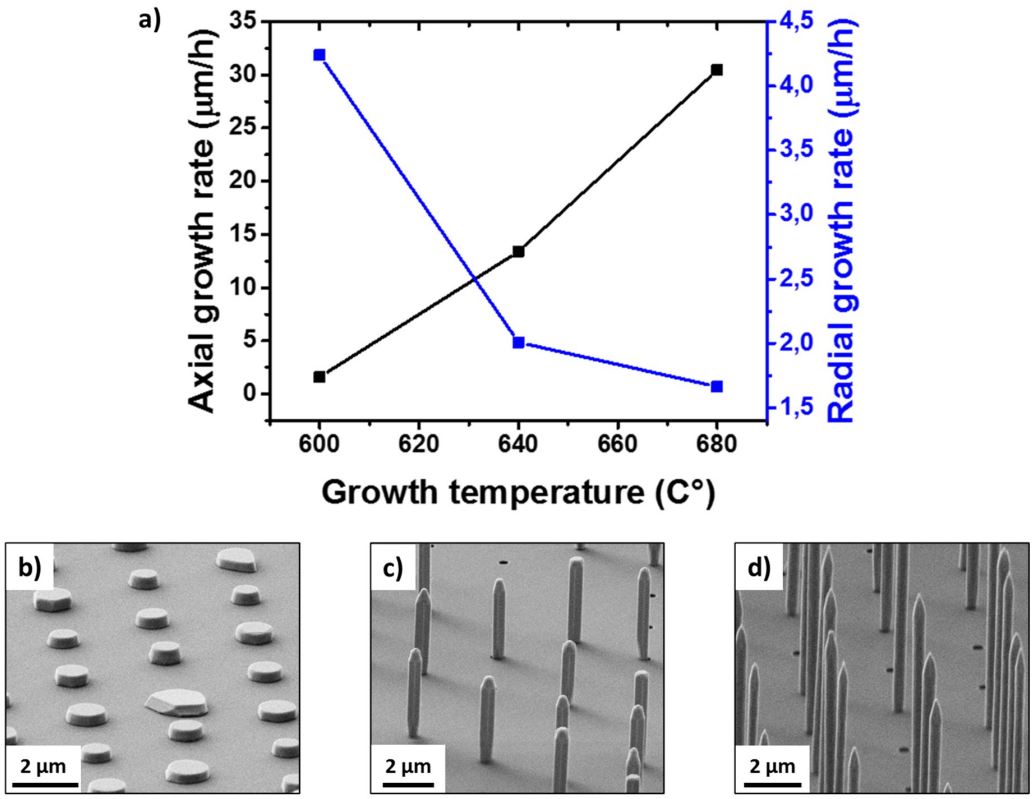

Figure II.12: (a) NWs axial and radial growth rates as a function of the growth temperature. Tilted-view SEM images of InAs NWs grown on Si(111) substrate at different growth temperatures: (b) 600 °C, (c) 640 °C and (d) 680 °C. Hole diameter is 350 nm and the pitch is 2.5 µm.

The axial growth rate increased from 1 µm/h to 32 µm/h with increasing growth temperature from 600 °C to 680 °C. At low temperature, the growth is limited by the decomposition of adsorbed precursors, e.g., dechlorination of the InCl species. As the temperature increases, the growth rate increases due to thermal activation of the dechlorination step. The results presented here are consistent with the model developed in Section 1 for the growth of InAs NWs on bare Si(111). It confirmed that NWs grow following the vapor-solid mechanism (VS). The radial growth rate decreased with the temperature. In HVPE, it is assumed that the {1-10} facets have a low growth rate due to their atomic arrangement. It has been demonstrated in the case of GaAs growth that growth on {1-10} facets is mainly limited by the kinetics of adsorption and desorption of Ga and As species [78]. The same assumption can be applied to InAs growth because the growth steps are assumed to be identical with similar kinetic behavior. Thus, at low temperature, more As and In atoms are adsorbed on the surface corresponding to a high growth rate. As we increase the temperature, the desorption increases leading to a drop of the radial growth rate. Finally, an experiment at 715 °C was also carried out where no nucleation was observed. At such growth temperature, the desorption rate is too high to enable dense nucleation of InAs material on Si(111).

Figure II.13 shows the variation of the axial and radial growth rates of NWs grown on Si(111) at 640 °C for different III/V ratios. The As_4 partial pressure is fixed at 1.0×10^{-3} atm. The hole diameter

is 350 nm. By increasing the III/V ratio from 2 to 6.5 we observe a slight decrease of the axial growth rate while the radial growth rate stays nearly constant. At higher III/V ratio, the axial growth rate decreased to 2 µm/h and the radial growth rate increased significantly.

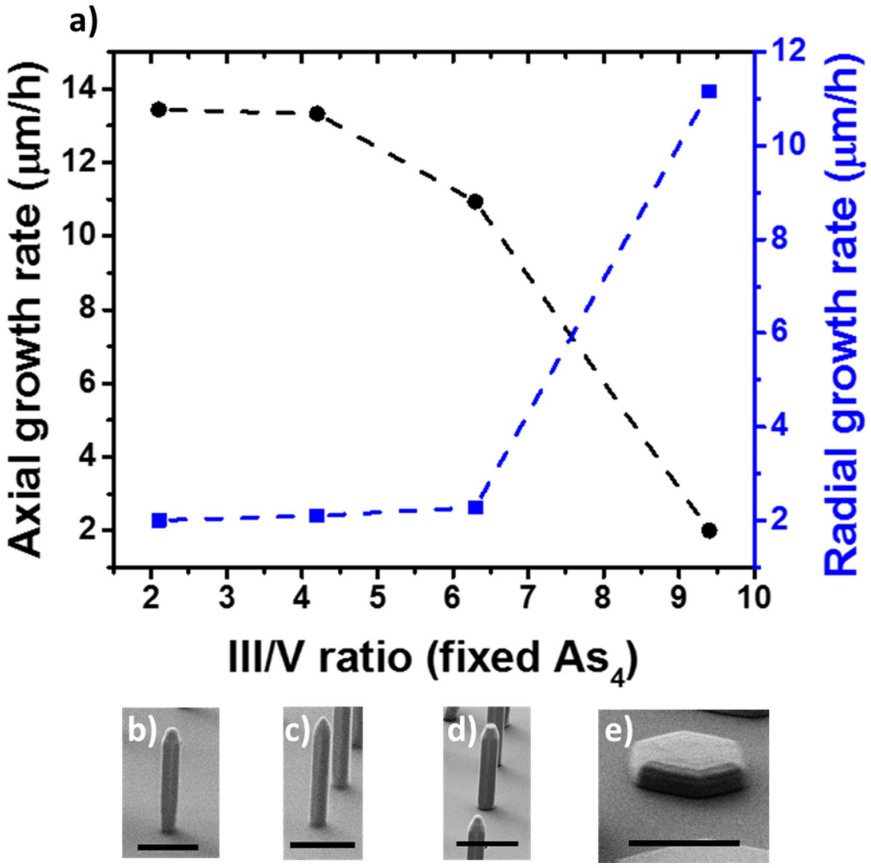

Figure II.13: (a) NWs radial and axial growth rates as a function of the III/V ratio. Tilted-view SEM images of InAs NWs grown on Si(111) at III/V ratio: (b) 2, (c) 4.5, (d) 6.5 and (e) 9.5. Scale bars are 2 µm. The diameter of the hole is 350 nm and the pitch is 2.5 µm.

The growth of the top (111)B facet is mainly limited by the dechlorination of the adsorbed InCl and the supersaturation of the vapor phase, that is by the gaseous material input with respect to equilibrium of the deposition reaction. As we have shown in section II.2, the axial growth rate increased when increasing the InCl partial pressure. However, for too high InCl partial pressure, e.g. too high supersaturation, the surface starts to be blocked by AsInCl molecules and the growth rate reaches a plateau. Here, at a III/V ratio of 2, the axial growth rate is already at its maximum value. As we increase the InCl partial pressure, the axial growth rate starts to decrease. Further increase of the InCl partial pressure (III/V = 9.5) leads to a drastic change of the InAs crystal morphology. At high III/V ratio, the (111)B facet becomes saturated by the AsInCl molecules, which inhibits the axial growth rate. On the other hand, the radial growth rate strongly increased with the III/V ratio. An increase of the InCl adsorption on the {1-10} facets does not explain such a variation of the morphology. It is well known that the growth rate of the {1-10} facets is mainly dependent on the adsorption of As atoms. Bjork et al. [26] demonstrated that the number of nuclei inside an aperture is

a function of the flux of In atoms. A minimum In flux was needed to have nucleation of a single NW in the aperture. By further increasing the In flux, they observed multiple NW nucleation. In our case, we assume that by increasing the InCl partial pressure, we enhance the nucleation density leading to many nuclei in the hole. Thus, as explained previously, the coalescence of the different islands forms new facets with a high growth rate.

II.3.3 Control of surface treatment step prior to growth

Due to the non-polarity of Si(111) surface, a pre-treatment is needed to control the growth direction of the NWs. It has been demonstrated by Tomioka et al. [47] that it is possible to change the non-polar Si(111) surface to an As-incorporated (1×1) surface by exposing the (111) surface to arsenic atoms. This procedure is now widely used in MBE and MOVPE and seems to lead to better NW nucleation on the substrate. In HVPE, direct condensation of InAs material on Si(111) is not a straightforward process due to low adsorption of chloride precursors in the range of temperature used in this work. On the other hand, the As-terminated (111)B surface of the GaAs(111)B substrate ensures the nucleation and then NWs grow perfectly along the (111)B direction, as shown in section II.3.1.

In the present study of InAs growth on Si(111), different surface pre-treatments have been tested in order to optimize the nucleation of NWs. First, substrates were exposed to an InCl partial pressure of 6.6×10^{-3} atm for 5 minutes, resulting in the growth of tilted NWs (figure II.14-(a)). For the second pre-treatment, the substrates were exposed to an As_4 partial pressure of 5×10^{-5} atm during the heating phase (figure II.14-(b)). We can see that the majority of NWs grown vertically. The growth temperature is 640 °C and the III/V ratio is 18 for both experiments.

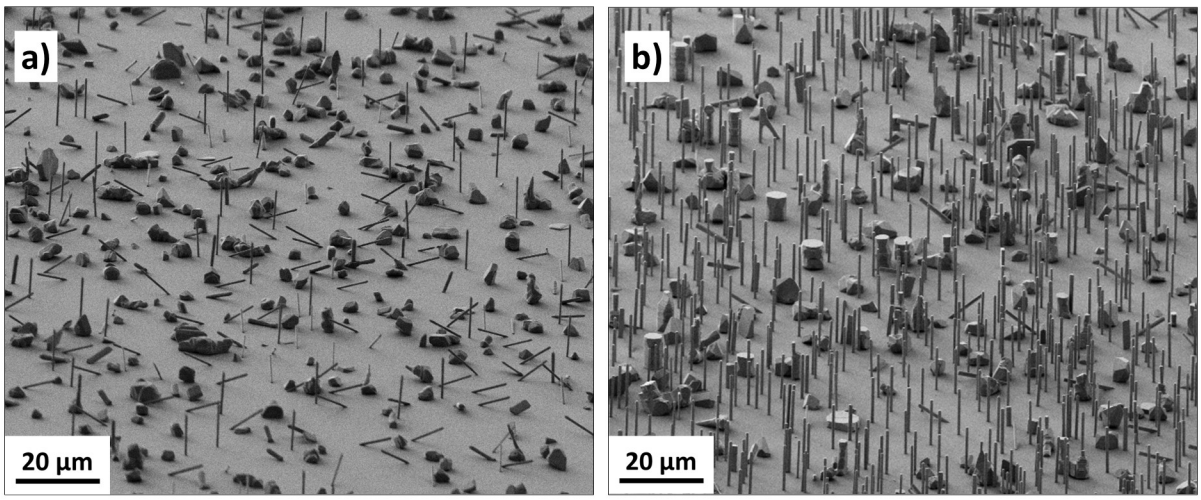

Figure II.14: Tilted-view SEM images of InAs NWs grown on bare Si(111). a) Growth was preceded by a In pre-treatment under an InCl partial pressure of 6.6×10^{-3} atm for 5 minutes. b) Substrates were exposed to an As_4 partial pressure of 5×10^{-5} atm during the heating phase.

Under In and As environment, different Si(111) surface reconstructions can be observed. As-terminated and In-incorporated Si(111) surface correspond to (111)A type surface while As-incorporated and In-terminated Si(111) correspond to (111)B type. NWs on (111)A surface grow along 3 equivalent (111)B direction forming an angle of 19.6° with respect to the substrate surface. Thus, we can suppose that the presence of a majority of tilted NWs observed on figure II.14-(a) can be due to In terminated Si(111) which is the result of the InCl pre-treatment. We can also consider that no In atoms adsorb on the Si(111) surface resulting in a non-polar surface. On figure II.14-(b), it is reasonable to assume that the As_4 pre-treatment leads to surface reconstruction which in turns results in a majority of vertical NWs. Moreover, we clearly see an increase of the NW density.

For the study presented in section II.3.2, the substrates were exposed to an As_4 partial pressure of 3.75×10^{-4} atm. The partial pressure was arbitrarily increased to ensure vertical growth at higher growth temperature. However, it would be essential to study the efficiency of this surface pre-treatment under different substrate temperatures and different P_{As_4}, in order to avoid over-consumption of arsine. Finally, the results presented here demonstrate the need of an arsenic pre-treatment to ensure the nucleation of vertical NWs and increase their density.

II.3.4 Investigation of the optical properties

In this section, I present the photoluminescence and the absorptance of InAs NWs grown on Si(111) and GaAs(111)B. Photoluminescence (PL) spectroscopy was performed using a Brucker-Vertex 70 FTIR spectrometer equipped with a KBr beam-splitter and a cooled InSb detector. PL was excited by a 780 nm laser diode. The samples were cooled at 10K using a closed cycle He flow cryostat.

Low-temperature PL spectra of InAs NWs grown on GaAs(111)B and Si(111) are shown in figure II.15-(a) and (b), respectively. For NWs grown on GaAs(111)B, a strong peak at 0.445 eV with a FWHM of 32 meV was observed, designated as a1. NWs grown on Si exhibited a dominant PL emission centred at 0.413 eV with a FWHM of 34 meV, designated as a2. A lower PL intensity recorded from InAs NWs grown on Si compared to GaAs is probably due to the lower NWs density and diameter (lower material volume).

The PL peak energy a1 (0.445 eV) in Figure II.15-(a) is blue-shifted compared to bulk zinc blende (ZB) InAs at 0.418 eV. Similar peaks have already been observed in the literature. Koblmuller et al. [93] observed a shift of the photoluminescence spectra when varying the NWs diameter. By decreasing the NWs diameter, the principal PL peak was shifted to higher energy. This blue shift was attributed to quantum confinement (QC) for very thin InAs NWs ($\sim$50 nm). However, the NWs studied here are too large ($\sim$350 nm) to exhibit QC. In ref. [94, 95, 96], a PL peak between 0.45 eV and 0.48 eV was associated with wurtzite (WZ)-dominated, and mixed WZ-ZB InAs NWs. This was supported by Bechstedt and Belabbes [97] who estimated the bandgap energy for different polytypes (0.411, 0.431, 0.440, and 0.481 eV for the 3C, 6H, 4H, and 2H polytypes, respectively). The presence of both cubic and hexagonal phases in InAs NWs has already been observed in section II.2. The PL

peak emission a2 observed at 0.418 eV is probably due to the contribution of ZB phase of InAs, confirming the presence of both WZ and ZB phases in InAs NWs grown by SAG-HVPE. The dominant PL peak energy a2 at 0.413 eV of InAs NW grown on Si in Figure II.15-(b) corresponds to the zinc blende band-to-band transition and the shoulder a3 observed at 0.38 eV is attributed to emission from defects [98].

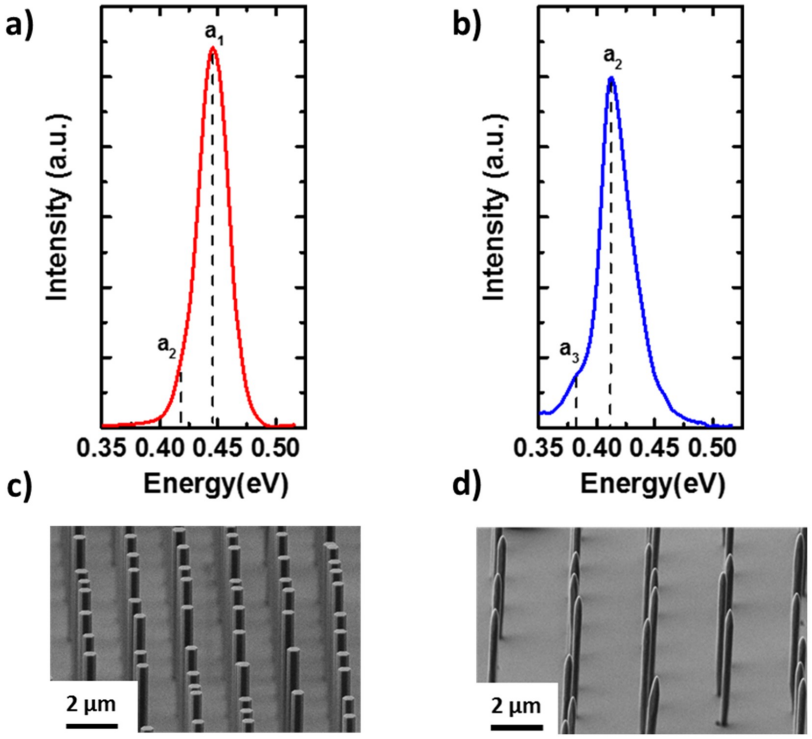

Figure II.15: PL spectra at 10 K of InAs NWs grown on (a) GaAs(111)B and (b) Si(111). (c, d) Corresponding SEM images. The pitch are respectively 2 µm and 2.5 µm. Holes diameter is 60 nm.

To further explore the potential of InAs NWs for optical applications, especially photodetectors, we examined their optical absorptance as measured by Fourier transform infrared (FTIR). FTIR microscopy was performed at room temperature using a BRUKER Hyperion 3000 system with a halogen source and MCT detector. Absorptance spectra ($A(\lambda)$) were calculated as $A(\lambda)$=1-$R(\lambda)$-$T(\lambda)$, where the reflectance spectra ($R(\lambda)$) and transmittance spectra ($T(\lambda)$) were measured with a 15$\times$ objective lens. A knife-edge aperture was used to ensure illumination of the array only. A gold-coated glass slide was used as a reference for reflectance measurements, and unobstructed air was used as a reference for transmittance measurements. For this purpose, NWs were grown on high resistivity (5.107 Ωcm) patterned GaAs(111)B substrates to avoid free-carrier absorption from the substrate. FTIR spectra are shown in Figure II.16 for three different NW diameters (310, 530, 630 nm).

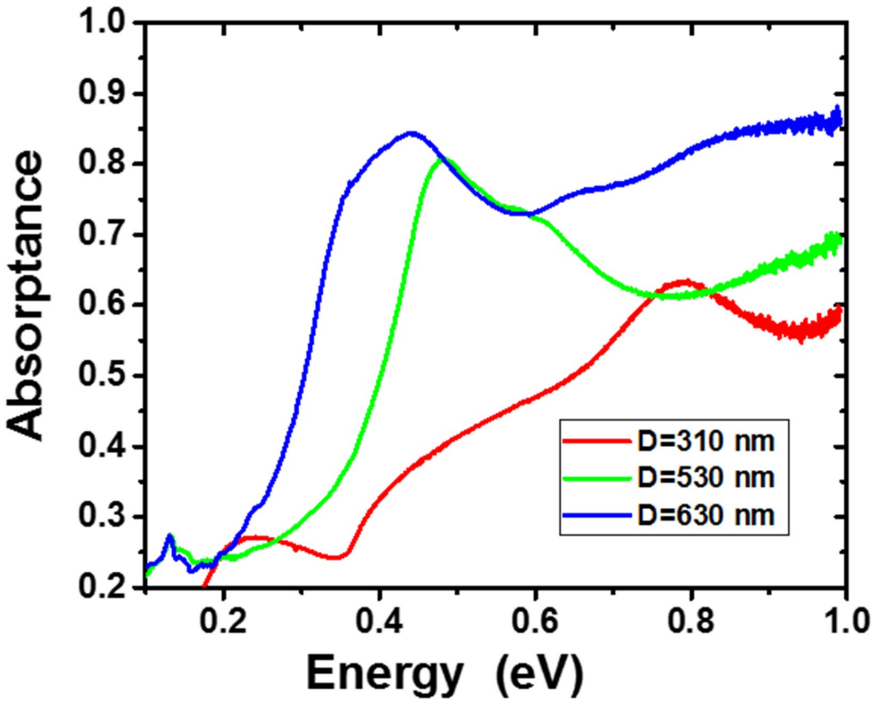

Figure II.16: Room temperature FTIR spectra of InAs NWs with different diameters (D) at constant pitch (4 µm).

The FTIR spectra exhibited strong optical absorptance with a primary absorptance peak that red-shifted with increasing NW diameter. NWs support leaky mode resonances (primarily HE11 modes), resulting in strong optical absorption at certain resonant wavelengths [99]. The absorption peak red-shifts with increasing NW diameter due to the electromagnetic boundary conditions, indicating that these NW arrays might be useful for multispectral infrared photodetectors [99, 100]. Based on prior simulations [100], the HE11 resonance peak is expected at 0.81, 0.56 and 0.49 eV for InAs NWs of diameter 310, 530 and 630 nm, respectively, in reasonable agreement with the experimental results in Figure II.16. The resonance peaks broaden with increasing diameter, possibly due to near-field coupling between adjacent NWs [71]. In addition, FTIR results may be affected by scattering. In the absence of scattering, FTIR measurements agree almost perfectly with simulated spectra [101]. Scattering, if present, results in a loss of light and an apparent increase in absorptance. Thus, scattering from parasitic growth likely resulted in some background absorptance in the measured FTIR spectra. These measurements constitute a preliminary step to develop devices. This work will be continued after this PhD within the collaboration between Institut Pascal and McMaster University.

II.4 Selective area growth of GaAs NWs

The study presented in this section is part of our collaboration with IBM Europe in the framework of an ERC project named ENUF for Evaluation of Novel Ultra-Fast selective III-V epitaxy. The aim of the project is to evaluate the technical feasibility of combining Template-Assisted Selective Epitaxy (TASE) with HVPE. TASE, which is also known as conformal growth, has many advantages:

1. Starts epitaxy from a single nucleation point $\rightarrow$ Avoids threading dislocations.
2. Keeps area of epitaxial interface small.
3. Expands seed and guides growth within oxide template $\rightarrow$ Guided growth.

IBM has already developed MOVPE-based TASE for photonic applications within the ERC project PLASMIC. However, using MOVPE to deposit crystals in the template has two important limitations: first, the low crystal growth rates so far obtained ($\sim$10 nm/min), lead to long process times ($>$1 h). Second, such long process times lead to unwanted deposition of material on the wafer due to the limited process selectivity. Using HVPE, growth rates of GaAs as high as 100 µm/h can be achieved, which can reduce the process time about 100$\times$ as compared to MOVPE. HVPE also allows a large flexibility for selective and localized growth on large, patterned substrates. Moreover, HVPE conformal growth of high quality GaAs on Si has already been demonstrated at Institut Pascal [102].

In this section I first show the selective growth of GaAs NWs on patterned GaAs(111)B in order to demonstrate the very good selectivity of HVPE over a large surface. Then, I study the direct growth of GaAs on Si(111). The demonstration and optimization of the growth has been facilitated by the development of InAs growth on Si(111). These preliminary studies finally enable to achieve the TASE of GaAs material on GaAs and Si substrates using HVPE.

II.4.1 Growth of GaAs NWs dense arrays on GaAs substrates

I first demonstrate the growth of well-ordered GaAs NWs on SiNx patterned GaAs(111)B. The pitch is 500 nm and holes diameter is 240 nm (figure II. 17). The growth temperature is 740 °C and the III/V ratio is 1.6. Growth was perfectly selective on a large area of the substrate (figure II.17-(a)) and consisted of vertically aligned NWs delimited by six equivalent $\{110\}$ lateral facets and a (111)B top facet. The NWs have a length of 1 µm and a diameter of $\sim$310 nm resulting in a aspect ratio of $\sim$3.

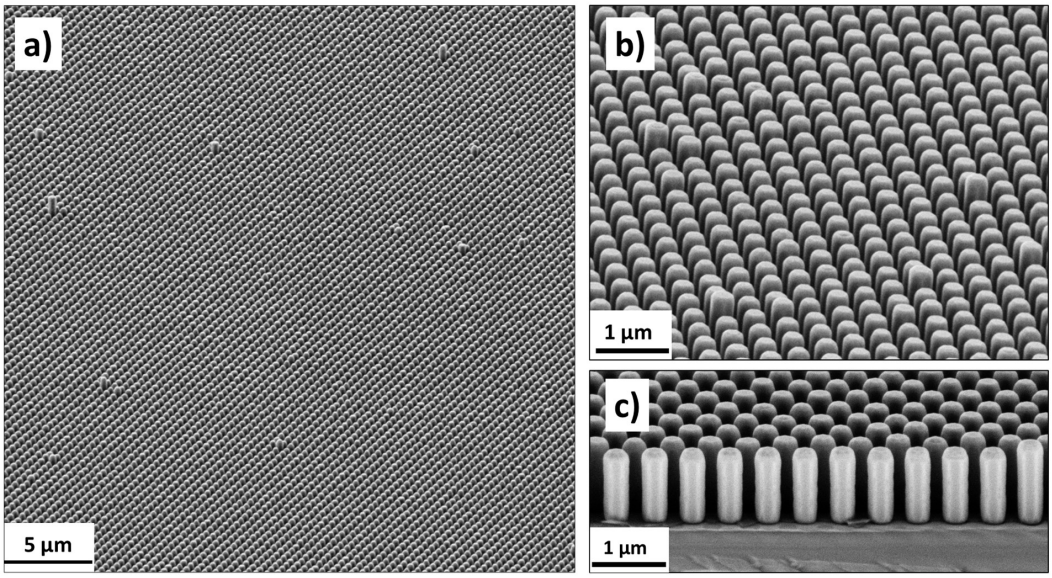

Figure II.17: Tilted-view SEM images of GaAs NWs grown on patterned GaAs(111)B at 740 °C. The sample shows a very good selectivity and a high homogeneity over a large surface. Pitch is 500 nm and holes diameter is 240 nm.

In HVPE, it is commonly assumed that there is no influence of the mask coverage ratio on the crystal morphology. However, growth at the nanometric scale with such high density has never been reported. Thus, it is interesting to investigate the effect of the growth parameters on the NWs morphology in order to determine the underlying growth mechanisms of GaAs NWs. Here, I show the effect of the growth temperature on the axial and radial growth rates of GaAs NWs (see Figure II.18). Pattern dimensions are P=500 nm and D=240 nm. The axial growth rate decreases from 6 µm/h at 740 °C to 3.5 µm/h at 785 °C while the radial growth rate is nearly constant.

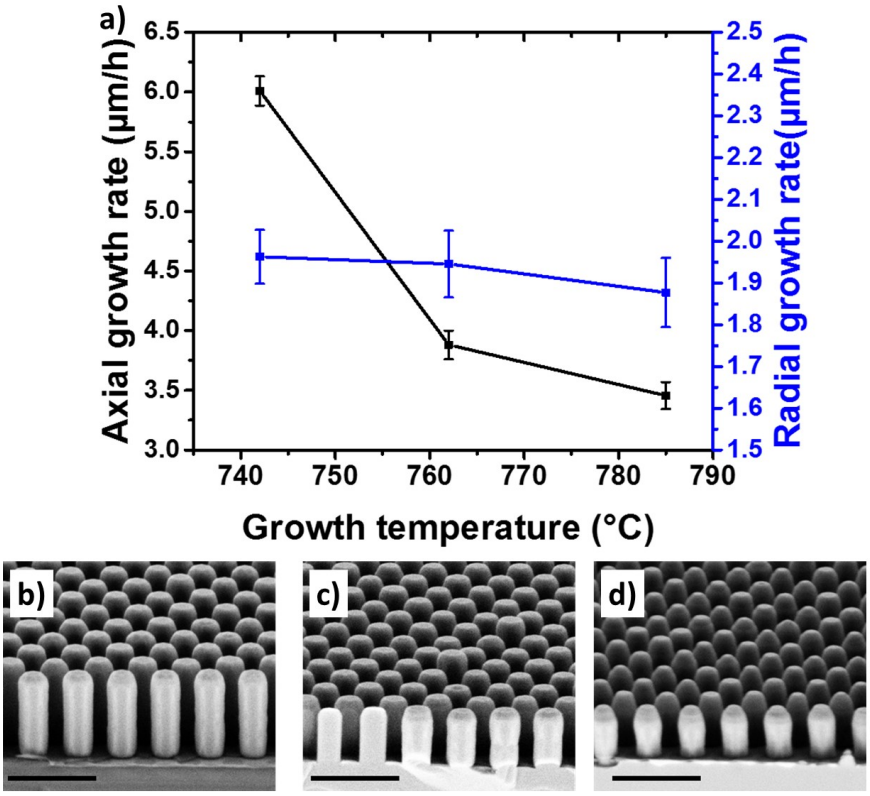

Figure II.18: (a) NWs axial and radial growth rates as a function of the growth temperature. Tilted-view SEM images of GaAs NWs grown on GaAs(111)B substrate at different growth temperatures: (b) 740 °C, (c) 760 °C and (d) 785 °C. Scales bars are 1 µm. Pitch is 500 nm and holes diameter is 240 nm.

The decrease of the axial growth rate when increasing the growth temperature is due to a decrease of the adsorption of precursors. Moreover, at such temperature there is a high probability that desorption of adsorbed molecules occurs before their decomposition on the surface. This desorption before decomposition is much more pronounced for GaCl molecules which easily desorb before their dechlorination. Finally, it shows that we are in a temperature range where the growth rate is limited by the material input from the gas phase. This lack of material is confirmed in figure II.19, where the variation of NWs morphology with the As_4 partial pressure is plotted. The As_4 partial pressure is varied from 5.6×10^{-4} atm to 1.1×10^{-3} atm. The growth temperature is 740 °C.

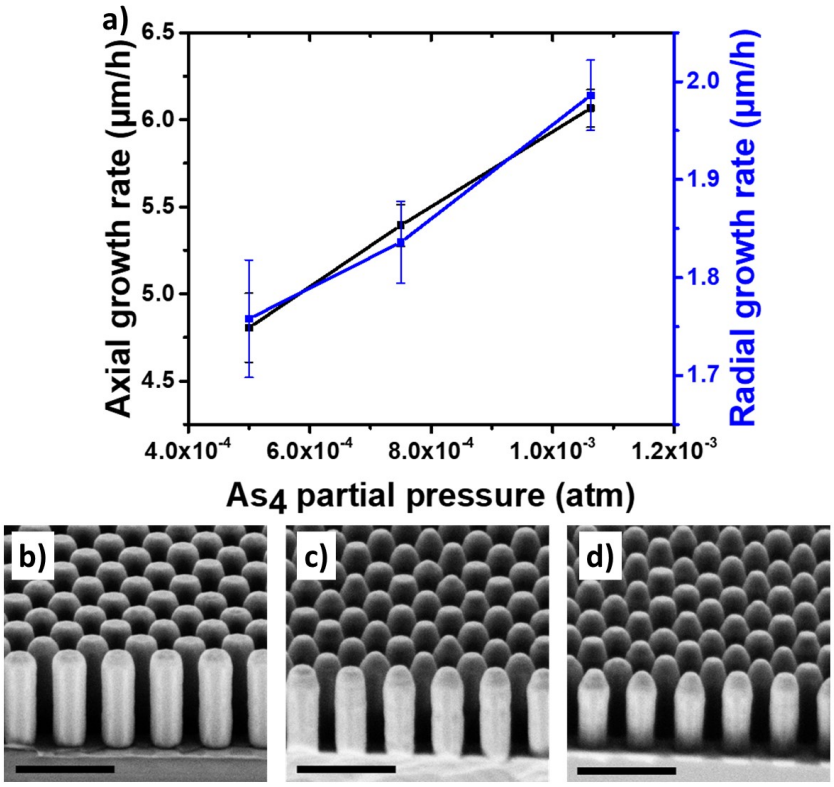

Figure II.19: (a) NWs axial and radial growth rates as a function of the As_4 partial pressure. Tilted-view SEM images of GaAs NWs grown on GaAs(111)B substrate at different As_4 partial pressure: (b) 1.1×10^{-3} atm, (c) 5.6×10^{-4} atm and (d) 7.1×10^{-4} atm. Scales bars are 1 µm. Pitch is 500 nm and holes diameter is 240 nm.

A slight increase is noticed of both axial and radial growth rates with the As_4 partial pressure. This behavior is surprising for the HVPE process. For usual GaAs growth, it was shown that the arsenic species adsorb on the surface without desorbing. It means that an increase of the As_4 partial pressure is useless because the surface is always saturated with As ad-species. Here, NWs are grown at higher temperature meaning that adsorption/desorption ratio of arsenic molecules is lower and its desorption may be considered. The high desorption of both As_4 and GaCl molecules at such high temperature will be confirmed in the part of this work dealing with the growth of GaAs NWs on Si(111).

To determine the influence of the pitch on the NWs morphology, I have compared the growth of GaAs NWs on patterned GaAs(111)B with pitch of 500 nm and 1 µm. Figure II.20 shows NWs grown on patterned GaAs(111)B with a pitch of, (a) 500 nm, and (b) 1 µm. One can observe the length inhomogeneity on figure II.20-(b), that is why length was determined from statistical analysis. The dimensions of the NWs are D=345 nm / L=490 nm for (a) and D=375 nm / L=590 nm for (b). The growth temperature is 740 °C, III/V ratio is 1.5 and the growth time is 10 minutes.

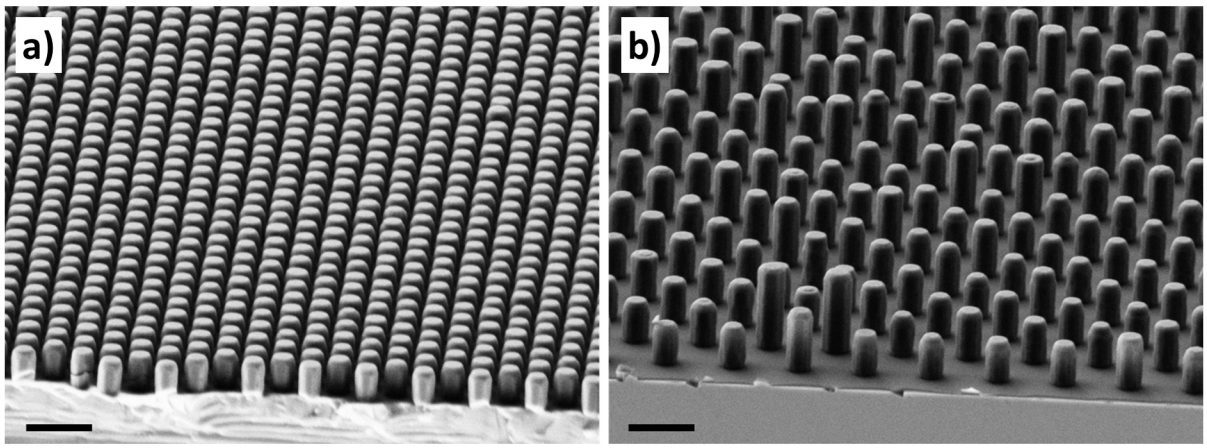

Figure II.20: Tilted-view SEM images of GaAs NWs grown on GaAS(111)B substrate with, (a) P=500 nm and, (b) P=1 µm. The scale bars are 1 µm. Pitch is 500 nm and holes diameter is 240 nm.

The lower dimensions of NWs grown on substrate with P=500 nm may be explained by a depletion of the gas phase. This latter can be induced by the larger surface of growing crystal in contact with the gas phase for P=500 nm. Then, it is interesting to calculate the surface of material in contact with the gas phase and also the volume of grown material. First, I calculate the number of NWs for 1 μm^2 of substrate surface. For pitches of 500 nm and 1 µm, there are 5.2 and 1.3 NWs per μm^2, respectively. Then, if we consider the final shape of the NWs, the NWs' total surface for 1 μm^2 of substrate are 3 μm^2 for P=500 nm and 1 μm^2 for P=1 µm. The difference of radial and axial growth rate between P=500 nm and P=1 µm is not significant to confirm the existence of a gas-phase depletion. Moreover, the volume of grown material per μm^2 is 3 times higher for P=500 nm, confirming the absence of gas phase depletion. NWs dimensions are summarized in table II.1.

	P=500 nm	P=1 µm
NWs length (nm)	490	590
NWs diameter (nm)	345	375
NWs density (NWs/μm^2)	5.2	1.3
NWs surface per μm^2	3 μm^2	1 μm^2
NWs volume per μm^2	0.25 μm^3	0.08 μm^3

Table II.1: GaAs NWs dimensions for P=500 nm and P=1 µm.

II.4.2 GaAs growth on silicon substrates

In the framework of our collaboration with IBM Europe, I have developed the direct epitaxy of GaAs material on silicon. Finding the growth conditions enabling nucleation of GaAs on silicon was essential in order to achieve TASE-HVPE on silicon. I present here the study of GaAs growth on patterned Si(111) substrates. Due to the lack of good quality substrates, I was not able to conduct

a systematic study as a function of the different growth parameters. However, the results that were obtained give a first understanding of the different trends observed from the experiments.

Self-catalyzed GaAs NWs grown on Si(111) using HVPE has already been demonstrated by Z. Dong [103]. The growth was achieved at low temperature (600 °C) and high III/V ratio (∼30). Such condition were not suitable for self-catalyzed growth of GaAs NWs due to gallium droplet stabilization issues. Here, I show the growth of GaAs on Si(111) at high temperature (>715 °C) and low III/V ratio (1.5 to 4.5). As for InAs growth on silicon, an additional surface preparation step of the Si(111) substrate under As_4 atmosphere was introduced during the pre-growth heating ramp. At high input partial pressure of As_4 $\sim 7.6 \times 10^{-4}$ atm the significant desorption rate of As atoms from the surface is compensated. Once the As atoms are available on the Si surface, the growth of GaAs can easily be initiated. On figure II.21 are displayed GaAs crystals grown on patterned Si(111) at 715 °C and 760 °C. At 715 °C, polycrystalline crystals are grown while well faceted hexagons are obtained at 760 °C.

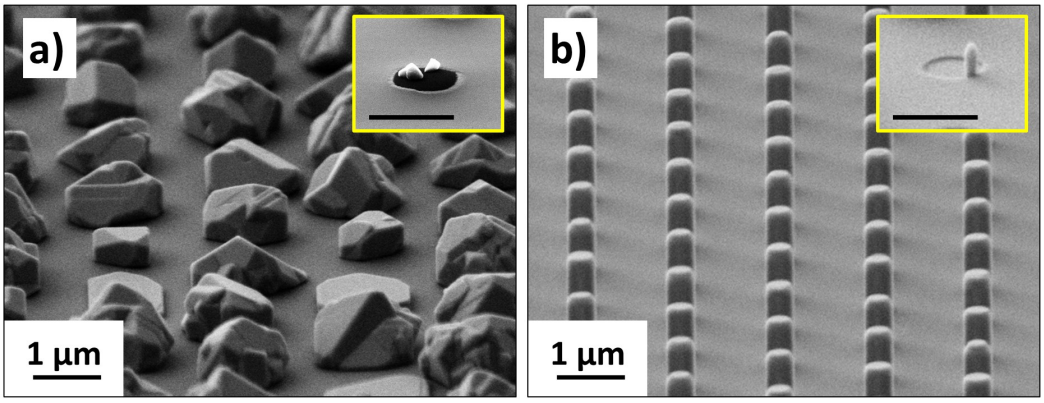

Figure II.21: Tilted-view SEM images of GaAs crystal grown on SiNx patterned Si(111) substrate at (a) 715 °C and (b) 760 °C. The diameter of the holes is 350 nm and the pitch is 1.5 µm. The insets show the initial stage of growth after 1.5 minute of growth. The scale bars are 500 nm.

As shown in the inset of figure II.21-(a), at 715 °C, GaAs crystals with many different facets nucleate. The coalescence of these poor quality crystals leads to polycrystalline GaAs corresponding to the majority of the grown material observed at 715 °C. When the temperature is increased to 760 °C, higher quality nuclei formed and lead to the growth of well defined hexagonal NWs. Recently, Yeu et al. [104] theoretically have calculated the surface energy of different low index facets and the chemical potentials of adsorb Ga and As atoms. They have calculated temperature and As_4 partial pressure domains in which NWs grow. Based on this model and by considering our As_4 partial pressure, axial growth along the (111)B direction is expected at temperature above 740 °C which is in accordance with our observations. Finally, even if very good selectivity is achieved at 715 °C, high temperature is needed to grow good crystalline quality GaAs material.

	Growth temperature (°C)	GaCl partial pressure (atm)	As_4 partial pressure (atm)	Figure
Conditions 1	785	3.3×10^{-3}	7.2×10^{-4}	II.22-(a,b)
Conditions 2	760	3.3×10^{-3}	7.2×10^{-4}	II.22-(c)
Conditions 3	785	3.3×10^{-3}	3.6×10^{-4}	II.22-(d)
Conditions 4	785	1.6×10^{-3}	7.2×10^{-4}	II.22-(e)

Table II.2: Summary of the growth conditions of GaAs NWs discussed in this section.

Figure II.22 shows tilted-view SEM images of regularly and vertically aligned GaAs NWs grown on patterned Si(111) substrate with 350 nm-diameter holes and a pitch of 1.75 µm. NWs are grown under various growth conditions which are summarized in Table II.2. As for InAs material, it has been reported [9] that GaAs growth on Si(111) could result in both vertical and tilted 19.6° oriented GaAs structures. The observation of strictly vertical NWs on the whole Si substrate implies that the NWs were all grown along the $<111>$B direction. This confirms that the Si(111) was As-terminated following the As_4 surface treatment.

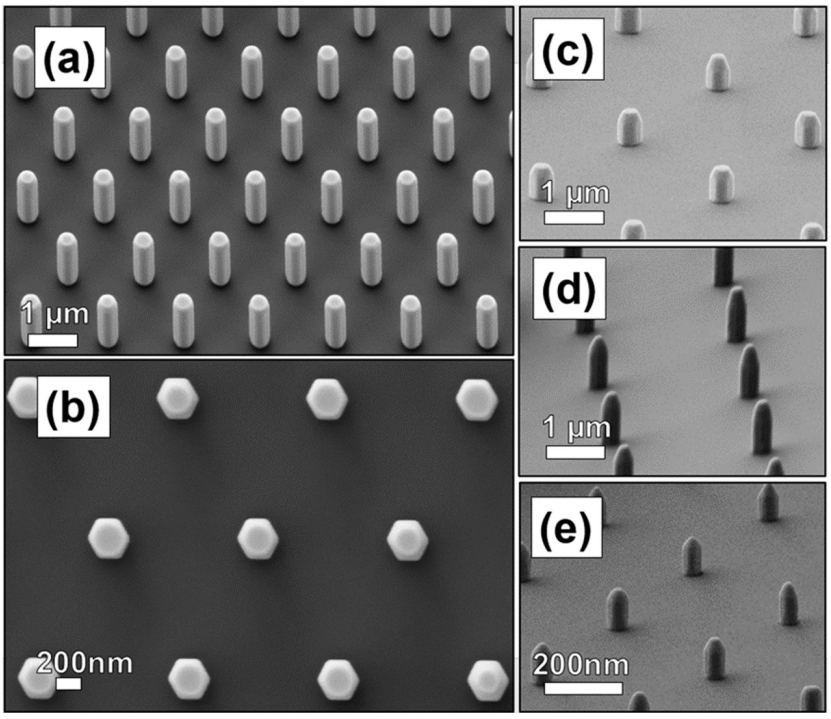

Figure II.22: (a) Tilted-view and (b) top-view SEM images of well-ordered and vertically aligned GaAs NW arrays grown on Si(111) substrate under optimized growth conditions (conditions 1). The diameter of the circular holes is 0.35 µm and the pitch is 1.75 µm. Tilted-view SEM images of samples obtained under (c) conditions (2), (d) conditions (3) and (e) conditions (4) showing the morphological changes with growth conditions of GaAs NWs on patterned Si(111) substrate with 350 nm-diameter hole and a pitch of 3.5 µm.

The results reported in figure II.22 reveal that the NWs keep mostly a pencil-like shape delimited by the six equivalent $\{110\}$ and (100)-like top facets. The top (111)B facet appears when the height of the wire is the shortest, for example at lower growth temperature of 760 °C, as seen in Figure II.22-(c). In depth and comprehensive studies of the evolution of the intrinsic growth anisotropy of GaAs, performed on patterned substrates of various orientations by HVPE, can be found in Ref [78]. Based on these reviews, let us now comment on the GaAs NWs shapes. It is assumed that the growth rate of the $\{110\}$ facets, which consist of rows of Ga-As, is usually very low over a wide range of HVPE conditions because of the low adsorption of As and GaCl on the surface even at low growth temperature. Thus, the radial growth rate of the $\{110\}$ facets remains low whatever the growth conditions. The top (111)B facet undergoes a slow dechlorination step. Its growth rate can be increased by increasing the growth temperature, as shown by the NWs grown at 760 °C and 785 °C, showing lengths of 0.6 µm and 1.6 µm, respectively. At high temperature, growth rate is limited by the adsorption of precursors. In fact, by decreasing the As_4 partial pressure (conditions 3) or decreasing GaCl partial pressure (conditions 4) the NWs length is decreased. This confirmed the observations on GaAs NWs grown on GaAs(111)B substrate, for whom the axial growth rate of GaAs NWs decreased when increasing growth temperature or decreasing As_4 partial pressure.

In the framework of the ENUF project, the aim was to develop GaAs growth on Si with a focus on the enhancement of the lateral growth rate. I demonstrate here that the morphology of the growing GaAs crystal can be switched to large platelets by changing the apertures diameter. Several authors showed that the axial and radial growth rates of GaAs NWs grown by SAG-MBE or MOVPE were strongly dependent on the pitch and the collection area. The latter is strongly influenced by the diffusion of adatoms on the mask [105]. This process is not relevant for HVPE because the GaCl precursor does not crack on the mask and desorbs quickly. However, a strong dependence between the aperture size and the final shape was noticed when the substrate was silicon. Figure II.23 shows SEM images of GaAs structures grown by SAG on Si(111) substrates patterned with 500 nm-diameter holes under conditions (2). We can see a large overgrowth on the mask (at a rate of 16 µm/h), so that the structures are micro-platelets. The axial growth rate is slightly reduced from 2.60 µm/h to 2.00 µm/h when the aperture size increases from 0.35 µm (Figure II.22-(c)) to 0.50 µm (Figure II.23). Such a decrease of the axial growth rate of GaAs NWs with the aperture size has already been observed [9], [106]. Consequently, the crystal shape evolves from an hexagonal NW to a well-faceted micro-platelet whatever growth conditions, for different aperture/hole diameters: 0.50 µm , 0.70 µm and 1.00 µm.

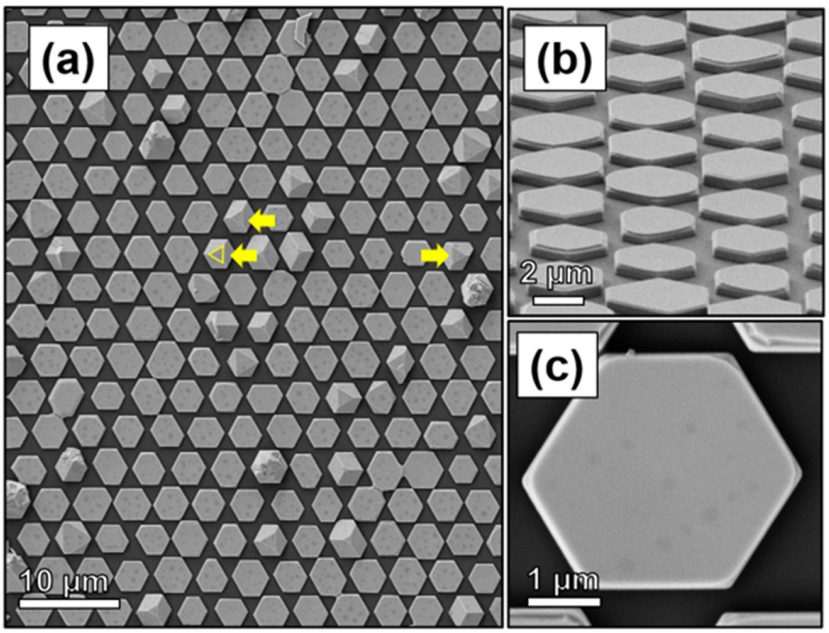

Figure II.23: (a) top-view and (b) tilted-view SEM images of hexagonal GaAs micro-platelets grown on Si(111) substrate under growth conditions 2. The arrows indicate triangular thin mesa surrounded by $\{110\}$ facets. (c) Closer top-view SEM image on a selected micro-platelet showing a perfect hexagonal morphology. The diameter of the circular holes is 0.50 µm and the pitch is 2.50 µm.

Similar platelets were obtained on patterned GaAs(111)B substrates with 50 nm-diameter holes [107]. The growth of such structures, even at small opening diameters, was attributed to the formation of stable As-trimers following the (2×2) surface reconstruction under high partial pressure of element V and low temperature, thus suppressing axial growth along the (111)B direction. However, the formation of stable As-trimers may not be the cause for the micro-platelets grown in this work due to the high growth temperature. Moreover, if As-trimers formation was involved, we would expect the micro-platelet morphology even for the substrate pattern with small 350 nm-diameter hole (where NWs/nanorods are indeed grown). For Tomioka et al. [9], the size openings determine the number of 2D islands during initial nucleation. The coalescence of these islands with rotational twins results in the generation of 3D islands. The further coalescence of the 3D islands in the large apertures ($D >$ 600 nm) generates three-fold-symmetry as well as unexpected lateral facets. Smaller openings ($D <$ 400 nm) promote the formation of one 2D island per aperture that stimulates the growth of hexagonal GaAs NWs. These findings are supported by Ikeijiri et al. [50] through a thermodynamic model of the variation of Gibbs free energy. The authors show that the transition from a tetrahedron with three-fold-symmetry facets, which corresponds to the first nucleation step, to a perfect hexagonal shape is more favourable and faster in the case of smaller openings. All these trends are in agreement with our experimental observations and sustain the transition from a perfect hexagonal wire to platelet as a function of the aperture sizes of patterned silicon substrate.

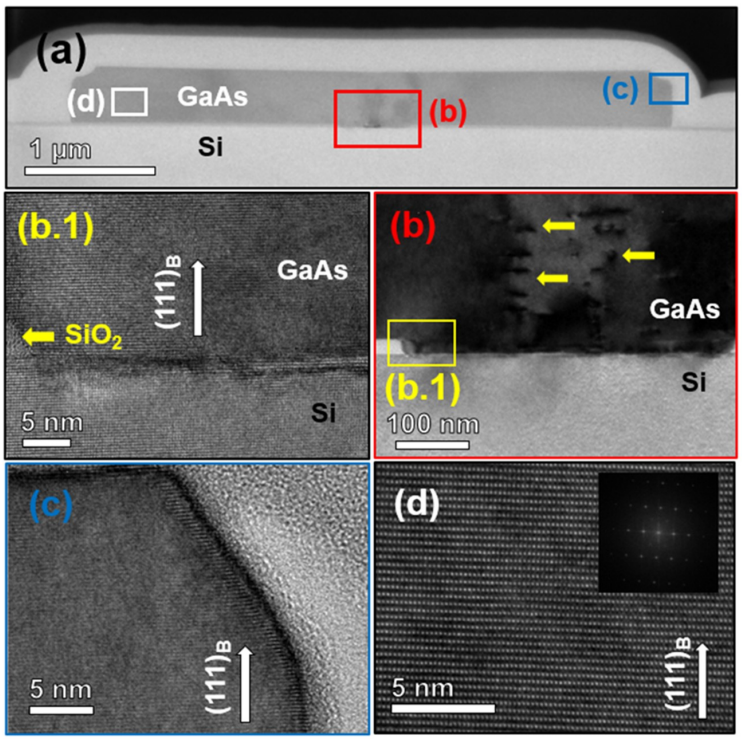

Figure II.24: TEM investigation on a selected GaAs micro-platelet grown on Si(111) in conditions 2. (a) Low-resolution TEM image showing an overview of the cross section of the platelet. (b) and (b.1) TEM images reveal the GaAs crystalline quality at the interface with the Si substrate and at the top edge of the aperture, respectively. (c) End facets of GaAs platelet exhibiting a quasi-perfect crystalline quality. (d) HR-TEM image shows that the growing GaAs crystal is defect-free. The inset is the corresponding FFT pattern of a pure GaAs ZB crystal.

Cross-sectional TEM images of a selected GaAs micro-platelet are given in Figure II.24 to illustrate the crystal quality. The platelets were initially prepared by FIB for cross-section images in a direction perpendicular to the [110]. The HR-TEM image of Figure II.24-(b) taken in the opening area reveals few structural defects, such as dislocations, as indicated by the arrows. Such defects can appear after coalescence of different islands, which nucleate predominantly at the aperture edges. The interface between the GaAs platelet, the Si substrate and SiO_2 mask exhibits a perfect crystalline quality, confirming that the direct epitaxy is perfectly achieved. The entire crystal is pure ZB and free of crystalline defects (see Figure II.24-(c) and (d)).

Structural characterization by HR-TEM of GaAs nanowires was also carried out to check their crystalline quality. They were grown using growth conditions 1. A vertical cross section perpendicular to the [110] direction was prepared by Focused Ion Beam (FIB). In Figure II.25, one can find cross-section TEM (a) and HR-TEM images of selected GaAs NWs taken at the top of NWs (b) and at the interface with the substrate (c). The NW diameter is about 0.4 µm with a length of 1.6 µm. High density of structural defects can clearly be found along the [111]B growth direction, in particular twinnings, as can be seen in close up in Figure II.25-(b).

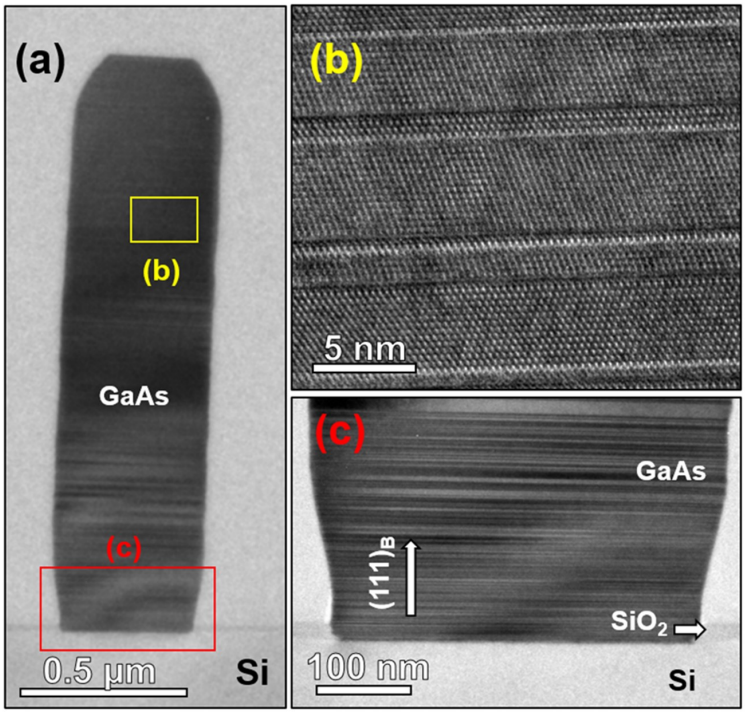

Figure II.25: (a) Low resolution cross-section TEM image of GaAs nanowire grown on Si(111) substrate (conditions 1). (b) HR-TEM image taken from the top part of the nanorod showing the crystalline structure of GaAs with a large zone free of twinning and stacking faults. (c) HR-TEM image taken from the bottom part of the nanorod showing the interface with Si (patterned substrate with 350 nm-diameter hole and a pitch of 3.5 µm).

Polytypism is also observed at the bottom part of the rod near the substrate interface. These alternate stackings between Zinc-Blende (ZB) and Wurtzite (WZ) are commonly observed during the growth of GaAs NWs along the [111] direction. Their formation might be attributed to the small difference in the internal formation energy between the two phases, which comes mainly from the electrostatic interaction between the third-nearest-neighbor atoms [107, 108, 109]. The wurtzite phase can also be observed when twinning of the ZB phase occurs every monolayer [110]. Few studies have properly shown the possible control of the crystal phase of GaAs NWs grown along the [111] direction through a VS process.

As mentioned previously, the growth of GaAs along the (111)B direction can involve the nucleation of tetrahedrons with three-fold symmetry or hexagons with six-fold symmetry. In the case of growth involving tetrahedron, it has been demonstrated by [53] and [110] that the density of twins can be reduced by increasing the mask opening (i.e, the diameter of the NWs). For GaAs NWs, we have no proof of tetrahedron nucleation during the growth. As reported on figure II.26, I demonstrate the nucleation of tetrahedrons during the growth of the GaAs platelets. The platelets are grown under conditions (2), on patterned Si(111) with holes diameter of 1 µm and a pitch of 5 µm.

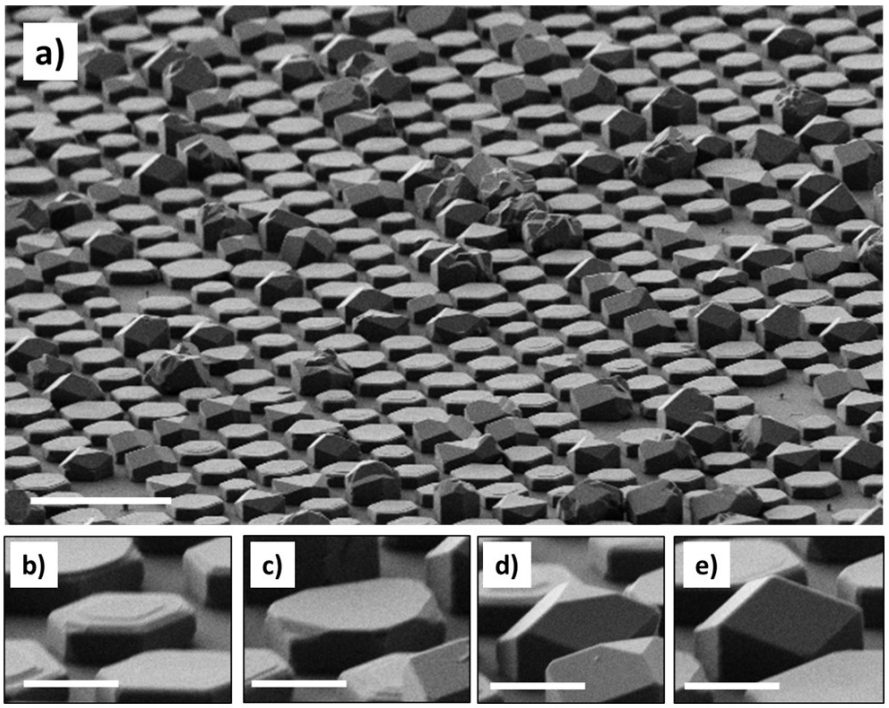

Figure II.26: Tilted-view SEM images of GaAs platelets grown on patterned Si(111) substrate. Platelets exhibiting triangular top facet prove that nucleation of tetrahedrons during the growth is possible. Scale bar is 10 µm for (a) and 2 µm for (b), (c), (d) and (e).

On figure II.26-(c), (d) and (e), we can see the morphology of GaAs crystals at different stage of the growth. Such morphologies are the proof that tetrahedrons have nucleated. In fact figure (c) corresponds to the lateral expansion of a tetrahedron, resulting in an hexagon-like shape. After this expansion, the three tilted $\{1\bar{1}0\}$ facets extend from the hexagon corner towards the center. The top (111)B surface then shrinks as shown on figure (d). In ref. [110], it is shown that the shrinking of the triangular top surface enables the nucleation of a new tetrahedron. If the new tetrahedron is twinned with respect to the underlying surface, then expansion like figure (c) occurs, otherwise the (111)B surface keeps shrinking and forms a pinned-off crystal as shown in figure (e). These results are consistant with ref. [110] and confirmed the possible nucleation of tetrahedron during growth. Then it allows to explain the difference of twin density observed in figures II.23 and II.24 by different probability of twinned tetrahedron nucleation. Moreover, in ref. [110], the length of twin free segment observed in GaAs NWs grown at 790 °C is similar to what we observe for NWs grown at 785 °C (figure II.25). Finally, in depth study as a function of the growth parameters should be conducted to determine their effects on the twin density and to confirm the growth mechanisms of the GaAs NWs.

To further confirm the crystal quality and check the optical quality of both GaAs nanowires and micro-platelets grown on Si, we have performed PL measurements. Figure II.27 depicts representative PL emission spectra of GaAs micro-platelet (red curve) and GaAs nanowire (blue curve) recorded at low PL temperature (10 K) during the same experiment.

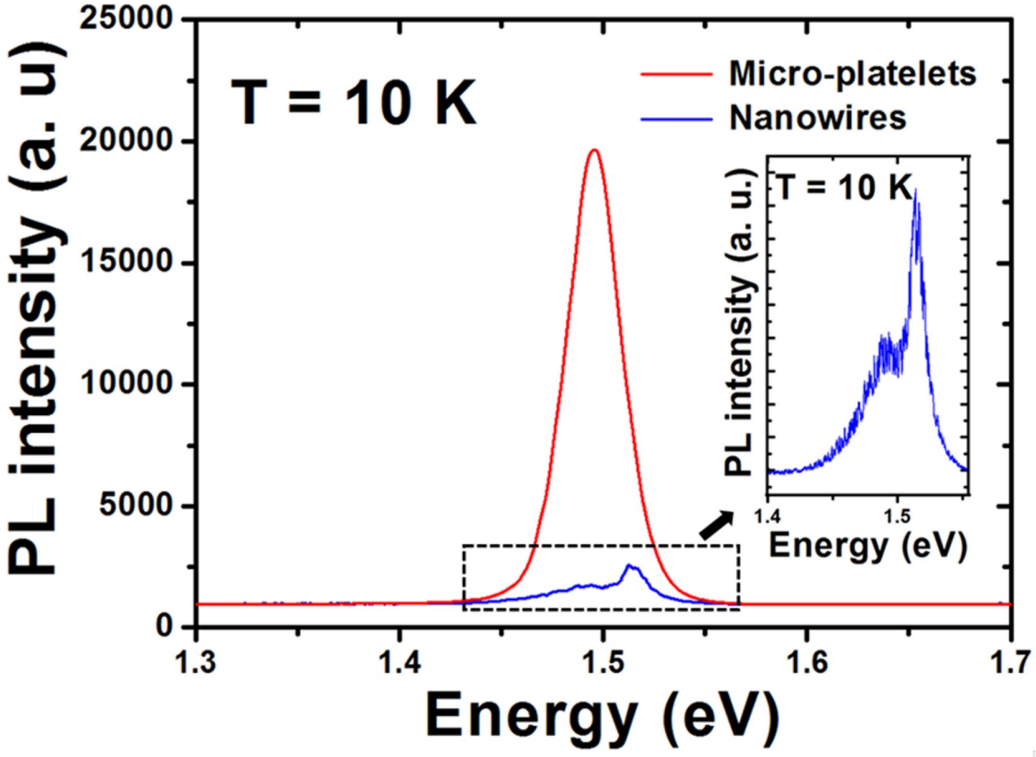

Figure II.27: Low temperature (10 K) spectra of GaAs nanowires (in blue) and micro-platelets (in red) arrays grown on silicon substrate.

Compared to nanowires, the micro-platelets exhibit significantly higher PL intensity. This is mainly due to their high crystalline quality in addition to their large surface excitation density compared to nanowires. It is further seen that the emission peak of micro-platelets is centered around 1.49 eV which is slightly lower than the excitonic emission in bulk GaAs (1.51 eV) [111], whereas two peaks around 1.51 eV and 1.49 eV are observed in the case of nanowires. This strongly suggests that the GaAs material contains a density of free-holes, which means that the GaAs material is unintentionally p-type. These acceptors are attributed to non-intentional carbon or silicon incorporation [112], [105, 106].

II.4.3 TASE-HVPE of GaAs on GaAs and Si substrates

The goal of this first step was to test the quality of the template, the selectivity, and the crystalline quality of the growing GaAs crystal in homoepitaxy condition. A schematic is shown in Figure II.28, illustrating the principle of the confined lateral overgrowth of GaAs by HVPE. The growth is initiated in the central opening and develops to form a layer inside the cavity formed by the GaAs substrate and the dielectric mask.

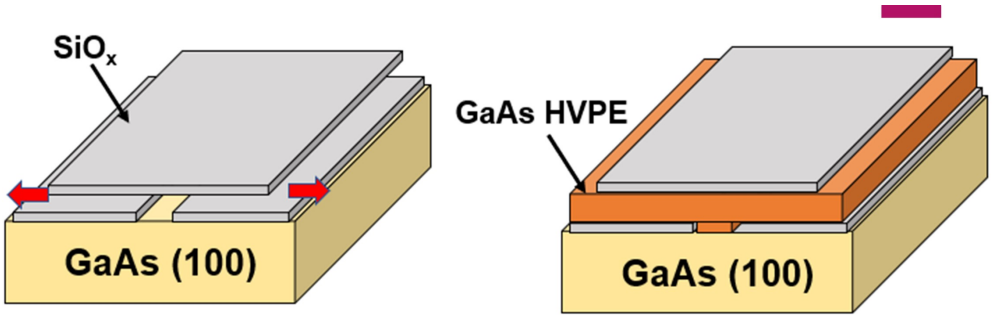

Figure II.28: Schematic of the confined lateral overgrowth of GaAs layer on GaAs (100) substrate.

The growth starts from the central opening and develops inside the cavity to form a perfect layer. The lateral overgrowth is very fast and is controlled by the growth temperature and the vapor phase composition. An example of the lateral overgrowth of GaAs-HVPE on GaAs template is shown in Figure II.29-(a). One could clearly see that the filling is very fast and homogeneous in a short growth time of only 1 minute. The crystal structure of GaAs-HVPE is assessed by TEM investigation. Figure II.29-(b) shows a FIB cross section of a 50 nm thick and 3.5 µm wide GaAs layer, HVPE-grown inside the cavity for 1 minute. The inset is a high-resolution image at the central opening with the substrate, it reveals the early stages of the growth. It confirms that the growth is perfectly initiated from the central opening and the cavity is nicely filled within a very short time. The high growth rate is associated with the use of high supersaturation conditions in the vapor phase.

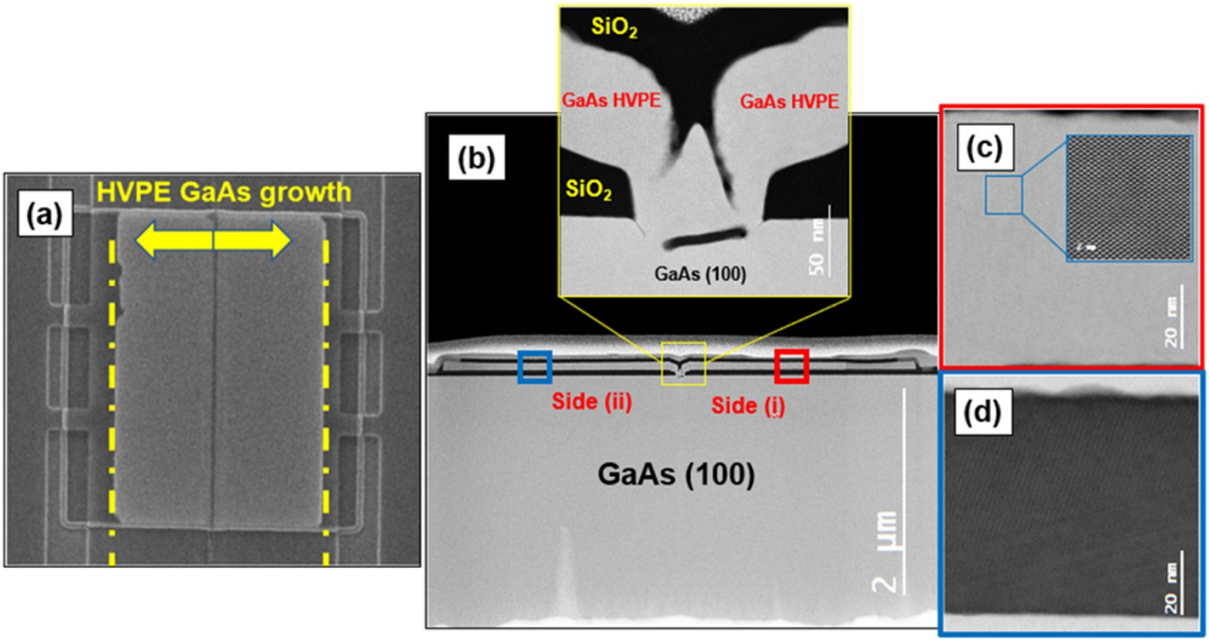

Figure II.29: (a) Top-view SEM image of GaAs layer grown by TASE-HVPE. (b) FIB cross section of GaAs template showing the filling of HVPE-GaAs inside the cavity. The inset is a high-resolution image at the central opening. (c) and (d) are HR-TEM images taken from both sides (i) and (ii) respectively.

Figures II.29-(c) and II.29-(d) show TEM images of GaAs grown by HVPE taken from sides (i) and (ii), respectively. For both sides, the HVPE-GaAs has a Zinc-Blende (ZB) phase with a perfect crystalline quality. The GaAs $\{110\}$ facets grew with an average rate of 105 µm/h. Few twins can be observed on side (ii) which can be related to the dielectric mask quality when interacting with the lateral overgrowth. Overall, this result highlights the good quality of the template and the potential of TASE-HVPE to grow high-quality GaAs layers in a record time.

The last steps focus on TASE-HVPE of GaAs directly on Si(111). Based on the growth conditions developed for the SAG of GaAs platelets on Si(111), TASE-HVPE of GaAs was carried out using III/V ratio of 2.25, at 740 °C for 20 min. Figure II.30 shows the first demonstration of filling GaAs into the micro cavities in a dense array. The overgrown crystals are generally not a problem, these can be selectively removed because the template oxide protects the underlying III-V within the template. The focus is therefore on achieving high-yield and uniform filling of the templates.

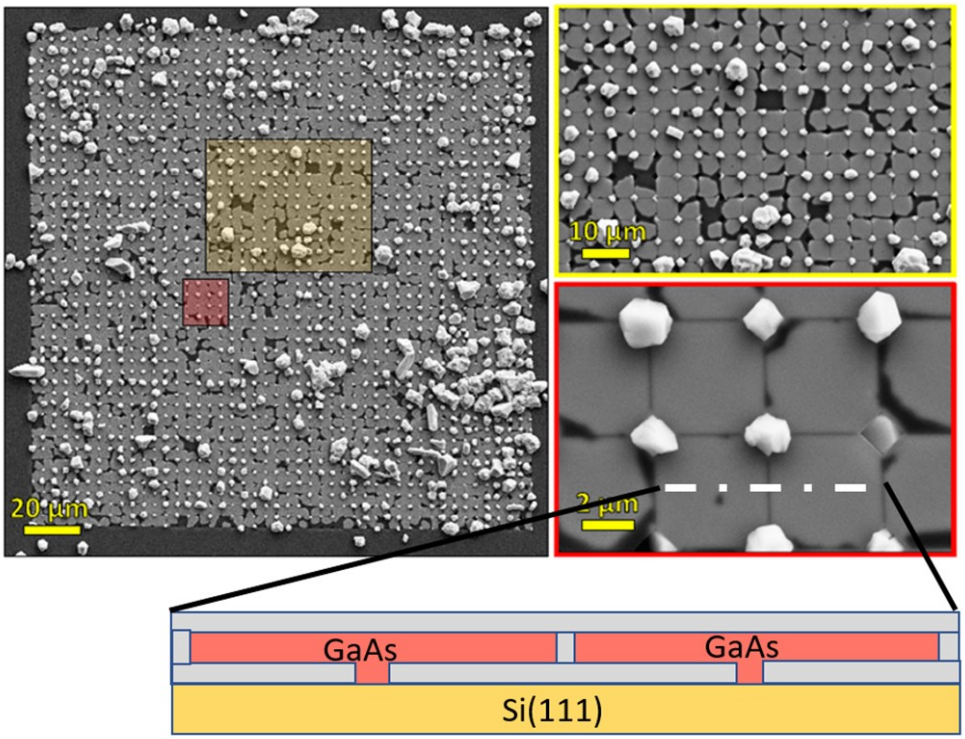

Figure II.30: First demonstration of a dense GaAs array fabricated on a Si wafer using TASE and HVPE. Overview, higher resolution images and a schematic illustrating the cross-section of the structure.

The uniformity of the filling is already remarkable, but missing areas as well as irregular shaped crystals are clearly noticeable. The next process steps to be performed are to remove all the overgrowth material using mechanical polishing, and to analyse the crystalline structure of the grown material. Unfortunately, we were not able to finalize these steps before the end of my PhD but it will be done later. Overall, this is the first promising demonstration of the validity of the concept to grow III-V material on Si substrates using TASE-HVPE.

II.5 Conclusion

In this chapter, we studied the growth of self-assembled InAs NWs on bare Si(111) and the selective are growth of vertically aligned InAs and GaAs NWs on patterned GaAs(111)B and Si(111) substrates. The goal of this study was to determine the different mechanisms involved during growth and also understand the effect of the growth parameters on the crystal morphology. We were able to demonstrate for the first time the growth by HVPE of catalyst-free InAs and GaAs NWs on GaAs(111)B and Si(111) substrates. We showed that a preparation of the Si(111) surface under As_4 is necessary before growth to ensure the vertical growth of the NWs and to increase the nucleation density. The study of self-assembled InAs NWs on Si(111), enables to develop a kinetic modelling based on fundamental kinetic of surface processes specific to HVPE. At low temperature, the growth is limited by the decomposition of adsorbed precursors, e.g., dechlorination of the InCl species. As the temperature increases, the growth rate increases due to thermal activation of the dechlorination step. At high temperatures, the adsorption/desorption ratio of growth precursors drastically decreases, leading to the drop of the axial growth rate. Structural characterizations showed the presence of many stacking-faults in InAs NWs, resulting in both cubic and hexagonal crystal phases. The presence of both phases is due to the surface reconstruction of the (111)B surface which strongly depends on the growth temperature and the As_4 partial pressure.

The optimized growth process has been applied to selective area growth of InAs on GaAs(111)B and Si(111) substrates. This study was part of the collaboration with Professor Ray LaPierre with the aim to demonstrate the multi-spectral absorbance of InAs NWs arrays. We have shown that the morphology of the grown material depends on the growth conditions and the size of the apertures. The morphology versus growth conditions was described by considering the kinetics of the growth mechanisms developed for self-assembled InAs NWs. The PL spectra measured at low temperature confirmed the presence of both ZB and wurtzite structures which were observed on self-assembled InAs NWs. The FTIR measurements showed that the NW arrays exhibited strong optical absorption, which was varied from 0.4 eV to 0.8 eV by tuning the NWs diameters. These results are in accordance with the theoretical models developed by Pr Ray LaPierre which is encouraging for the development of multi-spectral photo-detectors.

The growth mechanisms were identified and the control of the shape of the NWs as a function of the experimental growth parameters and mask pattern was discussed. The nanowire morphology is promoted at smaller aperture diameter. Larger apertures result in the formation of regularly arrays of GaAs micro-platelets with a pure ZB crystalline quality free of defects. As for InAs, due to surface reconstruction, GaAs NWs exhibit twins, however the density is lower due to the higher growth temperature and the larger diameter of the structures. Finally, I demonstrated the feasibility of combining TASE with HVPE, highlighting the potential of TASE-HVPE for the fabrication of III-V materials on Si wafers.

As a conclusion, we may consider that the results presented in this chapter are sufficiently encouraging to develop optoelectronics devices based on HVPE grown InAs and GaAs materials.

Chapter III

Growth of $In_xGa_{(1-x)}As$ nanowires

III.1 Introduction

In the previous chapter, I have demonstrated the growth of InAs NWs arrays capable of absorbing light at different wavelengths by tuning the NWs diameter. A different way to modify the maximum absorbance wavelength is to grow ternary material and then change its composition. In fact, a change in the material composition results in a variation of the band-gap energy. When growing ternary alloys, it is essential to control the composition homogeneity in the NW and between each NWs. In this chapter, I present preliminary results of InGaAs growth by HVPE on GaAs(111)B and Si(111). The different steps to achieve InGaAs NWs growth are presented. The effect of growth temperature and III-Cl partial pressures on the crystal morphology and gallium concentration are briefly discussed. The composition of the NWs and the homogeneity are investigated by EDX. A theoretical model based on thermodynamic and kinetic considerations is developed, to link the composition of the vapor phase and the growth temperature to the composition of the solid.

III.2 InGaAs NWs growth: effect of the growth parameters

In chapter 2, I have demonstrated the growth of both InAs and GaAs NWs. Growth conditions giving high axial growth rate have been found. These results were encouraging for the growth of ternary InGaAs NWs. The growth of InGaAs 2D layers by HVPE has already been demonstrated in our laboratory by E. Gil [81]. That is why, I decided to investigate the growth of ternary InGaAs NWs by HVPE. First, it is important to note that the growth of GaAs using As_4 and GaCl precursors is much more favorable than InAs. In fact, as shown in figure III.1, the equilibrium constant of GaAs is much more higher than that of InAs.

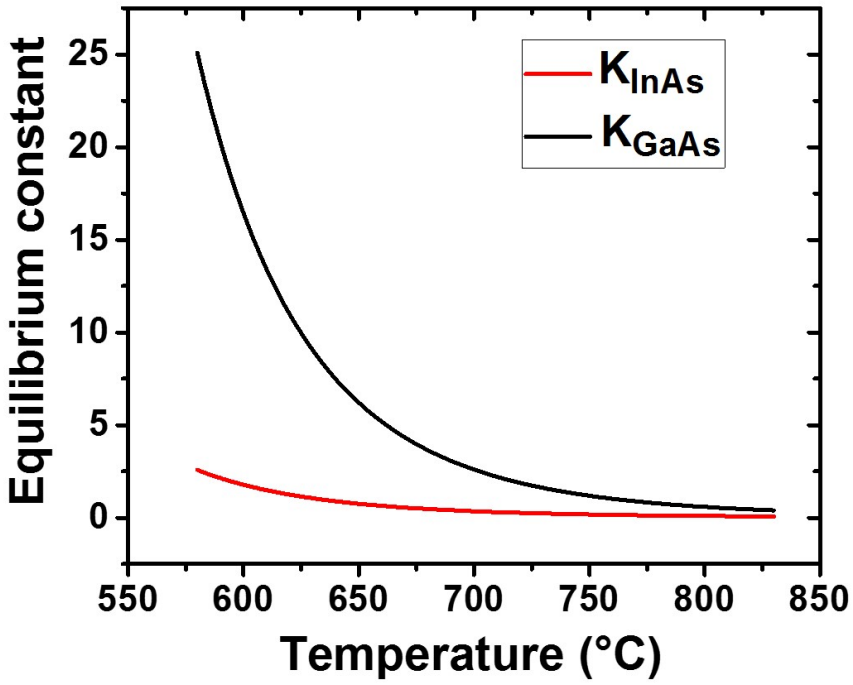

Figure III.1: Evolution of the equilibrium constants related to InAs and GaAs condensation from III-Cl and As_4 molecules as a function of temperature. Note that K are calculated here as (solid/gaseous species).

At 680 °C, we can see that K_{InAs} is 7 times lower thant K_{GaAs}. It implies that the InCl partial pressure (P_{InCl}) has to be high compared to GaCl partial pressure (P_{GaCl}) in order to incorporate indium in the material. This has already been demonstrated by HVPE with the growth at 650 °C of InGaAs layers with an In concentration of 50% for P_{InCl}/P_{GaCl} ratio $\simeq$ 15.

A convenient way to start this study was to employ growth conditions used for InAs or GaAs NWs growth and then add a little amount of the other III precursors. The growth of InGaAs was first carried on GaAs(111)B substrates, patterned with a SiO_2 dielectric mask and Si(111) substrates patterned with SiNx. The substrates were stabilized under As_4 during the heating phase. The growth starts when InCl and GaCl fluxes are turned-on simultaneously. At the end of the growth both InCl

and GaCl are turned-off simultaneously. The substrates are then cooled down under As_4 atmosphere until the temperature reaches 560 °C. The first step is to find growth conditions which enable the growth of InGaAs NWs, no matter the Ga composition. To this end I have decided to start with growth conditions giving high aspect ratio InAs NWs; i.e, a high growth temperature ($\geq$ 680 °C). Figure III.2 shows InGaAs material grown at (a) 680 °C and (b) 715 °C. The As_4 partial pressure (P_{As_4}) is 7.5×10^{-4} atm, P_{GaCl} is 6.7×10^{-4} atm, and P_{InCl} is 1×10^{-2} atm. The partial pressures used here correspond to a III_{In}/III_{Ga} ratio of 15. At 680 °C we can see that polycrystalline structures are grown, while at 715 °C NWs are grown.

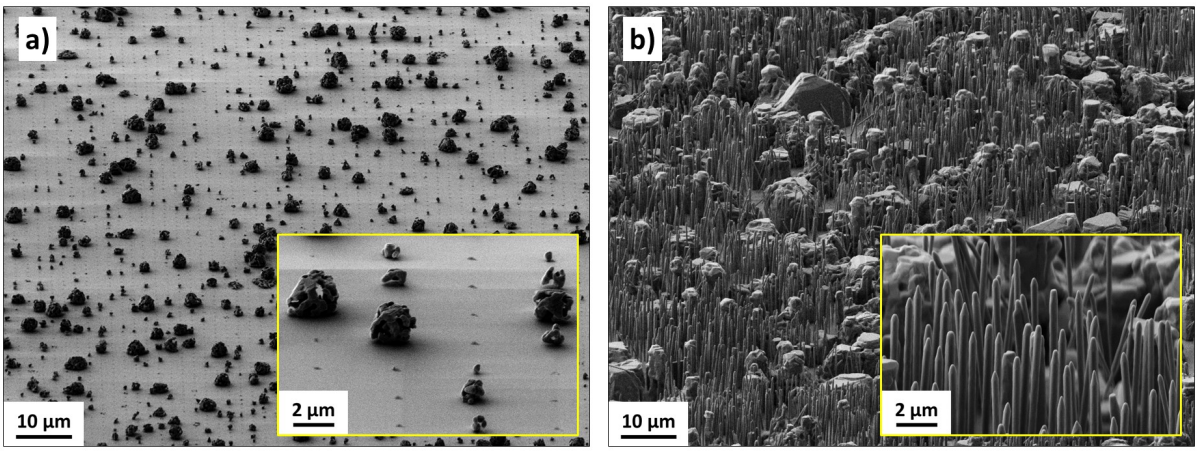

Figure III.2: Tilted-view SEM images of InGaAs material grown on GaAs(111)B substrate patterned with SiO_2 dielectric mask. The growth temperature is, a) 680 °C and, b) 715 °C . Insets show magnified views of the grown material. Diameter is 60 nm and pitch is 2 µm.

We have shown in Chapter 2 that the axial growth rate of InAs NWs is maximum at 680 °C due to the high dechlorination of AsInCl molecules. Here, the absence of NWs on figure III.2-(a) can be attributed to the very low growth rate of GaAs crystal along the (111)B direction at 680 °C. This observation is consistent with the results of chapter 2, in which we have shown that GaAs axial growth rate is significant at growth temperature above 740 °C for GaCl partial pressure of 1.6×10^{-3} atm. Here we assume that the surface is blocked with AsGaCl molecules which hinders the growth of both binaries InAs and GaAs in the ternary InGaAs crystal. By increasing the temperature to 715 °C, the axial growth rate is drastically increased, resulting in NWs with a length of 10 µm and a diameter of 350 nm. This increase of the axial growth rate is attributed to the higher dechlorination of AsGaCl molecules. InGaAs NWs growth was also observed on Si(111) patterned substrate. Even if the density is low, it enables a first investigation of the Ga composition by EDX on the as-grown NWs. SEM images of InGaAs NWs grown on patterned Si(111) and EDX spectra are shown in Figure III.3.

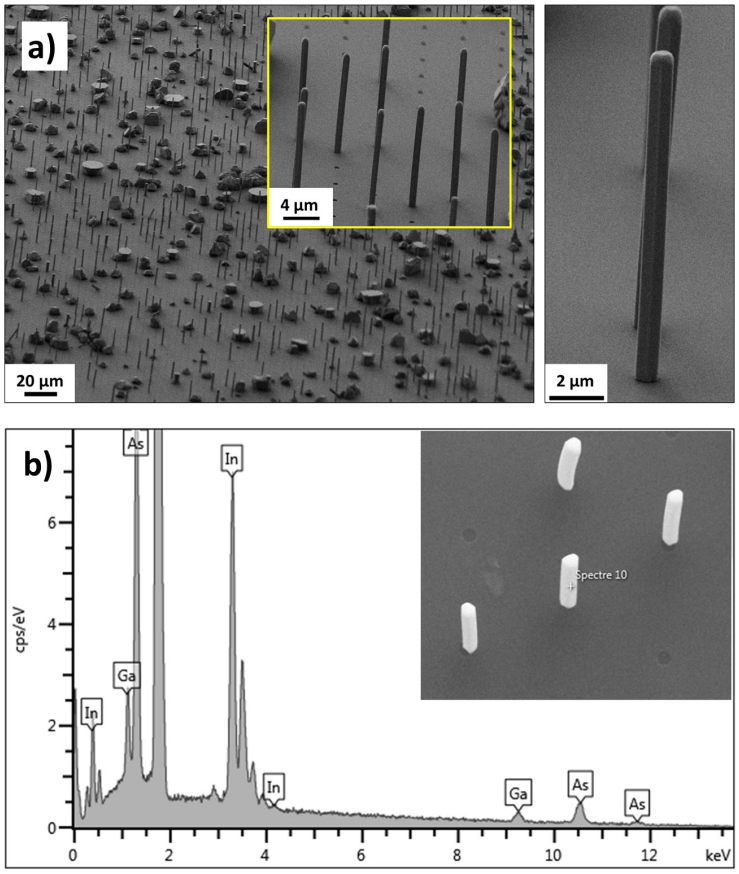

Figure III.3: a) shows tilted-view SEM images of InGaAs grown on Si(111) substrate patterned with SiN_x dielectric mask. Diameter is 350 nm and the pitch is 3.5 µm. b) is an EDX spectra of InGaAs NWs, showing a gallium concentration of 15%.

Compared to InGaAs NWs on GaAs(111)B substrate, the density of NWs observed on Figure III.3-(a) is very low. As we showed for InAs and GaAs growth on Si(111), the substrate surface and the growth conditions (temperature and precursor partial pressures) are critical for the nucleation density. Here, the NWs have clearly a uniform diameter with a hexagonal shape delimited by six equivalent $\{1-10\}$ side facets and a (111)B facet at the top. It demonstrates that the growth conditions are suitable for NW growth but the nucleation step on Si(111) must be optimised. Concerning the composition, the EDX spectra shown on figure III.3-(b) shows In and Ga peaks. It proves the presence of both metal elements in the NWs with a Ga concentration of 15%.

The relatively low diameter of the InGaAs NWs grown on GaAs(111)B, shown on figure III.2-(b), enables a first analysis of their crystalline quality by HRTEM. HRTEM images of InGaAs NWs are shown on figure III.4.

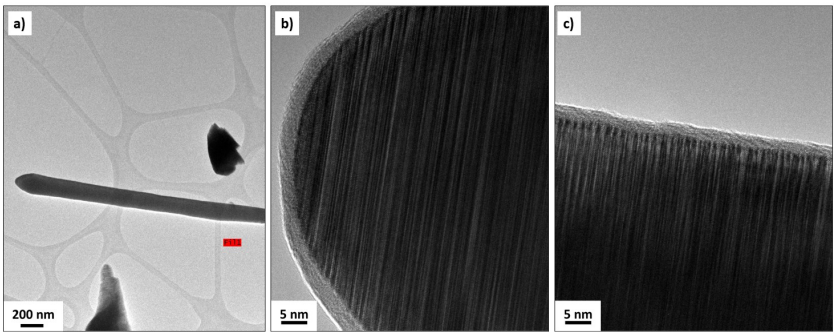

Figure III.4: HRTEM images of InGaAs NWs, with a Ga concentration of 15%, grown at 715 °C. b) and c) correspond to the top and bottom part respectively.

As for InAs NWs grown at high temperature, we can observe that NWs grow with a high density of stacking faults and twins. It is reasonnable to assume that the same (111)B surface reconstruction as InAs occurs [87]. Moreover, it has been shown by Koblmuller et al. [113], that the the density of stacking fault varies with the composition. Then it would be interesting to compare the crystalline quality of InGaAs NWs with higher Ga concentration which will be done in a forthcoming study. With the will to increase the Ga concentration, I decided to explore the growth of InGaAs at higher P_{GaCl}. InGaAs NWs grown at 715 °C under different P_{GaCl} are shown in figure III.5. We can see that the axial growth rate decreases (from 60 to 15 µm/h) when P_{GaCl} increases while the radial growth rate increases (from 1 to 2.6 µm/h)).

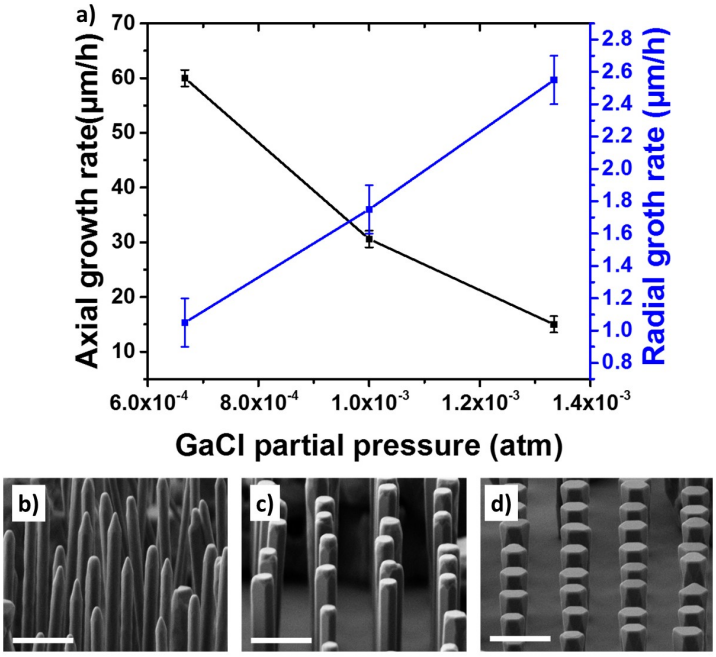

Figure III.5: (a) InGaAs NWs axial and radial growth rates as a function of P_{GaCl}. Tilted-view SEM images of InGaAs NWs grown on GaAs(111)B substrate at different P_{GaCl}: (b) P_{GaCl}=6.6×10^{-4} atm, (c) P_{GaCl}=1.0×10^{-3} atm and (d) P_{GaCl}=1.3×10^{-3} atm. Diameter is 60 nm and pitch is 2 µm. Scales bars are 2 µm.

We have previously shown that the axial growth rate was limited by the dechlorination of AsGaCl molecules. Here, the decrease of the axial growth rate with increasing P_{GaCl} shows that the growth is also limited by the dechlorination of AsGaCl molecules. This is further confirmed by the growth at $P_{GaCl}=1.6\times10^{-3}$ atm (Table III.1-(c), p.88) which shows polycrystalline structures similar to figure III.2-(a). Concerning the radial growth rate, its increase with P_{GaCl} shows that the growth is not limited by the dechlorination of AsGaCl molecules but rather by the adsorption/desorption of species. This behavior was confirmed by Hollan et al. [114] who observed growth rate up to 80 µm/h when increasing the precursors partial pressures and decreasing the growth temperature. This short study at 715 °C highlights the large effect of P_{GaCl} on the NWs morphology and it is reasonable to conclude that this morphology change is associated to a variation in the Ga concentration.

In order to access the gallium concentration along the length of the InGaAs NWs, the chemical composition of individual NWs was characterized by EDS. The EDS experiments were carried out by Catherine Bougerol at the Institut Néel in the framework of the ENNORA project (research project financed by region AURA). Figures III.6-(a), (b) and c) show the EDS profiles along the (111)B growth axis of the NWs, corresponding to figures III.5-(b), (c) and (d) respectively. Figure III.6-(d) is an EDS transverse profile corresponding to NWs of figure III.5-(d).

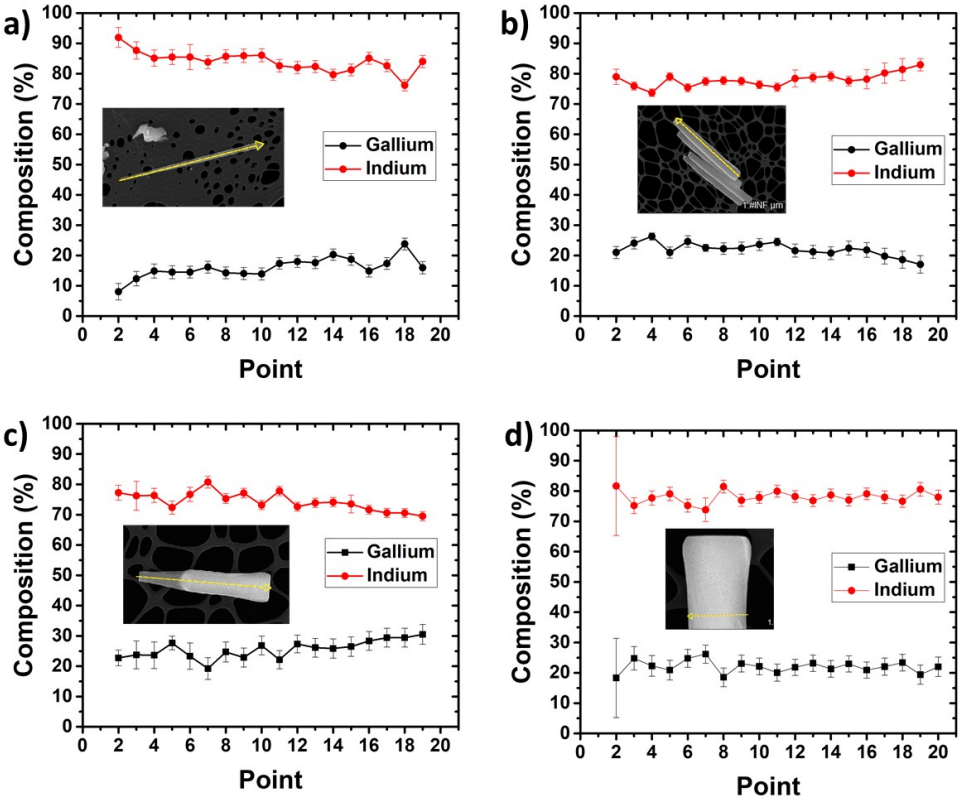

Figure III.6: EDS profiles along the (111)B direction of InGaAs NWs grown under different P_{GaCl}: (a) $P_{GaCl}=6.6\times10^{-4}$ atm, (b) $P_{GaCl}=1.0\times10^{-3}$ atm and (c) $P_{GaCl}=1.3\times10^{-3}$ atm. d) is the radial EDS profile corresponding to NW c). The insets show SEM images of NWs deposited on a carbon grid.

First, concerning the composition homogeneity along the NWs, we can see that the Ga concentration is constant all along the NWs. Compared to MOVPE and MBE, for whom the composition can vary along the NW due to the diffusion length difference between In and Ga atoms, in HVPE, the diffusion of In and Ga atoms is negligible. Then it is possible to significantly improve the homogeneity of the composition during InGaAs NWs growth. Moreover, in the case of catalysed growth, it was shown that a In-rich shell may form due to the high diffusion of In on the sidewalls. In this work, we can see in figure III.6-(d) that the radial composition is constant, confirming that there is no significant contribution of the diffusion. This homogeneity of the composition along the length and the diameter of the NWs also indicates that InGaAs NWs growth occurs through the VS mode. Finally, one can see that the Ga concentration tends to be lower at the bottom and higher at the top of the NWs. This is due to transient regimes at the beginning and end of the growth. This issue can easily be fixed by optimizing the arrival and evacuation of InCl and GaCl species.

Concerning the evolution of the Ga concentration with P_{GaCl}, we see that the gallium concentration increases from 15% to 25% when P_{GaCl} is increased from 6.6×10^{-4} atm to 1×10^{-3} atm. This increase of the Ga concentration is easily explained by the larger GaCl adsorption on the surface when we increase P_{GaCl}. Surprisingly, by further increase P_{GaCl} to 1.33×10^{-3} atm, the Ga concentration does not increase while the morphology significantly changes. Moreover, as I have shown in table III.1-(c), at P_{GaCl}=1.6×10^{-3} atm, the Ga concentration is increased to 65% but the grown material is polycrystalline and of poor quality. It is well known that strain has an impact on the composition during growth. In fact, E. Gil [81] showed that strain has to be considered to fit the InGaAs composition they observed. The author shows that strain changes the activity coefficients of InAs and GaAs binaries in the ternary alloy which in turn changes the alloy composition. In 2011, Shin et al [64] have demonstrated the catalyst-free growth of InGaAs NWs on Si(111). In this study, bending of the InGaAs NWs is clearly shown and is associated to inhomogeneous strain and composition distribution along the NWs (i.e, phase separation). The latter has been observed by X-ray diffraction (XRD) characterization. The XRD spectra of the InGaAs NWs exhibit two peaks convoluted into a large peak with a clear shoulder either on the Ga or In rich side [64]. In our case, looking back to figure III.3-(b), we can observe a bowing of some NWs which might indicate the presence of strain and/or composition variation. Of course, these hypothesis have to confirmed by further growth experiments and characterizations. These experiments will be performed in a future work.

The different growth conditions presented here correspond to InGaAs material grown under InAs growth conditions to which I have added GaCl. In figure III.7, I show InGaAs material grown on Si(111) substrates patterned with SiNx dielectric mask using GaAs growth conditions; i.e, the growth temperature is 742 °C, P_{GaCl} is 1.6×10^{-3} atm and P_{As_4} is 7.5×10^{-4} atm. P_{InCl} is 1.6×10^{-3} atm and 3.2×10^{-3} atm for figures (a) and (b), respectively. The composition measured by EDS are $\sim 4\%$ and $\sim 8\%$ for figures (a) and (b), respectively.

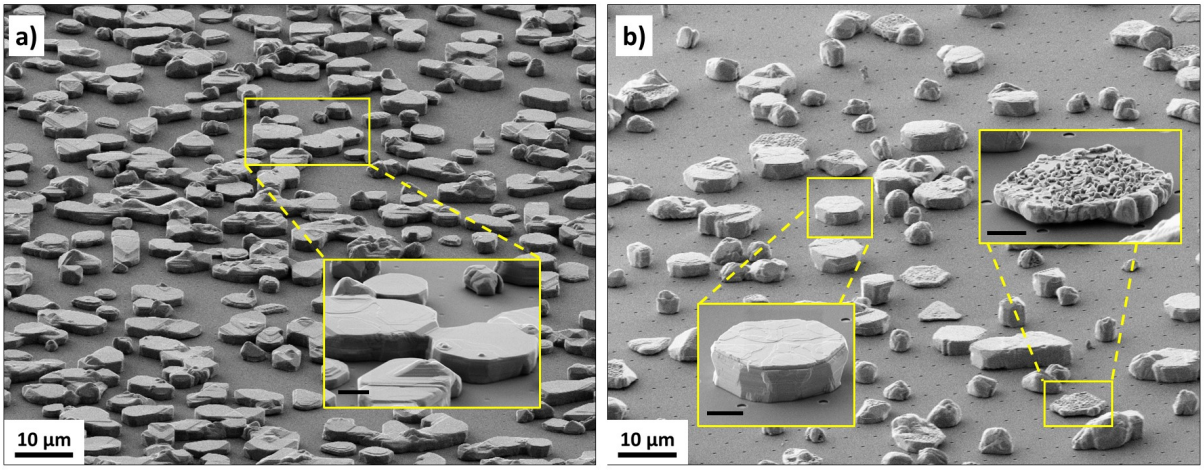

Figure III.7: Tilted-view SEM images of InGaAs material grown at 742 °C at different P_{InCl}: a) P_{InCl}=1.6×10^{-3} atm and b) P_{InCl}=3.2×10^{-3} atm. The diameter is 350 nm and pitch is 2.5 µm.

We can observe, on both figures III.7-(a) and (b), that the crystals have a low axial growth rate and a high radial growth rate leading to the growth of large structures similar to GaAs platelets obtained at 742 °C. As for In-rich InGaAs, the density is low and can be increased by optimizing the nucleation step; i.e, substrate surface and gas phase composition. However, some structures exhibit hexagonal shape indicating that they have grown epitaxially on the substrate which is very encouraging for the direct epitaxy of InGaAs on silicon by HVPE. Concerning the composition, we see that by increasing P_{InCl}, indium concentration in the solid increases from $\sim 4\%$ to $\sim 8\%$. This is simply explained by an increase of InCl adsorption on the surface resulting in higher In incorporation in the solid. At such temperature, the increase of the indium concentration leads to decomposition of the grown material due to the weak In-As bond (see inset of figure III.7-(b)). Then the more there are InAs bonds in the solid, the more decomposition occurs.

A summary of the results obtained during the InGaAs study are reported in Table III.1, as a function of the growth temperature and the InCl/GaCl ratio.

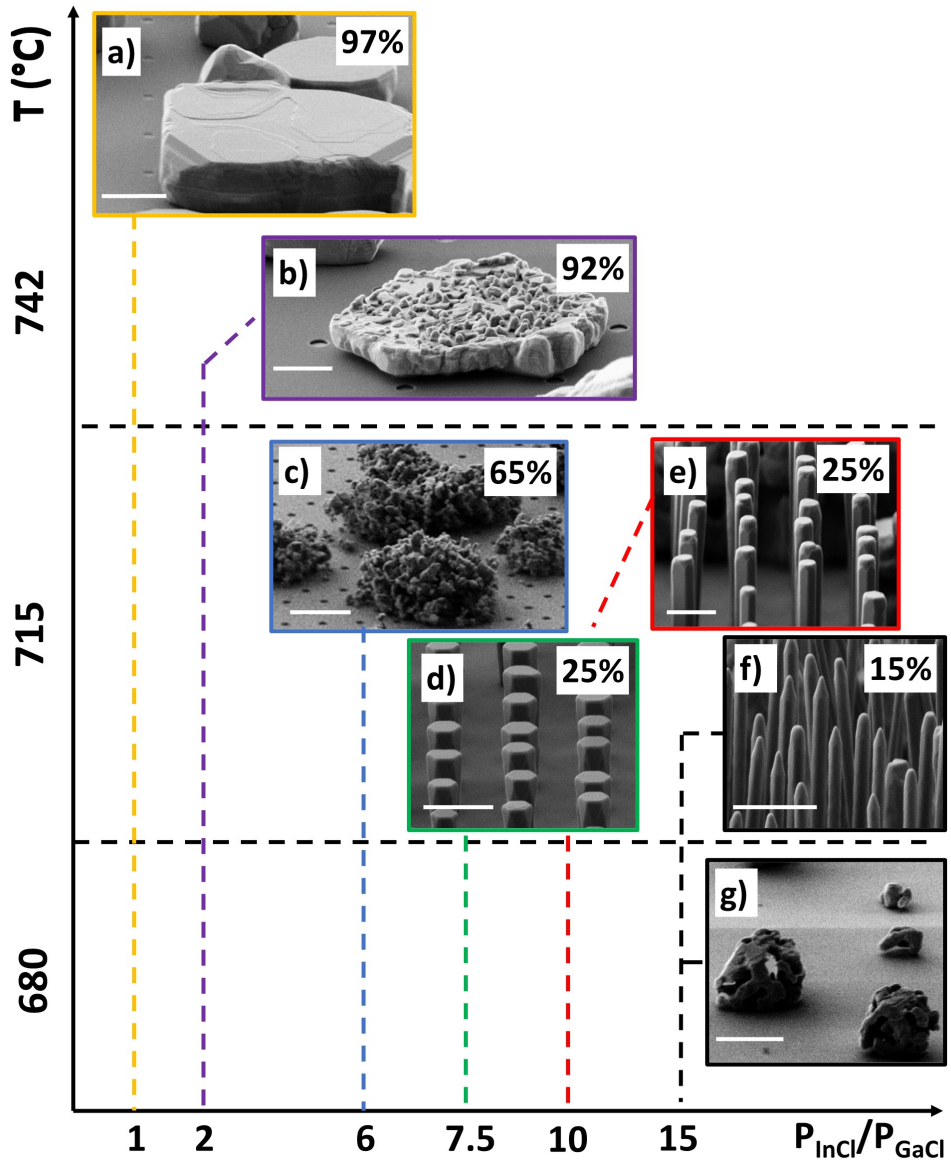

Table III.1: Experimental cartography displaying the influence of parameters (T (°C) and InCl/GaCl ratio) on the growth of InGaAs material. The gallium concentration in % is shown on each SEM image. Scale bars are 2 µm.

This table highlights the two key parameters: the growth temperature and the InCl/GaCl ratio. They have to be carefully set-up to keep a good morphology while changing the composition. At high temperature, an increase of the indium concentration lead to decomposition, while at lower temperature, the crystal quality is deteriorated due to an increase of the gallium concentration. Such behavior has already been observed by S. Hertengerger et al. [65, 115] who showed that an increase of the growth temperature is needed to increase the Ga concentration in the NW. Finally, the results presented in this study will be used in the next section to develop a theoretical model linking the growth parameters to the composition of the solid.

III.3 Thermodynamics and kinetics of InGaAs growth

In this section, I present preliminary results of thermodynamic and kinetic modeling of InGaAs crystal growth. The aim of this model is to predict the InGaAs composition as a function of the growth conditions; i.e, GaCl and InCl partial pressures. The composition can be determined by calculating the growth rate of each binary. To this end, it is necessary to express the adsorption flux and desorption flux using the partition functions of the activated molecules according to the Eyring theory. In this section, I will detail the calculation, already used in chapter II to determine the InAs growth rate along the (111)B direction, in order to calculate the InGaAs composition as a function of the vapor phase composition.

According to Eyring's theory, each molecule goes from the vapor phase to the solid (adsorption) and from the solid to the gas phase (desorption) by the formation of an activated complex of energy ε^* greater than the initial and final potential energies. To be adsorbed, a molecule must overcome a potential barrier of height $\varepsilon^* - \varepsilon_m$ which defines the adsorption activation energy (Figure III.8). Surface molecules oscillate in a 3D potential where they are trapped, they have a total energy ε equal to the sum of the potential energy $\varepsilon^{1/2}$ and a vibration term. To go from the crystalline state to the vapor phase, the molecules cross the potential barrier of height $\varepsilon^* - \varepsilon^{1/2}$ called desorption activation energy.

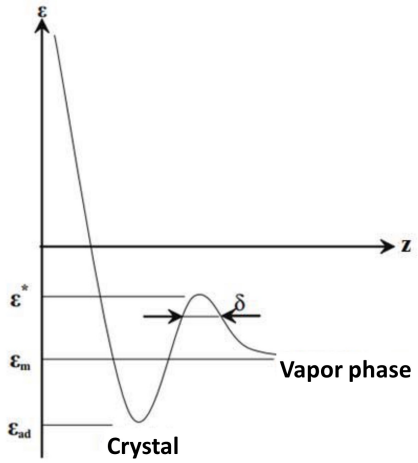

Figure III.8: Variation of molecules potential energy along the growth direction z.

The Eyring theory is applied to the limiting step which is the dechlorination of IIIAsCl molecules. The following sections are dedicated to the calculation of adsorption and desorption flux of IIICl molecules in order to express InAs and GaAs binaries growth rate in the ternary InGaAs.

III.3.1 Adsorption flux J_{+4}

Using the equality of chemical potentials of the dechlorination step:

$$AsInCl + H_{2g} \rightleftharpoons InAs_c + Cl - H - H^*$$

We have:

$$\mu_{InAs_c} + \mu_{(Cl-H-H^*)} = \mu_{AsInCl} + \mu_{H_{2g}}$$

then:

$$\frac{N^*_{Cl-H-H}}{N_v}\frac{1}{z^*_{Cl-H-H}}\frac{1}{z_{InAs_c}} = \frac{N_{AsInCl}}{N_v z_{AsInCl}}\frac{N_{H_{2g}}}{z_{H_{2g}}}$$

N_v is the number of vacant sites of the surface

N_i is the number of adsorbed molecule i,

z_i is the partition function of molecule i.

The adsorption flux J_{+4} is given by:

$$\frac{1}{S}\frac{dN^*_{(Cl-H-H)}}{dt} = \frac{1}{S}N^*_{(Cl-H-H)}\frac{\overline{v}^*}{\delta_{In}}$$

with $\overline{v}^*$ the activated molecules mean speed which overcome the potential barrier of width δ_{In}, where $\overline{v}^*$ is defined as for a 1D translation:

$$\overline{v}^* = \sqrt{\frac{k_B T}{2\pi m^*_{(Cl-H-H)}}}$$

We can write the partition function of the activated molecule isolating the 1D translation along the potential barrier:

$$z^*(In) = z^*_0(In)\delta_{In}\sqrt{\frac{2\pi m^*_{(Cl-H-H)} k_B T}{h^2}}$$

Then:

$$J_{+4} = \frac{1}{S}\frac{k_B T}{h}\frac{z^*_0(In) z_{InAs_c}}{z_{AsInCl} z_{H_{2g}}} N_{AsInCl} N_{H_{2g}} \tag{III.1}$$

We define the coverage ratio θ_i as following:

$\theta_i = \frac{N_i}{N}$ where N is the total number of surface sites. We will have: $N_s = \frac{N}{S}$, the number of sites per surface unit.

Considering the ideal gas law, J_{+4} is written:

$$J_{+4} = N_s \frac{k_B T}{h} \frac{z_0^*(In) z_{InAs_c}}{z_{AsInCl} z_{H_{2g}}} \theta_{AsInCl} \frac{P_{H_{2g}}}{\frac{k_B T}{V}} \tag{III.2}$$

The number of adsorbed InAsCl molecules is given by chemical potential equality of the reaction:

$$\frac{1}{4} As_{4g} + InCl_g \rightleftharpoons AsInCl$$

then:

$$\frac{N_{AsInCl}}{N_v z_{AsInCl}} = \frac{P_{As_{4g}}^{1/4}}{(\frac{k_B T}{V} z_{As_{4g}})^{1/4}} \frac{P_{InCl_g}}{\frac{k_B T}{V} z_{InCl_g}}$$

$$\theta_{AsInCl} = \theta_v \left[\frac{P_{As_{4g}}^{1/4}}{(\frac{k_B T}{V} z_{As_{4g}})^{1/4}} \frac{P_{InCl_g}}{\frac{k_B T}{V} z_{InCl_g}} \right] z_{AsInCl}$$

Finally:

$$J_{+4} = N_s \frac{k_B T}{h} \frac{z_0^*(In) z_{InAs_c}}{z_{InCl_g} z_{H_{2g}} z_{As_{4g}}^{1/4}} \frac{P_{H_{2g}} P_{As_{4g}}^{1/4} P_{InCl_g}}{(\frac{k_B T}{v})^{9/4}} \theta_v \tag{III.3}$$

III.3.2 Desorption flux J_{-4}

The desorption flux is calculated using the chemical potential equality of the reaction:

$$InAs_c + Cl - H - H^* \rightleftharpoons InAs + H + HCl_g$$

Based on the same calculation as for the adsorption flux J_{+4} we have:

$$J_{-4} = N_s \frac{k_B T}{h} \frac{z_0^*(In) P_{H_{2g}}^{1/2} P_{HCl_g}}{z_{H_{2g}}^{1/2} z_{HCl_g} (\frac{k_B T}{V})^{3/2}} \theta_{InAs} \tag{III.4}$$

The growth rate of the binary InAs in the ternary $In_xGa_{1-x}As$ can be written as the difference between the adsortion and desorption flux:

$$R_{InAs} = \Omega_{InAs} J_{-4} \left[\frac{J_{+4}}{J_{-4}} - 1 \right]$$

with Ω_{InAs} the volume of the InAs molecule.

Then:

$$R_{InAs} = \Omega_{InAs} J_{-4} \left[\frac{P_{H_{2g}}^{1/2} P_{As_{4g}}^{1/4} P_{InCl_g}}{P_{HCl_g}} \frac{z_{InAs_c} z_{HCl_g}}{z_{H_{2g}}^{1/2} z_{As_{4g}}^{1/4} z_{InCl_g} (\frac{k_B T}{V})} \frac{\theta_v}{\theta_{InAs}} - 1 \right]$$

If we applied a statistical treatment of the chemical potential equilibrium to the InAs condensation reaction:

$$InCl_g + \frac{1}{4} As_4 + \frac{1}{2} H_2 \rightleftharpoons InAs_c + HCl_g$$

We find the statistical expression of the equilibrium constant defined in the Chapter I. Then we can write in the alloy $In_xGa_{1-x}As$:

$$\frac{1}{x} \frac{z_{InAs_c} z_{HCl_g}}{z_{H_{2g}}^{1/2} z_{As_{4g}}^{1/4} z_{InCl_g} . (\frac{k_B T}{V})} = \frac{1}{K_{InAs}^{eq}(x,T)}$$

or:

$$\frac{z_{InAs_c} z_{HCl_g}}{z_{H_{2g}}^{1/2} z_{As_{4g}}^{1/4} z_{InCl_g} (\frac{k_B T}{V})} = \frac{1}{K_{InAs}^{eq}(T) \alpha_{InAs}}$$

Where, α_{InAs} is the activity coefficient representing the interaction of InAs with GaAs in the solid InGaAs.

Finally, the growth rate of InAs in the ternary InGaAs crystal reads:

$$R_{InAs} = \Omega_{InAs} J_{-4} \left[\frac{P_{H_{2g}}^{1/2} P_{As_{4g}}^{1/4} P_{InCl_g}}{P_{HCl_g}} \frac{1}{K_{InAs}^{eq}(T) \alpha_{InAs}} \frac{\theta_v}{\theta_{InAs}} - 1 \right] \tag{III.5}$$

In the same way, GaAs growth rate in the ternary is given by:

$$R_{GaAs} = \Omega_{GaAs} J_{-4} \left[\frac{P_{H_{2g}}^{1/2} P_{As_{4g}}^{1/4} P_{GaCl_g}}{P_{HCl_g}} \frac{1}{K_{GaAs}^{eq}(T) \alpha_{GaAs}} \frac{\theta_v}{\theta_{GaAs}} - 1 \right] \tag{III.6}$$

Moreover, we can see that we find the equation of the growth rate demonstrated in Chapter II:

$$R_{(III-As)} = \Omega_{(III-As)} \gamma_{(III-As)} J_{-4} \tag{III.7}$$

In order to determine the relation between the ratio P_{InCl}/P_{GaCl} and the composition x, we introduce the ratio R_{InAs}/R_{GaAs}. In fact, the composition x of the ternary alloy is determined by the ratio of InAs and GaAs growth rates:

$$\frac{R_{InAs}}{R_{GaAs}} = \frac{x}{1-x}$$

Then:

$$\frac{x}{1-x} = \frac{\Omega_{InAs}}{\Omega_{GaAs}} \frac{J_{-4}(InAs)}{J_{-4}(GaAs)} \left[\frac{\frac{P_{InAs}}{K^{eq}_{InAs}(T)\alpha_{InAs}} \frac{\theta_v}{\theta_{InAs}} - 1}{\frac{P_{GaAs}}{K^{eq}_{GaAs}(T)\alpha_{GaAs}} \frac{\theta_v}{\theta_{GaAs}} - 1} \right]$$

If we assume that the molecular volumes of InAs and GaAs are almost identical, then the ratio of the desorption fluxes is written:

$$\frac{J_{-4}(InAs)}{J_{-4}(GaAs)} = \frac{z^*_0(In)}{z^*_0(Ga)} \frac{\theta_{InAs}}{\theta_{GaAs}} exp\left(-\frac{(\varepsilon^*_{In} - \varepsilon^*_{Ga})}{k_B T_D} \right)$$

Using the approximation of Bragg-Williams, we have:

$$\frac{\theta_{InAs}}{\theta_{GaAs}} = \frac{x}{1-x}$$

The same approximation also gives:

$$\frac{\theta_v}{\theta_{InAs}} = \frac{1}{x} \qquad and \qquad \frac{\theta_v}{\theta_{GaAs}} = \frac{1}{1-x}$$

Moreover, if we consider that: $z^*_0(In) \simeq z^*_0(Ga)$, then we have:

$$exp\left(\frac{(\varepsilon^*_{In} - \varepsilon^*_{Ga})}{k_B T} \right) = \frac{\frac{P_{InAs}}{K^{eq}_{InAs}(T)\alpha_{InAs}} \frac{1}{x} - 1}{\frac{P_{GaAs}}{K^{eq}_{GaAs}(T)\alpha_{GaAs}} \frac{1}{1-x} - 1} \tag{III.8}$$

ε^*_{In} and ε^*_{Ga} are the dechlorination energy of AsInCl and AsGaCl molecules, respectively.

Finally we find the expression of $\gamma_{GaAs}(x,T)$ and $\gamma_{InAs}(x,T)$, and then:

$$\frac{\gamma_{InAs}(x,T_D)}{\gamma_{GaAs}(x,T_D)} = exp(\frac{\Delta\varepsilon^*}{k_B T})$$

Now we can express the partial pressure ratio P_{InCl}/P_{GaCl} as a function of the composition x:

$$\frac{P_{InCl}}{P_{GaCl}} = \frac{K^{eq}_{InAs}(x,T)}{K^{eq}_{GaAs}(x,T)} \left[exp(-\frac{\Delta\varepsilon^*}{k_B T}) + \frac{(1 - exp(-\frac{\Delta\varepsilon^*}{k_B T}))}{1 + \gamma_{InAs}(x,T)} \right] \tag{III.9}$$

$\Delta\varepsilon^*$ is determined by fitting the experimental data, $K^{eq}_{GaAs}(x,T)$ and $K^{eq}_{InAs}(x,T)$ are calculated using the thermodynamic data from [116, 117]. The fit of the experimental data presented in the previous section is shown on Figure III.9. Black and red squares correspond to InGaAs material grown at 715 °C and 742 °C respectively. Full lines are the theoretical curves.

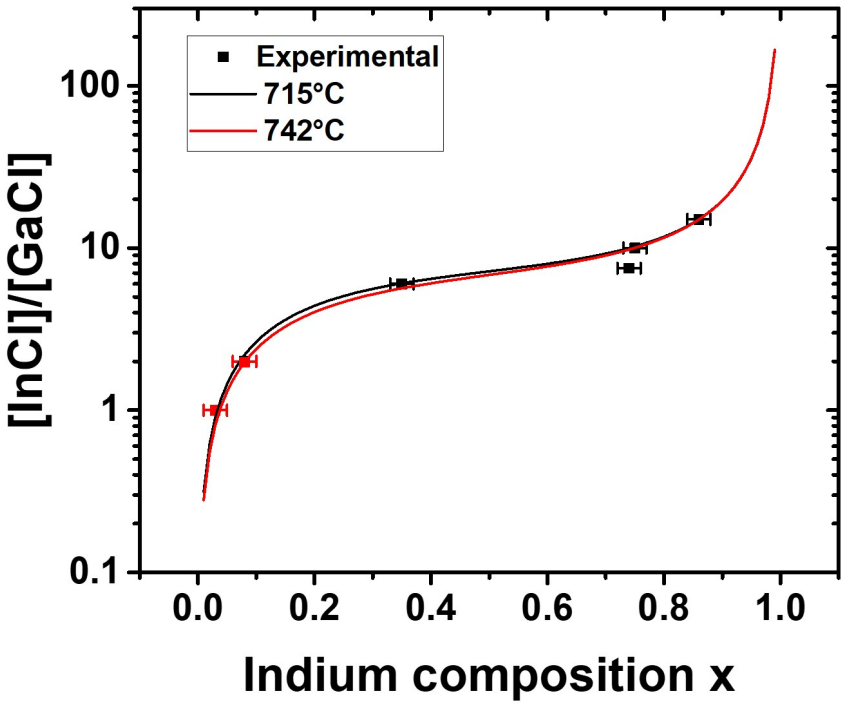

Figure III.9: Theoretical curves of the partial pressure ratio (written $[InCl]/[GaCl]$ on the axis) as a function of the indium composition (Full lines) fitting the experimental data (Squares).

We can see that the theoretical curve fits well the experimental data obtained by EDS measurements. The best fit of the experimental data is obtained for $\Delta\varepsilon^* \simeq 0$ meaning that the dechlorination energies of AsGaCl and AsInCl molecules are almost identical. This implies that the relation between the ratio P_{InCl}/P_{GaCl} and the composition x is simply given by the equation:

$$\frac{P_{InCl}}{P_{GaCl}} = \frac{K^{eq}_{InAs}(x,T_D)}{K^{eq}_{GaAs}(x,T_D)} \tag{III.10}$$

It leads us to conclude that the composition of the alloy is simply determined by thermodynamics. This finding must be confirmed by growing InGaAs NWs covering all the composition range while keeping a good crystalline quality. Finally, this theoretical modeling highlights the possibility to grow InGaAs material covering the full range of indium concentration by controlling the vapor phase composition. A semi-empirical procedure could be set-up to optimize the growth conditions and provide InGaAs NWs arrays with an accurate control of the composition.

III.4 Conclusion

In this chapter, I have investigated the growth of InGaAs NWs on GaAs(111)B substrates patterned with a SiO_2 mask and Si(111) substrates patterned with a SiNx mask. Preliminary results about the effect of the growth parameters, namely growth temperature and InCl/GaCl ratio, were presented. I demonstrated that growth on patterned GaAs substrates is well achieved while the density of NWs on Si(111) substrates is low. I also showed that growth temperature and III precursors partial pressures must be optimized in order to change the composition while keeping the NW morphology. At high temperature, an increase of the indium concentration leads to decomposition due to weak In-As bond in the crystal. At low temperature, an increase of the GaCl partial pressure results in a saturation of the surface which inhibits the axial growth. The variation of the composition with the InCl/GaCl is also investigated. The general trend observed is an increase of the Ga concentration when decreasing the InCl/GaCl ratio. However, for the shortest NWs unexpected Ga composition of 25% is measured while variation of the NWs morphology is observed, suggesting that strains might be considered. The homogeneity of the composition was investigated by EDS profile measurement along the NWs growth direction. Variation of the composition is observed at the base and the top of the NWs which can be easily fixed by optimising the start and the end of growth. This said, the composition is constant along the NWs growth axis, indicating that NWs grow following the VS growth mode. A theoretical model, based on thermodynamic and kinetic calculations has enabled the determination of the InGaAs composition as a function of the growth temperature and the InCl/GaCl ratio. The best fit of the experimental data is finally obtained when the dechlorination energy of InAsCl and InGaCl molecules are set identical, meaning that the composition is simply a function of InAs and GaAs equilibrium constants and gas partial pressures. These results are very promising for the development of InGaAs NWs epitaxy on silicon using HVPE.

General conclusion

The present thesis was devoted to the growth and characterization of III-V (In,Ga)As nanowires (NWs) using hydride vapor phase epitaxy (HVPE). The objective and novelty were to demonstrate growth of InGaAs NWs with tunable composition from InAs to GaAs and morphology.

I have first presented the potential and specifics of HVPE for the growth of III-As materials. An overview of the state-of-the-art related to the growth of InGaAs NWs by other growth techniques (MBE and MOVPE) was reported, highlighting the complex task that is VLS growth of InGaAs NWs. A thermodynamic study of the vapor phase composition at equilibrium, which includes the formation of III-Cl and the cracking of AsH3 precursors, was conducted. Supersaturation of the vapor phase was calculated to determine whether condensation of (In,Ga)-As crystal occurs or not.

Catalyst-free growth by HVPE of InAs and GaAs NWs was reported for the first time to our knowledge. Direct growth of vertically aligned InAs NWs on un-patterned Si(111) substrates was performed. The NWs grow along the (111)B direction with a constant diameter. The axial growth rate can be controlled by tuning the growth temperature and the III/V ratio. The experimental results were supported by a theoretical model based on thermodynamics and surface kinetics. It was shown that the growth occurs through condensation and is mainly limited by the kinetics of decomposition of adsorbed species at low temperature, and the thermodynamics of adsorption at high temperature. HRTEM characterization revealed the presence of both wurtzite (WZ) and zinc-blende (ZB) crystal structures in the NWs. This was attributed to the surface reconstruction of the (111)B surface at high As4 partial pressure in the HVPE environment, which is responsible for the formation of such stacking faults and polytypism.

Selective area growth (SAG) by HVPE of InAs NWs on patterned Si(111) and GaAs(111)B substrates was developed, with a focus on the control of the NWs morphology, required for multi-spectral photo-detection. We showed that in HVPE, the morphology of the grown material depends on the growth conditions and the size of the apertures. The hole diameter plays a major role. Indeed, small opening results in NWs growth while larger opening leads to multiple island nucleation which in turns results in planar growth after coalescence. The morphology versus growth conditions was described by considering the kinetics of the growth mechanisms involved in HVPE.

Optical characterizations by photoluminescence spectroscopy (PL) of InAs NWs arrays on Si and GaAs have confirmed the presence of both ZB and WZ structures. However, the NWs arrays exhibited strong PL intensity and optical absorption. Moreover, we have demonstrated that the absorption wavelength can be tuned by varying the NWs diameter. These results are encouraging for the development of multi-spectral photo-detection devices which will be performed during a forthcoming PhD in collaboration with Pr. Ray LaPierre.

We demonstrated the SAG-HVPE of GaAs NWs and platelets on GaAs(111)B and Si(111) patterned substrates. At temperature above 740 °C, well faceted NWs and platelets were grown, while polycrystalline crystals were grown at lower temperature due to multiple nucleation in the openings. As for InAs material, the crystal morphology can be tuned by changing growth conditions and pattern design. The platelets exhibited defect-free ZB structure while stacking faults were observed in the NWs. The density of stacking faults should be related to the As4 partial pressure, the growth temperature and the NWs diameter. The growth process developed to achieve direct growth of GaAs on silicon was finally applied to template assisted selective epitaxy (TASE). The successful conformal growth of planar GaAs on Si demonstrates the validity of TASE-HVPE. Both Institut Pascal and IBM Europe expect that these results are highly valuable and the collaboration will be continued to further develop this approach (a paper is under preparation).

Last part of the thesis work was dedicated to InGaAs ternary alloy growth. Growth of InGaAs was facilitated by the understanding of InAs and GaAs growth mechanisms. The growth of InGaAs NWs on patterned GaAs(111)B and Si(111) substrates using indium-rich growth conditions was performed. The NWs grew vertically on the substrates and exhibited a high aspect ratio. The density of NWs on Si(111) was low but could be increased by optimizing the initial growth conditions. Preliminary results of growth parameters effect on the NWs morphology and composition were presented. We showed that by varying the InCl/GaCl ratio, either by changing InCl or GaCl partial pressures, the composition could be tuned. At high temperature (742 °C), an increase of the indium concentration led to crystal decomposition due to weak InAs bonds. At lower temperature (715 °C), an increase of the Ga concentration (15% to 25%) yielded shorter and larger NWs and finally suppressed the NW growth due to surface blockage with GaCl molecules. EDX analyses showed a good composition homogeneity along the NWs. This preliminary study demonstrated that control of the ternary material crystal composition was reached. However, vapor phase composition and growth temperature should be accurately set to control the NWs morphology.

Theoretical model that enables the calculation of the InGaAs alloy composition as a function of the vapor phase composition and growth temperature was proposed. By considering that the dechlorination energy of AsInCl and AsGaCl molecules were identical, a good agreement was observed between the experimental results and the model. This led us to conclude that the composition of InGaAs material grown by HVPE is given by the thermodynamic equilibrium of both InAs and GaAs condensation reactions in the InGaAs alloy.

To conclude, catalyst-free growth of III-As NWs using HVPE has been successfully demonstrated. It is still at its early stage of development and requires further investigations. Therefore, this work will be continued, in the frame of a joint thesis supervised by Institut Pascal and McMaster University, with the aim to fabricate a multi-spectral photo-detector device for infrared applications.

Bibliography

[1] M. R. Ramdani, E. Gil, C. Leroux, Y. André, A. Trassoudaine, D. Castelluci, L. Bideux, G. Monier, C. Robert-Goumet, and R. Kupka, "Fast Growth Synthesis of GaAs Nanowires with Exceptional Length," *Nano Letters*, vol. 10, pp. 1836–1841, May 2010.

[2] H. Hijazi, V. G. Dubrovskii, G. Monier, E. Gil, C. Leroux, G. Avit, A. Trassoudaine, C. Bougerol, D. Castellucci, C. Robert-Goumet, and Y. André, "Influence of Silicon on the Nucleation Rate of GaAs Nanowires on Silicon Substrates," *The Journal of Physical Chemistry C*, vol. 122, pp. 19230–19235, Aug. 2018.

[3] Z. Dong, Y. André, V. G. Dubrovskii, C. Bougerol, C. Leroux, M. R. Ramdani, G. Monier, A. Trassoudaine, D. Castelluci, and E. Gil, "Self-catalyzed GaAs nanowires on silicon by hydride vapor phase epitaxy," *Nanotechnology*, vol. 28, p. 125602, Feb. 2017.

[4] M. Zeghouane, G. Avit, Y. André, C. Bougerol, Y. Robin, P. Ferret, D. Castelluci, E. Gil, V. G. Dubrovskii, H. Amano, and A. Trassoudaine, "Compositional control of homogeneous InGaN nanowires with the In content up to 90%," *Nanotechnology*, vol. 30, p. 044001, Nov. 2018. Publisher: IOP Publishing.

[5] E. Ertekin, P. A. Greaney, D. C. Chrzan, and T. D. Sands, "Equilibrium limits of coherency in strained nanowire heterostructures," *Journal of Applied Physics*, vol. 97, p. 114325, June 2005.

[6] S. Raychaudhuri and E. T. Yu, "Critical dimensions in coherently strained coaxial nanowire heterostructures," *Journal of Applied Physics*, vol. 99, p. 114308, June 2006.

[7] D. V. Beznasyuk, *Axial GaAs/InAs nanowire heterostructures for photonic applications on Si*. phdthesis, Université Grenoble Alpes, Sept. 2018.

[8] F. Glas, "Critical dimensions for the plastic relaxation of strained axial heterostructures in free-standing nanowires," *Physical Review B*, vol. 74, p. 121302, Sept. 2006.

[9] K. Tomioka, Y. Kobayashi, J. Motohisa, S. Hara, and T. Fukui, "Selective-area growth of vertically aligned GaAs and GaAs/AlGaAs core–shell nanowires on Si(111) substrate," *Nanotechnology*, vol. 20, p. 145302, Apr. 2009.

[10] X. Ji, X. Yang, W. Du, H. Pan, and T. Yang, "Selective-Area MOCVD Growth and Carrier-Transport-Type Control of InAs(Sb)/GaSb Core–Shell Nanowires," *Nano Letters*, vol. 16, pp. 7580–7587, Dec. 2016.

[11] H. Kim, W.-J. Lee, A. C. Farrell, J. S. D. Morales, P. Senanayake, S. V. Prikhodko, T. J. Ochalski, and D. L. Huffaker, "Monolithic InGaAs Nanowire Array Lasers on Silicon-on-Insulator Operating at Room Temperature," *Nano Letters*, vol. 17, pp. 3465–3470, June 2017.

[12] P. Krogstrup, H. I. Jørgensen, M. Heiss, O. Demichel, J. V. Holm, M. Aagesen, J. Nygard, and A. Fontcuberta i Morral, "Single-nanowire solar cells beyond the Shockley–Queisser limit," *Nature Photonics*, vol. 7, pp. 306–310, Apr. 2013.

[13] R. S. Wagner and W. C. Ellis, "Vapor-liquid-solid mechanism of single crystal growth," *Applied Physics Letters*, vol. 4, pp. 89–90, Mar. 1964.

[14] V. G. Dubrovskii, "Group V sensitive vapor–liquid–solid growth of Au-catalyzed and self-catalyzed III–V nanowires," *Journal of Crystal Growth*, vol. 440, pp. 62–68, Apr. 2016.

[15] S. Breuer, C. Pfüller, T. Flissikowski, O. Brandt, H. T. Grahn, L. Geelhaar, and H. Riechert, "Suitability of Au- and Self-Assisted GaAs Nanowires for Optoelectronic Applications," *Nano Letters*, vol. 11, pp. 1276–1279, Mar. 2011.

[16] M. Bar-Sadan, J. Barthel, H. Shtrikman, and L. Houben, "Direct Imaging of Single Au Atoms Within GaAs Nanowires," *Nano Letters*, vol. 12, pp. 2352–2356, May 2012.

[17] C. Colombo, D. Spirkoska, M. Frimmer, G. Abstreiter, and A. Fontcuberta i Morral, "Ga-assisted catalyst-free growth mechanism of GaAs nanowires by molecular beam epitaxy," *Physical Review B*, vol. 77, Apr. 2008.

[18] F. Jabeen, V. Grillo, S. Rubini, and F. Martelli, "Self-catalyzed growth of GaAs nanowires on cleaved Si by molecular beam epitaxy," *Nanotechnology*, vol. 19, p. 275711, May 2008. Publisher: IOP Publishing.

[19] F. Matteini, G. Tütüncüoglu, H. Potts, F. Jabeen, and A. Fontcuberta i Morral, "Wetting of Ga on SiOx and Its Impact on GaAs Nanowire Growth," *Crystal Growth & Design*, vol. 15, pp. 3105–3109, July 2015.

[20] X. Wang, X. Yang, W. Du, H. Ji, S. Luo, and T. Yang, "Thickness influence of thermal oxide layers on the formation of self-catalyzed InAs nanowires on Si(111) by MOCVD," *Journal of Crystal Growth*, vol. 395, pp. 55–60, June 2014.

[21] T. Grap, T. Rieger, C. Blömers, T. Schäpers, D. Grützmacher, and M. I. Lepsa, "Self-catalyzed VLS grown InAs nanowires with twinning superlattices," *Nanotechnology*, vol. 24, p. 335601, Aug. 2013.

[22] M. Madsen, M. Aagesen, P. Krogstrup, C. Sørensen, and J. Nygård, "Influence of the oxide layer for growth of self-assisted InAs nanowires on Si(111)," *Nanoscale Research Letters*, vol. 6, no. 1, p. 516, 2011.

[23] D. S. Dhungana, A. Hemeryck, N. Sartori, P.-F. Fazzini, F. Cristiano, and S. R. Plissard, "Insight of surface treatments for CMOS compatibility of InAs nanowires," *Nano Research*, vol. 12, pp. 581–586, Mar. 2019.

[24] S. K. Jangir, H. K. Malik, A. Kumar, D. V. Sridhar Rao, R. Muralidharan, and P. Mishra, "Influence of Molecular Beam Epitaxy (MBE) Parameters on Catalyst-Free Growth of InAs Nanowires on Silicon (111) Substrate," *Journal of Electronic Materials*, Feb. 2019.

[25] K. Tomioka, P. Mohan, J. Noborisaka, S. Hara, J. Motohisa, and T. Fukui, "Growth of highly uniform InAs nanowire arrays by selective-area MOVPE," *Journal of Crystal Growth*, vol. 298, pp. 644–647, Jan. 2007.

[26] M. T. Björk, H. Schmid, C. M. Breslin, L. Gignac, and H. Riel, "InAs nanowire growth on oxide-masked <111> silicon," *Journal of Crystal Growth*, vol. 344, pp. 31–37, Apr. 2012.

[27] B. Mandl, A. W. Dey, J. Stangl, M. Cantoro, L.-E. Wernersson, G. Bauer, L. Samuelson, K. Deppert, and C. Thelander, "Self-seeded, position-controlled InAs nanowire growth on Si: A growth parameter study," *Journal of Crystal Growth*, vol. 334, pp. 51–56, Nov. 2011.

[28] H. Paetzelt, V. Gottschalch, J. Bauer, G. Benndorf, and G. Wagner, "Selective-area growth of GaAs and InAs nanowires—homo- and heteroepitaxy using SiNx templates," *Journal of Crystal Growth*, vol. 310, pp. 5093–5097, Nov. 2008.

[29] S. Hertenberger, D. Rudolph, M. Bichler, J. J. Finley, G. Abstreiter, and G. Koblmüller, "Growth kinetics in position-controlled and catalyst-free InAs nanowire arrays on Si(111) grown by selective area molecular beam epitaxy," *Journal of Applied Physics*, vol. 108, p. 114316, Dec. 2010.

[30] H. Hijazi, *HVPE-Grown GaAs Nanowires : Growth Modeling, Passivation and Transport Properties*. phdthesis, Université Clermont Auvergne, Oct. 2019.

[31] C.-Y. Yeh, Z. W. Lu, S. Froyen, and A. Zunger, "Zinc-blende–wurtzite polytypism in semiconductors," *Physical Review B*, vol. 46, pp. 10086–10097, Oct. 1992.

[32] H. J. Joyce, Q. Gao, J. Wong-Leung, Y. Kim, H. H. Tan, and C. Jagadish, "Tailoring GaAs, InAs, and InGaAs Nanowires for Optoelectronic Device Applications," *IEEE Journal of Selected Topics in Quantum Electronics*, vol. 17, pp. 766–778, July 2011.

[33] K. A. Dick, K. Deppert, L. Samuelson, and W. Seifert, "Optimization of Au-assisted InAs nanowires grown by MOVPE," *Journal of Crystal Growth*, vol. 297, pp. 326–333, Dec. 2006.

[34] V. G. Dubrovskii, N. V. Sibirev, J. C. Harmand, and F. Glas, "Growth kinetics and crystal structure of semiconductor nanowires," *Physical Review B*, vol. 78, Dec. 2008.

[35] J. C. Harmand, M. Tchernycheva, G. Patriarche, L. Travers, F. Glas, and G. Cirlin, "GaAs nanowires formed by Au-assisted molecular beam epitaxy: Effect of growth temperature," *Journal of Crystal Growth*, vol. 301-302, pp. 853–856, Apr. 2007.

[36] K. A. Dick, K. Deppert, T. Mårtensson, B. Mandl, L. Samuelson, and W. Seifert, "Failure of the vapor-liquid-solid mechanism in Au-assisted MOVPE growth of InAs nanowires," *Nano Letters*, vol. 5, pp. 761–764, Apr. 2005.

[37] Z. Zhang, Z.-Y. Lu, P.-P. Chen, W. Lu, and J. Zou, "Defect-free zinc-blende structured InAs nanowires realized by in situ two V/III ratio growth in molecular beam epitaxy," *Nanoscale*, vol. 7, pp. 12592–12597, July 2015.

[38] M. Tchernycheva, L. Travers, G. Patriarche, F. Glas, J.-C. Harmand, G. E. Cirlin, and V. G. Dubrovskii, "Au-assisted molecular beam epitaxy of InAs nanowires: Growth and theoretical analysis," *Journal of Applied Physics*, vol. 102, p. 094313, Nov. 2007.

[39] W. M. Haynes, *CRC Handbook of Chemistry and Physics*. CRC Press, June 2014.

[40] C. Chatillon and D. Chatain, "Congruent vaporization of GaAs(s) and stability of Ga(l) droplets at the GaAs(s) surface," *Journal of Crystal Growth*, vol. 151, pp. 91–101, May 1995.

[41] E. A. Anyebe, Q. Zhuang, A. M. Sanchez, S. Lawson, A. J. Robson, L. Ponomarenko, A. Zhukov, and O. Kolosov, "Self-catalysed growth of InAs nanowires on bare Si substrates by droplet epitaxy," *physica status solidi (RRL) – Rapid Research Letters*, vol. 8, no. 7, pp. 658–662, 2014. _eprint: https://onlinelibrary.wiley.com/doi/pdf/10.1002/pssr.201409106.

[42] U. P. Gomes, D. Ercolani, V. Zannier, J. David, M. Gemmi, F. Beltram, and L. Sorba, "Nucleation and growth mechanism of self-catalyzed InAs nanowires on silicon," *Nanotechnology*, vol. 27, no. 25, p. 255601, 2016.

[43] W. Yang, X. Ji, X. Wang, T. Li, T. Shi, T. Yang, and Q. Chen, "The effect of nanoscale steps on the self-catalyzed position-controlled InAs nanowire growth," *Journal of Micromechanics and Microengineering*, vol. 28, no. 1, p. 014002, 2018.

[44] B. Mandl, J. Stangl, E. Hilner, A. A. Zakharov, K. Hillerich, A. W. Dey, L. Samuelson, G. Bauer, K. Deppert, and A. Mikkelsen, "Growth Mechanism of Self-Catalyzed Group IIIV Nanowires," *Nano Letters*, vol. 10, pp. 4443–4449, Nov. 2010.

[45] U. P. Gomes, D. Ercolani, N. V. Sibirev, M. Gemmi, V. G. Dubrovskii, F. Beltram, and L. Sorba, "Catalyst-free growth of InAs nanowires on Si (111) by CBE," *Nanotechnology*, vol. 26, p. 415604, Sept. 2015.

[46] B. Mandl, J. Stangl, T. Mårtensson, A. Mikkelsen, J. Eriksson, L. S. Karlsson, G. Bauer, L. Samuelson, and W. Seifert, "Au-Free Epitaxial Growth of InAs Nanowires," *Nano Letters*, vol. 6, pp. 1817–1821, Aug. 2006.

[47] K. Tomioka, J. Motohisa, S. Hara, and T. Fukui, "Control of InAs Nanowire Growth Directions on Si," *Nano Letters*, vol. 8, pp. 3475–3480, Oct. 2008.

[48] L. C. Chuang, F. G. Sedgwick, R. Chen, W. S. Ko, M. Moewe, K. W. Ng, T.-T. D. Tran, and C. Chang-Hasnain, "GaAs-Based Nanoneedle Light Emitting Diode and Avalanche Photodiode Monolithically Integrated on a Silicon Substrate," *Nano Letters*, vol. 11, pp. 385–390, Feb. 2011.

[49] C.-H. Song, M. Kong, H. Jang, S. Tae Lee, H.-H. Park, C. Zoo Kim, S. Hyun Jung, Y. Choi, S. Kim, D.-H. Ko, K. Seo, and C.-S. Shin, "Vertical growth characterization of InAs nanowires grown by selective area growth on patterned InP(1 1 1)B substrate by a MOCVD method," *Solid-State Electronics*, vol. 175, p. 107939, Jan. 2021.

[50] K. Ikejiri, T. Sato, H. Yoshida, K. Hiruma, J. Motohisa, S. Hara, and T. Fukui, "Growth characteristics of GaAs nanowires obtained by selective area metal–organic vapour-phase epitaxy," *Nanotechnology*, vol. 19, p. 265604, May 2008.

[51] H. Küpers, R. B. Lewis, A. Tahraoui, M. Matalla, O. Krüger, F. Bastiman, H. Riechert, and L. Geelhaar, "Diameter evolution of selective area grown Ga-assisted GaAs nanowires," *Nano Research*, vol. 11, pp. 2885–2893, May 2018.

[52] K. Tomioka, Y. Kobayashi, J. Motohisa, S. Hara, and T. Fukui, "Selective-area growth of vertically aligned GaAs and GaAs/AlGaAs core-shell nanowires on Si(111) substrate," *Nanotechnology*, vol. 20, p. 145302, Apr. 2009.

[53] H. Yoshida, K. Ikejiri, T. Sato, S. Hara, K. Hiruma, J. Motohisa, and T. Fukui, "Analysis of twin defects in GaAs nanowires and tetrahedra and their correlation to GaAs(111)B surface reconstructions in selective-area metal organic vapour-phase epitaxy," *Journal of Crystal Growth*, vol. 312, pp. 52–57, Dec. 2009.

[54] X. Wang, W. Yang, B. Wang, X. Ji, S. Xu, W. Wang, Q. Chen, and T. Yang, "Effect of nanohole size on selective area growth of InAs nanowire arrays on Si substrates," *Journal of Crystal Growth*, vol. 460, pp. 1–4, Feb. 2017.

[55] S. Plissard, G. Larrieu, X. Wallart, and P. Caroff, "High yield of self-catalyzed GaAs nanowire arrays grown on silicon via gallium droplet positioning," *Nanotechnology*, vol. 22, p. 275602, July 2011.

[56] M. T. Robson, V. G. Dubrovskii, and R. R. LaPierre, "Conditions for high yield of selective-area epitaxy InAs nanowires on SiO x /Si(111) substrates," *Nanotechnology*, vol. 26, no. 46, p. 465301, 2015.

[57] J. Vukajlovic-Plestina, W. Kim, L. Ghisalberti, G. Varnavides, G. Tütüncuoglu, H. Potts, M. Friedl, L. Güniat, W. C. Carter, V. G. Dubrovskii, and A. Fontcuberta i Morral, "Fundamental aspects to localize self-catalyzed III-V nanowires on silicon," *Nature Communications*, vol. 10, p. 869, Dec. 2019.

[58] Y. Kim, H. J. Joyce, Q. Gao, H. H. Tan, C. Jagadish, M. Paladugu, J. Zou, and A. A. Suvorova, "Influence of Nanowire Density on the Shape and Optical Properties of Ternary InGaAs Nanowires," *Nano Letters*, vol. 6, pp. 599–604, Apr. 2006.

[59] I. Regolin, V. Khorenko, W. Prost, F.-J. Tegude, D. Sudfeld, J. Kästner, and G. Dumpich, "Composition control in metal-organic vapor-phase epitaxy grown InGaAs nanowhiskers," *Journal of Applied Physics*, vol. 100, p. 074321, Oct. 2006.

[60] A. S. Ameruddin, P. Caroff, H. H. Tan, C. Jagadish, and V. G. Dubrovskii, "Understanding the growth and composition evolution of gold-seeded ternary InGaAs nanowires," *Nanoscale*, vol. 7, pp. 16266–16272, Oct. 2015.

[61] Y.-N. Guo, H.-Y. Xu, G. J. Auchterlonie, T. Burgess, H. J. Joyce, Q. Gao, H. H. Tan, C. Jagadish, H.-B. Shu, X.-S. Chen, W. Lu, Y. Kim, and J. Zou, *Phase Separation Induced by Au Catalysts in Ternary InGaAs Nanowires*. Jan. 2013.

[62] J. J. Hou, N. Han, F. Wang, F. Xiu, S. Yip, A. T. Hui, T. Hung, and J. C. Ho, "Synthesis and Characterizations of Ternary InGaAs Nanowires by a Two-Step Growth Method for High-Performance Electronic Devices," *ACS Nano*, vol. 6, pp. 3624–3630, Apr. 2012.

[63] M. Heiß, A. Gustafsson, S. Conesa-Boj, F. Peiró, J. R. Morante, G. Abstreiter, J. Arbiol, L. Samuelson, and A. F. i. Morral, "Catalyst-free nanowires with axial InxGa1-xAs/GaAs heterostructures," *Nanotechnology*, vol. 20, p. 075603, Jan. 2009.

[64] J. C. Shin, K. H. Kim, K. J. Yu, H. Hu, L. Yin, C.-Z. Ning, J. A. Rogers, J.-M. Zuo, and X. Li, "InxGa1-xAs Nanowires on Silicon: One-Dimensional Heterogeneous Epitaxy, Bandgap Engineering, and Photovoltaics," *Nano Letters*, vol. 11, pp. 4831–4838, Nov. 2011.

[65] S. Hertenberger, S. Funk, K. Vizbaras, A. Yadav, D. Rudolph, J. Becker, S. Bolte, M. Döblinger, M. Bichler, G. Scarpa, P. Lugli, I. Zardo, J. J. Finley, M.-C. Amann, G. Abstreiter, and G. Koblmüller, "High compositional homogeneity in In-rich InGaAs nanowire arrays on nanoimprinted SiO2/Si (111)," *Applied Physics Letters*, vol. 101, p. 043116, July 2012.

[66] J. Miao, W. Hu, N. Guo, Z. Lu, X. Zou, L. Liao, S. Shi, P. Chen, Z. Fan, J. C. Ho, T.-X. Li, X. S. Chen, and W. Lu, "Single InAs Nanowire Room-Temperature Near-Infrared Photodetectors," *ACS Nano*, vol. 8, pp. 3628–3635, Apr. 2014.

[67] S. Thunich, L. Prechtel, D. Spirkoska, G. Abstreiter, A. Fontcuberta i Morral, and A. W. Holleitner, "Photocurrent and photoconductance properties of a GaAs nanowire," *Applied Physics Letters*, vol. 95, p. 083111, Aug. 2009.

[68] A. Brenneis, J. Overbeck, J. Treu, S. Hertenberger, S. Morkötter, M. Döblinger, J. J. Finley, G. Abstreiter, G. Koblmüller, and A. W. Holleitner, "Photocurrents in a Single InAs Nanowire/Silicon Heterojunction," *ACS Nano*, vol. 9, pp. 9849–9858, Oct. 2015.

[69] H. Xia, Z.-Y. Lu, T.-X. Li, P. Parkinson, Z.-M. Liao, F.-H. Liu, W. Lu, W.-D. Hu, P.-P. Chen, H.-Y. Xu, J. Zou, and C. Jagadish, "Distinct Photocurrent Response of Individual GaAs Nanowires Induced by n-Type Doping," *ACS Nano*, vol. 6, pp. 6005–6013, July 2012.

[70] D. Ren, X. Meng, Z. Rong, M. Cao, A. C. Farrell, S. Somasundaram, K. M. Azizur-Rahman, B. S. Williams, and D. L. Huffaker, "Uncooled Photodetector at Short-Wavelength Infrared Using InAs Nanowire Photoabsorbers on InP with p–n Heterojunctions," *Nano Letters*, vol. 18, pp. 7901–7908, Dec. 2018.

[71] K. M. Azizur-Rahman and R. R. LaPierre, "Optical design of a mid-wavelength infrared InSb nanowire photodetector," *Nanotechnology*, vol. 27, p. 315202, Aug. 2016.

[72] C. J. Goosney, V. M. Jarvis, D. P. Wilson, N. I. Goktas, and R. R. LaPierre, "InSb nanowires for multispectral infrared detection," *Semiconductor Science and Technology*, vol. 34, p. 035023, Mar. 2019.

[73] D. Saxena, S. Mokkapati, P. Parkinson, N. Jiang, Q. Gao, H. H. Tan, and C. Jagadish, "Optically pumped room-temperature GaAs nanowire lasers," *Nature Photonics*, vol. 7, pp. 963–968, Dec. 2013.

[74] Y. Hu, R. R. LaPierre, M. Li, K. Chen, and J.-J. He, "Optical characteristics of GaAs nanowire solar cells," *Journal of Applied Physics*, vol. 112, p. 104311, Nov. 2012.

[75] M. Yao, N. Huang, S. Cong, C.-Y. Chi, M. A. Seyedi, Y.-T. Lin, Y. Cao, M. L. Povinelli, P. D. Dapkus, and C. Zhou, "GaAs Nanowire Array Solar Cells with Axial p–i–n Junctions," *Nano Letters*, vol. 14, pp. 3293–3303, June 2014.

[76] N. Han, Z.-x. Yang, F. Wang, G. Dong, S. Yip, X. Liang, T. F. Hung, Y. Chen, and J. C. Ho, "High-Performance GaAs Nanowire Solar Cells for Flexible and Transparent Photovoltaics," *ACS Applied Materials & Interfaces*, vol. 7, pp. 20454–20459, Sept. 2015.

[77] G. B. Stringfellow, "Fundamental aspects of vapor growth and epitaxy," *Journal of Crystal Growth*, vol. 115, pp. 1–11, Dec. 1991.

[78] E. Gil-Lafon, J. Napierala, D. Castelluci, A. Pimpinelli, R. Cadoret, and B. Gérard, "Selective growth of GaAs by HVPE: keys for accurate control of the growth morphologies," *Journal of Crystal Growth*, vol. 222, pp. 482–496, Jan. 2001.

[79] A. Pimpinelli, R. Cadoret, E. Gil-Lafon, J. Napierala, and A. Trassoudaine, "Two-particle surface diffusion-reaction models of vapour-phase epitaxial growth on vicinal surfaces," *Journal of Crystal Growth*, vol. 258, pp. 1–13, Oct. 2003.

[80] D. W. Shaw, "Mechanisms in Vapour Epitaxy of Semiconductors," in *Crystal Growth: Theory and Techniques Volume 1* (C. H. L. Goodman, ed.), pp. 1–48, Boston, MA: Springer US, 1974.

[81] E. Gil, *Realisation par la methode aux hydrures et etude de puits quantiques contraints ga#xin#1##xas/inp*. thesis, Clermont-Ferrand 2, Jan. 1992.

[82] E. Gil-Lafon, J. Napierala, A. Pimpinelli, R. Cadoret, A. Trassoudaine, and D. Castelluci, "Direct condensation modelling for a two-particle growth system: application to GaAs grown by hydride vapour phase epitaxy," *Journal of Crystal Growth*, vol. 258, pp. 14–25, Oct. 2003.

[83] U. P. Gomes, D. Ercolani, V. Zannier, S. Battiato, E. Ubyivovk, V. Mikhailovskii, Y. Murata, S. Heun, F. Beltram, and L. Sorba, "Heterogeneous nucleation of catalyst-free InAs nanowires on silicon," *Nanotechnology*, vol. 28, p. 065603, Jan. 2017.

[84] S. A. Dayeh, E. T. Yu, and D. Wang, "IIIV Nanowire Growth Mechanism: V/III Ratio and Temperature Effects," *Nano Letters*, vol. 7, pp. 2486–2490, Aug. 2007.

[85] E. Gil, Y. André, R. Cadoret, and A. Trassoudaine, "2 - Hydride Vapor Phase Epitaxy for Current III–V and Nitride Semiconductor Compound Issues," in *Handbook of Crystal Growth (Second Edition)* (T. F. Kuech, ed.), Handbook of Crystal Growth, pp. 51–93, Boston: North-Holland, Jan. 2015.

[86] R. Cadoret and Gil-Lafon, "Mécanismes de croissance des faces {001} exactes et désorientées de GaAs par la méthode aux chlorures sous H2 : diffusion superficielle, croissance par spirale, mécanismes de désorption HCl et GaCl3," *Journal de Physique I*, vol. 7, pp. 889–907, July 1997.

[87] Z. Liu, C. Merckling, R. Rooyackers, O. Richard, H. Bender, Y. Mols, M. Vila, J. Rubio-Zuazo, G. R. Castro, N. Collaert, A. Thean, W. Vandervorst, and M. Heyns, "Correlation between surface reconstruction and polytypism in InAs nanowire selective area epitaxy," *Physical Review Materials*, vol. 1, p. 074603, Dec. 2017.

[88] T. Hayakawa, M. Morishima, and S. Chen, "Surface reconstruction limited mechanism of molecular-beam epitaxial growth of AlGaAs on (111)B face," *Applied Physics Letters*, vol. 59, pp. 3321–3323, Dec. 1991.

[89] J. Napierala, E. Gil-Lafon, D. Castelluci, A. Pimpinelli, and B. Gérard, "Control of the growth morphologies of GaAs stripes grown on patterned substrates by HVPE," *Optical Materials*, vol. 17, pp. 315–318, June 2001.

[90] J. Tourret, O. Gourmala, Y. André, A. Trassoudaine, E. Gil, D. Castelluci, and R. Cadoret, "A complete crystallographic study of GaN epitaxial morphologies in selective area growth by hydride vapour phase epitaxy (SAG-HVPE)," *Journal of Crystal Growth*, vol. 311, pp. 1460–1465, Mar. 2009.

[91] K. Lekhal, S.-Y. Bae, H.-J. Lee, T. Mitsunari, A. Tamura, M. Deki, Y. Honda, and H. Amano, "Controlled morphology of regular GaN microrod arrays by selective area growth with HVPE," *Journal of Crystal Growth*, vol. 447, pp. 55–61, Aug. 2016.

[92] M. Zeghouane, G. Avit, T. W. Cornelius, D. Salomon, Y. André, C. Bougerol, T. Taliercio, A. Meguekam-Sado, P. Ferret, D. Castelluci, E. Gil, E. Tournié, O. Thomas, and A. Trassoudaine, "Selective growth of ordered hexagonal InN nanorods," *CrystEngComm*, vol. 21, pp. 2702–2708, Apr. 2019.

[93] G. Koblmüller, K. Vizbaras, S. Hertenberger, S. Bolte, D. Rudolph, J. Becker, M. Döblinger, M.-C. Amann, J. J. Finley, and G. Abstreiter, "Diameter dependent optical emission properties of InAs nanowires grown on Si," *Applied Physics Letters*, vol. 101, p. 053103, July 2012.

[94] M. Sonner, J. Treu, K. Saller, H. Riedl, J. J. Finley, and G. Koblmüller, "Carrier concentration dependent photoluminescence properties of Si-doped InAs nanowires," *Applied Physics Letters*, vol. 112, p. 091904, Feb. 2018.

[95] M. B. Rota, A. S. Ameruddin, H. A. Fonseka, Q. Gao, F. Mura, A. Polimeni, A. Miriametro, H. H. Tan, C. Jagadish, and M. Capizzi, "Bandgap Energy of Wurtzite InAs Nanowires," *Nano Letters*, vol. 16, pp. 5197–5203, Aug. 2016.

[96] X. Chen, Q. Zhuang, H. Alradhi, Z. M. Jin, L. Zhu, X. Chen, and J. Shao, "Midinfrared Photoluminescence up to 290 K Reveals Radiative Mechanisms and Substrate Doping-Type Effects of InAs Nanowires," *Nano Letters*, vol. 17, pp. 1545–1551, Mar. 2017.

[97] F. Bechstedt and A. Belabbes, "Structure, energetics, and electronic states of III–V compound polytypes," *Journal of Physics: Condensed Matter*, vol. 25, p. 273201, June 2013.

[98] E. A. Anyebe and M. Kesaria, "Photoluminescence Characteristics of Zinc Blende InAs Nanowires," *Scientific Reports*, vol. 9, p. 17665, Nov. 2019.

[99] C. J. Goosney, V. M. Jarvis, J. F. Britten, and R. R. LaPierre, "InAsSb pillars for multispectral long-wavelength infrared absorption," *Infrared Physics & Technology*, vol. 111, p. 103566, Dec. 2020.

[100] K. M. Azizur-Rahman and R. R. LaPierre, "Wavelength-selective absorptance in GaAs, InP and InAs nanowire arrays," *Nanotechnology*, vol. 26, p. 295202, July 2015. Publisher: IOP Publishing.

[101] N. Dhindsa, A. Chia, J. Boulanger, I. Khodadad, R. LaPierre, and S. S. Saini, "Highly ordered vertical GaAs nanowire arrays with dry etching and their optical properties," *Nanotechnology*, vol. 25, p. 305303, July 2014. Publisher: IOP Publishing.

[102] E. Gil-Lafon, A. Videcoq, J. Napierala, D. Castelluci, A. Pimpinelli, B. Gérard, J. Jimenez, and M. Avella, "High-quality GaAs-related lateral junctions on Si by conformal growth," *Optical Materials*, vol. 17, pp. 267–270, June 2001.

[103] Z. Dong, *Synthesis of GaAs nanowires and nanostructures by HVPE on Si substrate. Application to a microbial fuel cell based on GaAs nanowires*. thesis, Clermont Auvergne, Mar. 2017.

[104] I. W. Yeu, G. Han, J. Park, C. S. Hwang, and J.-H. Choi, "Theoretical understanding of the catalyst-free growth mechanism of GaAs \textless111\textgreaterB nanowires," *Applied Surface Science*, vol. 497, p. 143740, Dec. 2019.

[105] J. Noborisaka, J. Motohisa, and T. Fukui, "Catalyst-free growth of GaAs nanowires by selective-area metalorganic vapor-phase epitaxy," *Applied Physics Letters*, vol. 86, p. 213102, May 2005. Publisher: American Institute of Physics.

[106] T. H. T. Hamano, H. H. H. Hirayama, and Y. A. Y. Aoyagi, "New Technique for Fabrication of Two-Dimensional Photonic Bandgap Crystals by Selective Epitaxy," *Japanese Journal of Applied Physics*, vol. 36, p. L286, Mar. 1997. Publisher: IOP Publishing.

[107] M. Cantoro, G. Brammertz, O. Richard, H. Bender, F. Clemente, M. Leys, S. Degroote, M. Caymax, M. Heyns, and S. D. Gendt, "Controlled III/V Nanowire Growth by Selective-Area Vapor-Phase Epitaxy," *Journal of The Electrochemical Society*, vol. 156, p. H860, Oct. 2009. Publisher: IOP Publishing.

[108] P. Caroff, K. A. Dick, J. Johansson, M. E. Messing, K. Deppert, and L. Samuelson, "Controlled polytypic and twin-plane superlattices in iii–v nanowires," *Nature Nanotechnology*, vol. 4, pp. 50–55, Jan. 2009. Bandiera_abtest: a Cg_type: Nature Research Journals Number: 1 Primary_atype: Research Publisher: Nature Publishing Group.

[109] V. G. Dubrovskii and N. V. Sibirev, "Growth thermodynamics of nanowires and its application to polytypism of zinc blende III-V nanowires," *Physical Review B*, vol. 77, p. 035414, Jan. 2008.

[110] M. Yao, C. Sheng, M. Ge, C.-Y. Chi, S. Cong, A. Nakano, P. D. Dapkus, and C. Zhou, "Facile Five-Step Heteroepitaxial Growth of GaAs Nanowires on Silicon Substrates and the Twin Formation Mechanism," *ACS Nano*, vol. 10, pp. 2424–2435, Feb. 2016. Publisher: American Chemical Society.

[111] J. De-Sheng, Y. Makita, K. Ploog, and H. J. Queisser, "Electrical properties and photoluminescence of Te-doped GaAs grown by molecular beam epitaxy," *Journal of Applied Physics*, vol. 53, pp. 999–1006, Feb. 1982. Publisher: American Institute of Physics.

[112] H. Hijazi, G. Monier, E. Gil, A. Trassoudaine, C. Bougerol, C. Leroux, D. Castellucci, C. Robert-Goumet, P. E. Hoggan, Y. André, N. Isik Goktas, R. R. LaPierre, and V. G. Dubrovskii, "Si Doping of Vapor–Liquid–Solid GaAs Nanowires: n-Type or p-Type?," *Nano Letters*, vol. 19, pp. 4498–4504, July 2019. Publisher: American Chemical Society.

[113] G. Koblmüller and G. Abstreiter, "Growth and properties of InGaAs nanowires on silicon," *physica status solidi (RRL) – Rapid Research Letters*, vol. 8, pp. 11–30, Jan. 2014.

[114] L. Hollan, J. M. Durand, and R. Cadoret, "Influence of the Growth Parameters in GaAs Vapor Phase Epitaxy," *Journal of The Electrochemical Society*, vol. 124, p. 135, Jan. 1977. Publisher: IOP Publishing.

[115] Y. Kohashi, T. Sato, K. Ikejiri, K. Tomioka, S. Hara, and J. Motohisa, "Influence of growth temperature on growth of InGaAs nanowires in selective-area metal–organic vapor-phase epitaxy," *Journal of Crystal Growth*, vol. 338, pp. 47–51, Jan. 2012.

[116] I. Barin, "Ga-Ge5U3," in *Thermochemical Data of Pure Substances*, pp. 728–780, John Wiley & Sons, Ltd, 1995. Section: 12 _eprint: https://onlinelibrary.wiley.com/doi/pdf/10.1002/9783527619825.ch12h.

[117] I. Barin, "I-Kr," in *Thermochemical Data of Pure Substances*, pp. 844–924, John Wiley & Sons, Ltd, 1995. Section: 12 _eprint: https://onlinelibrary.wiley.com/doi/pdf/10.1002/9783527619825.ch12j.